

HEAT TRANSFER AND PRESSURE DROP IN THE CONDENSING SUPERHEATED  
REGION WITH VISUALIZATION AND FILM THICKNESS MEASUREMENT

BY

MELISSA MEYER

THESIS

Submitted in partial fulfillment of the requirements  
for the degree of Master of Science in Mechanical Engineering  
in the Graduate College of the  
University of Illinois at Urbana-Champaign, 2014

Urbana, Illinois

Adviser:

Professor Predrag Hrnjak

## ABSTRACT

Traditionally, condensation has been characterized by division into three zones: desuperheating, two-phase, and subcooled regions. According to this characterization, heat transfer and pressure drop in condensers are modeled separately for the single-phase and two-phase regions. When plotted as a function of enthalpy, the correlations show a discontinuity between the single-phase and two-phase zones because the three-zone approach implicitly assumes thermodynamic equilibrium throughout the condensation process. In reality, the refrigerant is not at equilibrium, and condensation occurs outside the conventionally defined two-phase zone. Condensation actually starts when the wall temperature reaches saturation, even in the presence of superheated vapor. Similarly, condensation continues if some vapor remains even when the bulk refrigerant enthalpy is indicating a subcooled state. These two situations make a fourth and fifth zone in the condenser, classified as the condensing superheated and condensing subcooled zones. The effects of these zones on heat transfer have been described previously, but the effects on pressure drop have received less attention, and confirmation of the physical processes thought to be occurring has not yet been provided.

This paper presents experimental results verifying the presence of liquid in the condensing superheated region. Flow visualization experiments with R134a revealed that condensate began to appear when the bulk refrigerant enthalpy was above saturation, as droplets and rivulets on the tube wall and then as an annular film with mist entrained in the vapor core. Liquid film thickness measurements further confirmed the growth of a condensate film at bulk enthalpies greater than saturation. The heat transfer coefficient followed the same trend seen in earlier experiments,

rising sharply in the condensing superheated region for a smooth transition between the single-phase and two-phase zones. The pressure drop gradient also increased significantly above the single-phase prediction once the wall temperature fell below the saturation temperature, as shown by prior experimental results for R32. In the condensing superheated region, shear interactions between the liquid film and vapor increase the pressure drop compared to vapor alone. As condensation continues, the shear increases due to a thicker and wavier liquid layer, but friction and momentum losses decrease as the refrigerant velocity decreases. These competing factors cause a peak and subsequent decrease in the pressure drop gradient and are corroborated by the flow visualization.

## **ACKNOWLEDGMENTS**

I would like to thank my adviser, Dr. Pega Hrnjak, for his patience and guidance throughout this project. I would like to thank Rahul Agarwal, Augusto Zimmermann, Neal Lawrence, Feini Zhang, Jiange Xiao, Lihan Xu, Jun Li, and the rest of my colleagues in the Air Conditioning and Refrigeration Center for their help and good humor. Thank you to Lisa Burdin for her cheerful support of the entire group. I would like to thank my family and friends for their encouragement. Finally, I would like to thank the sponsor companies of the ACRC for their support and motivation.

## TABLE OF CONTENTS

Nomenclature.....	vi
Chapter 1: Introduction.....	1
1.1 Motivation and scope.....	1
1.2 Figures.....	4
Chapter 2: Background.....	5
2.1 Condensation under superheated conditions.....	5
2.2 Condensation flow regimes and visualization.....	7
2.3 Film thickness measurement.....	7
2.4 Figures.....	9
Chapter 3: Experimental Method.....	10
3.1 Experimental facility.....	10
3.2 Measurements and data reduction.....	14
3.3 Figures.....	21
3.4 Tables.....	27
Chapter 4: Results and Discussion.....	28
4.1 Heat transfer.....	28
4.2 Visualization.....	29
4.3 Film thickness.....	31
4.4 Pressure drop.....	32
4.5 Figures.....	36
Chapter 5: Conclusion.....	69

5.1 Summary.....	69
5.2 Recommendations for future study.....	70
References.....	72
Appendix A: Repeatability test and pressure drop sensitivity analysis.....	75
A.1 Figures.....	76
Appendix B: CAD Drawings.....	77
B.1 Film thickness measurement support blocks.....	77
B.2 Visualization section components.....	84
Appendix C: Uncertainty analysis.....	87
Appendix D: MATLAB code.....	92
D.1 Film thickness image processing code.....	92
D.2 Optical model of critical light reflection for round tube.....	104

## NOMENCLATURE

$c_p$	Specific heat capacity	(J kg <sup>-1</sup> K <sup>-1</sup> )
$d_i$	Inner diameter of test tube	(m)
$h$	Specific enthalpy	(J kg <sup>-1</sup> )
HTC	Heat transfer coefficient	(W m <sup>-2</sup> K <sup>-1</sup> )
$L$	Cooling length of test tube	(m)
$\dot{m}$	Mass flow rate	(kg s <sup>-1</sup> )
$P$	Pressure	(Pa)
$\dot{Q}$	Heat transfer rate	(W)
$q$	Heat flux	(W m <sup>-2</sup> )
$T$	Temperature	(°C)
$Z$	Distance along test tube	(m)
$\rho$	Density	(kg m <sup>-3</sup> )

### Subscripts

$b$	Evaluated at bulk temperature
cond	Conduction heat from upstream
gain	Heat gain from ambient air
H <sub>2</sub> O	Water
$i$	Inlet
MC	Mixing chamber
$o$	Outlet

PC	Pre-cooler
r	Refrigerant
sat	Saturated
TS	Test section
vis	Visualization section
wi	Inner wall of test section

## CHAPTER 1: INTRODUCTION

### 1.1 Motivation and scope

Traditionally, condensation has been described using three zones: desuperheating, two-phase, and subcooled regions. The two-phase region begins when the bulk enthalpy of the condensing fluid reaches the saturated vapor enthalpy, and ends when the bulk enthalpy reaches the saturated liquid value. The disadvantage of characterizing condensation heat transfer and pressure drop in this way is that the models give unrealistic predictions at the boundaries of the zones. When plotted as a function of enthalpy, the correlations for heat transfer coefficient and pressure drop show discontinuities between the single-phase and two-phase regions, as seen in Figure 1. These discontinuities occur because the three-zone model implicitly assumes thermodynamic equilibrium throughout the condensation process. Under this assumption, the first drop of condensate would form when the bulk refrigerant enthalpy reached the saturated vapor enthalpy, i.e. at the start of the two-phase zone. However, the refrigerant has a nonuniform temperature profile across the diameter of the tube, and the fluid is colder in the vicinity of the wall than in the center of the tube. Experimental studies have indicated that condensation begins when the wall temperature falls below the saturation temperature, even in the presence of superheated vapor in the center of the tube. This means that condensation begins earlier than predicted by the three-zone model, when the bulk enthalpy of the refrigerant is greater than the saturated vapor enthalpy. Similarly, condensation continues when the bulk enthalpy of the refrigerant is less than the saturated liquid enthalpy, in the presence of some vapor and some subcooled liquid. Since condensation thus occurs across a broader enthalpy range than conventionally assumed, its

effects on heat transfer and pressure drop are also present outside of the traditionally defined two-phase region.

The heat transfer effects of condensation outside the two-phase region have been described earlier by Kondou and Hrnjak (2011a, 2011b, 2012) and by Agarwal and Hrnjak (2013). They defined a total of five zones: desuperheating (SH), condensing superheated (CSH), two-phase (TP), condensing subcooled (CSC), and subcooled (SC) regions. The condensing superheated zone begins when the wall temperature reaches the saturation temperature. The two-phase zone is defined as before, as the region in which the bulk enthalpy is saturated. The condensing subcooled region begins at the saturated liquid enthalpy and ends when all of the vapor has condensed. In the condensing superheated and condensing subcooled zones, condensation increases the heat transfer coefficient above the single-phase correlation predictions so that it transitions smoothly between the two-phase and single-phase regions, as shown in Figure 2. Kondou and Hrnjak (2012) proposed a correlation combining the single-phase and two-phase heat transfer coefficients to predict the heat transfer coefficient in the condensing superheated zone, and Agarwal and Hrnjak (2013) developed a unified model for the heat transfer coefficient in all five zones. The above researchers gathered experimental heat transfer data supporting the existence of the CSH and CSC zones, as well as pressure drop data for the entire condensation process. However, the pressure drop in the CSH zone was not yet described, and a more physical model is needed for the heat transfer coefficient.

The goal of this research is to move towards filling those needs and thus further develop our ability to predict refrigerant behavior in the CSH zone, eventually leading to the design of more

efficient condensers in the refrigeration and air conditioning industry. This goal was approached from several angles. Heat transfer experiments with flow visualization were performed in order to test the hypothesis that condensation occurs outside the two-phase region. In addition, visualization allows us to identify flow regimes and select appropriate heat transfer models as condensation progresses, as well as determine the liquid and vapor velocities for use in heat transfer and pressure drop models. The visualization performed for this work is unusual in that a diabatic visualization section was used, more closely approximating the behavior of the fluid in an actual condenser than typical adiabatic visualization experiments. In parallel with the flow visualization, liquid film thickness measurements were taken. The increase in film thickness is used to determine the change in the liquid mass along the condenser, which is directly tied to the rate of latent heat transfer. Therefore, insight into how the film grows can be used to break down the contributions of latent and sensible heat transfer to the overall heat transfer rate. The experimental work described so far all contributes to a deeper understanding of the physical processes taking place during condensation, helping to enable the development of a more fundamental five-zone model. Although currently only a five-zone model for heat transfer has been proposed, a pressure drop model is also needed that accurately accounts for condensation outside the two-phase zone. As a first step, this work reexamines the pressure drop data from previous experiments and analyzes the observed phenomena in the context of the five-zone hypothesis of condensation and the visualization and film thickness experiments.

The remainder of this document presents various aspects of the research described in the previous paragraph. First, a brief literature review is presented to provide the background of the project. Next, the experimental facility and methods are explained. The experimental results are

then discussed, and finally the main conclusions are given along with recommendations for future study. Figures and tables are grouped at the end of each chapter, while more details of certain aspects of the experimental procedure and results are provided in the appendices.

## 1.2 Figures

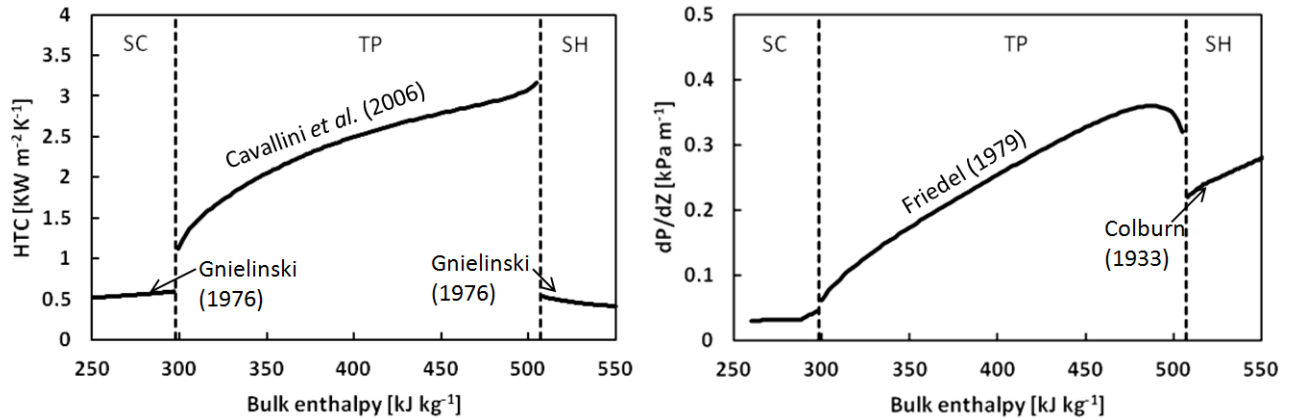


Figure 1: Traditional condensation models for heat transfer coefficient and pressure drop with subcooled, two-phase, and superheated regions. The plots shown are for R32 at 3.141 MPa with a mass flux of  $100 \text{ kg m}^{-2} \text{ s}^{-1}$

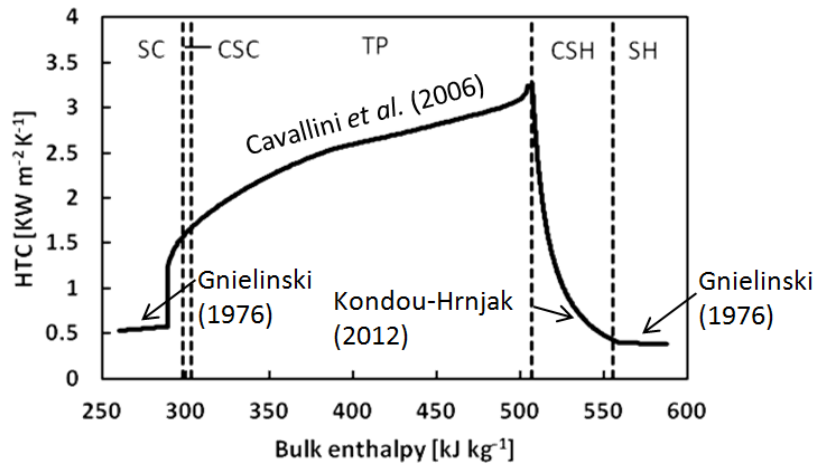


Figure 2: Five-zone condensation model for R32 at 3.141 MPa with a mass flux of  $100 \text{ kg m}^{-2} \text{ s}^{-1}$

## CHAPTER 2: BACKGROUND

### 2.1 Condensation under superheated conditions

Although the concept of condensation in the presence of superheated vapor is well-established, relatively little has been published on calculating its effects on heat transfer and pressure drop. Altman et al. (1960) measured the average heat transfer coefficients (HTCs) of R22 condensing in a 1.22-m-long horizontal tube. They reported six data points with varying degrees of superheat at the test section inlet, up to 21 K. From these data, they proposed an empirical correlation for the average HTC with superheat. The correlation is applicable only to R22 and, along with the experimental data, shows a 30 to 70 percent decrease in the condensing superheated HTC compared to a saturated HTC. Miropolsky et al. (1974) measured quasi-local HTCs of superheated steam condensing in vertical smooth tubes. Their results confirmed that condensation begins when the wall temperature falls below the saturation temperature, and they also offered an empirical correlation. Fujii et al. (1978) studied R11 and R113 condensing in horizontal smooth tubes. They measured the radial temperature distribution inside the tube and verified the coexistence of superheated vapor and subcooled liquid. In addition, they offered a semi-empirical correlation for the HTC. Lee et al. (1991) investigated superheated R22 condensing in a horizontal tube and proposed a model in which the HTC for condensing superheated vapor is found by representing the total heat flux as the sum of a forced convection (superheated) term and a two-phase condensation term, as in equation (2.1).

$$q_{\text{tot}} = \text{HTC}(T_{\text{rb}} - T_{\text{w}}) = \text{HTC}_{\text{SH}}(T_{\text{rb}} - T_{\text{sat}}) + \text{HTC}_{\text{TP}}(T_{\text{sat}} - T_{\text{w}}) \quad (2.1)$$

Their model predicted their experimental data within 20 percent. Webb (1998) proposed a similar model but defined the overall HTC in terms of the conventional driving temperature

difference for condensation,  $(T_{\text{sat}} - T_w)$ , instead of  $(T_{\text{rb}} - T_w)$ . Webb reported that this model gives the same result as that of Lee et al.

Kondou and Hrnjak (2011a, 2011b, 2012) proposed a calculation scheme identical to equation (2.1) for heat transfer in the condensing superheated zone, resulting in a semi-empirical correlation composed of a combination of existing single-phase turbulent and two-phase correlations. They experimentally determined HTC for  $\text{CO}_2$  and R410A in horizontal tubes with various heat and mass fluxes and at pressures around and below the critical point. They showed that the HTC consistently began to deviate from single-phase predictions when the wall temperature fell below the saturation temperature. The significant rise in the HTC in the CSH zone was in agreement with their proposed correlation. Agarwal and Hrnjak (2013a, 2013b) further validated the Kondou-Hrnjak correlation through experiments with R134a, R32, and R1234ze(E) with mass fluxes of 100 to 300  $\text{kg m}^{-2} \text{s}^{-1}$  and saturation temperatures of 30 to 50  $^\circ\text{C}$ , reporting a similar trend in the CSH zone. They also defined a fifth zone, the condensing subcooled zone, in which the bulk enthalpy is below the saturated liquid enthalpy but some vapor remains in the presence of subcooled liquid. They proposed a unified model across all five condensation zones and reported that the model predicted their experimental HTC results within 27 percent overall. In addition to the HTC, Kondou and Hrnjak (2012) and Agarwal and Hrnjak (2013a, 2013b) reported results for pressure drop measured during condensation. However, they did not propose a pressure drop model and focused primarily on heat transfer.

## **2.2 Condensation flow regimes and visualization**

Heat and momentum transfer processes depend strongly on the flow behavior of the condensing fluid, so predictions of heat transfer coefficients and pressure drop should take into account the flow regimes that occur. Figure 3 illustrates the general progression of common flow regimes that occur during condensation, including mist flow, annular and semi-annular flow, wavy flow, stratified flow, slug flow, plug flow, and bubbly flow. Combinations of these regimes are also possible, such as stratified-wavy or misty annular flow. The particular flow patterns that occur depend on the flow rate, fluid properties, and tube geometry.

Numerous flow regime and visualization studies have been performed, and a more detailed discussion of the literature is given by Dobson and Chato (1998). For the current work, the flow regime map of El Hajal et al. (2003) is selected as an example. They modified the earlier map of Kattan et al. (1998) for application to condensation in horizontal smooth tubes and then proposed a heat transfer model based on the new flow regime map. A map for R134a at a saturation temperature of 40 °C is shown in Figure 4.

## **2.3 Film thickness measurement**

Various methods have been utilized for measuring the liquid film thickness in two-phase flows, including contact needles, conductance probes, capacitive sensors, microwave absorption, audio reflection, light reflection or absorption, laser-induced fluorescence, fringe patterns, and visual interface detection. A review of the basic principles behind these methods and their use as reported in literature is provided by Wujek (2011). For this work, an optical method developed by Hurlburt and Newell (1996) was chosen. This technique has the advantages of being non-

intrusive, low-cost, and easy to use, with a fast frequency response. It relies on the principle of critical light reflection and is described in detail by Hurlburt and Newell (1996) and Shedd and Newell (1998). A brief overview of the method is given here.

When light from a point source shines diffusely on the interface of two media with different indices of refraction, the amount of light reflected or transmitted varies with the angle between the incident light and the interface, according to Fresnel's equations. An angle exists at which all of the incident light is reflected, as well as any light with a greater angle of incidence. The smallest angle for which all light is reflected is called the critical angle, and for planar surfaces it depends only on the indices of refraction of the two media. At angles smaller than the critical angle, little light is reflected, so critically reflected light from a point source forms a distinct circle around the source on the outer surface of the wall on which it shines. For planar surfaces, the radius of the reflected circle depends only on the critical angle and the thicknesses of each medium. Therefore, if the wall thickness and the indices of refraction of the wall, liquid, and vapor are known, the liquid film thickness can be determined by measuring the diameter of the critically reflected light circle. For tube geometries, the relationship between the film thickness and reflected light cannot be described by the simple equations of the planar case, and an ellipse is formed rather than a circle, but the basic principle is the same.

## 2.4 Figures

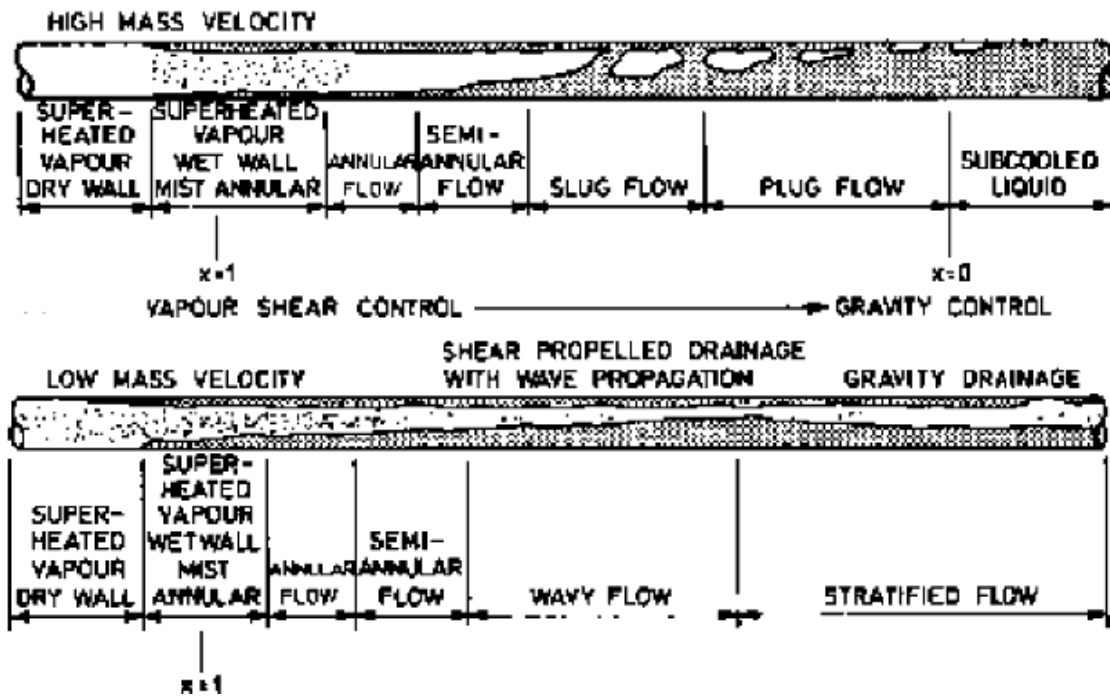


Figure 3: Flow patterns for condensation in horizontal tubes (Collier and Thome, 1994)

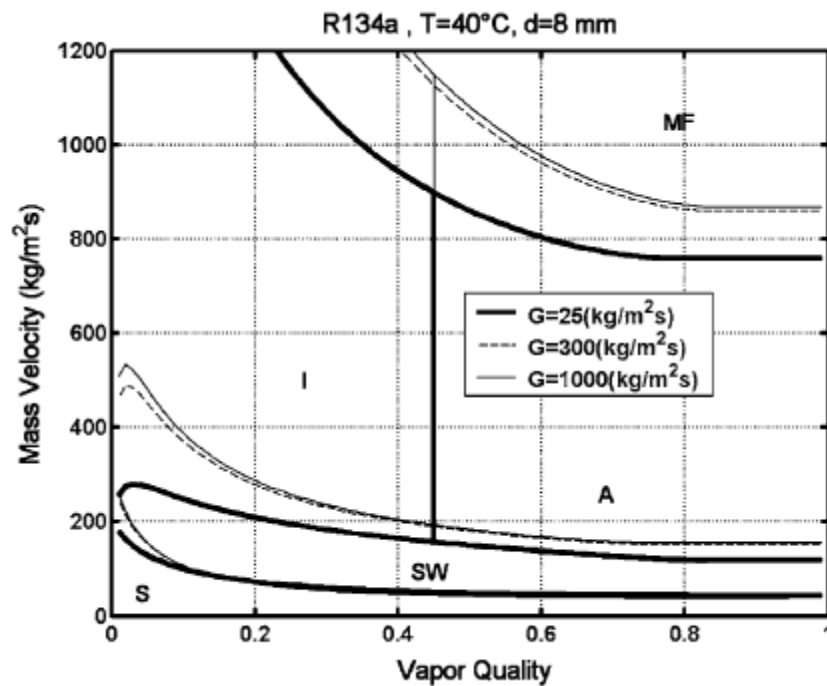


Figure 4: Flow pattern map for R134a at  $40^\circ\text{C}$  in an 8-mm diameter tube, where the transition curves were evaluated using three different mass fluxes (El Hajal et al., 2003)

## CHAPTER 3: EXPERIMENTAL METHOD

The flow visualization and film thickness experiments are intended to be connected to experiments performed previously in the same facility and described by Kondou and Hrnjak (2011a, 2011b, 2012) and Agarwal and Hrnjak (2013). The hypothesis was that the phenomena seen in these prior experiments would be supported and partially explained by the film thickness measurement and visualization aspects of the new experiments. Therefore, the same experimental facility was utilized with a few modifications to allow for the new measurements, and the experimental conditions were recreated as closely as possible. As a first step, only one refrigerant and set of operating conditions were selected; the focus is on the fundamental behavior of the condensing fluid and not on the comparison of different fluids, pressures, and flow rates. This first set of experiments was performed with R134a at 1.319 MPa (corresponding to a saturation temperature of 50 °C) with a mass flux of  $100 \text{ kg m}^{-2} \text{ s}^{-1}$  and a heat flux of  $10 \text{ kW m}^{-2}$ .

### 3.1 Experimental facility

Figure 5 shows a schematic of the facility in which experiments were previously performed to measure both the heat transfer and pressure drop of condensing refrigerants. The apparatus includes separate loops for refrigerant, water, and chilled water. The refrigerant loop consists of a variable speed gear pump, a coriolis-type mass flow meter, an electric pre-heater, a mixing chamber, a counter-flow concentric tube pre-cooler, a test section, sight glass, two after-coolers, and a receiver tank. A diaphragm-type differential pressure transducer measures the separate pressure drops across the pre-cooler and the test section. The pressure is controlled by the

refrigerant charge, heater setting, and flow rate of chilled water through the after-coolers. The refrigerant flow rate is controlled by the gear pump. The refrigerant is initially superheated in the pre-heater, and its condition at the test section inlet is adjusted by the temperature and flow rate of water through the pre-cooler. The heat flux in the test section is controlled by the flow of water through the test section.

Figure 6 illustrates the test section, which consists of a smooth copper tube 150 mm long with inner and outer diameters of 6.1 mm and 9.53 mm, respectively. The tube is oriented horizontally and covered with a thick brass jacket, with thermal paste filling the gap between the tube and jacket. Water flows through copper tubes soldered around the outside of the brass jacket, producing uniform cooling conditions throughout the test section. Twelve thermocouples are embedded in the top, bottom, left, and right of the test tube wall at three axial positions. Just before and after the test section, two 1.0-mm holes are bored through the refrigerant tube wall as pressure ports and connected to a differential pressure transducer through capillary tubes. The length between the pressure ports is 288 mm. Although this is longer than the length of the actual test section, the pressure drop between the ports is treated as the pressure drop across the test section. The larger distance between the ports allows for more accurate measurement of the pressure drop, and the deceleration effects on pressure drop in the adiabatic portion are small compared to the pressure drop in the diabatic test section.

Figure 7 shows a schematic of the modified facility used for the visualization and film thickness experiments. The general operation and heat transfer measurements are the same as described above with the exception of the removal of the pressure ports after the test section. This was

done in order to minimize the number of tube connections and resulting flow disturbances between the test section, film thickness measurement location, and visualization section, so the liquid film is allowed to develop undisturbed as much as possible. For data reduction purposes, pressure drop data was taken from previous experiments at corresponding test conditions. A sensitivity analysis showed that within the range of likely pressure drop readings, the value used did not have a large effect on the calculated enthalpy or heat transfer coefficient. Furthermore, the heat transfer results of the new experiments matched those of the former experiments within the range of experimental error. Therefore, the use of the old pressure drop data was assumed to be acceptable. The results of the sensitivity and repeatability analyses are included in Appendix A.

The copper tube between the test section outlet and film thickness section inlet is 69 cm long and insulated, and the conditions where the film thickness is measured are assumed to be approximately the same as at the test section outlet. The film thickness section consists of a 21-cm-long glass tube with an inner diameter of 6 mm and a wall thickness of 2 mm. At each end, the glass tube is inserted into a 10-mm to 3/8-in Swagelok union and sealed with JB Weld. The film thickness is measured approximately 17 cm from the upstream connection to allow the film to recover from any disturbance caused by the connection.

The film thickness is measured using the optical technique described by Shedd and Newell (1998) and Wujek (2011). With this method, diffuse light from a point source is shined on a transparent tube. The critically reflected light forms an ellipse whose minor diameter is dependent on the thickness of the liquid film inside the tube. The ellipse may be photographed

and its diameter measured to determine the film thickness. In order to measure the liquid film all around the circumference of the tube, a small self-contained device was constructed and is shown in Figure 8. The main components of the device are a Genius eFace 2025 webcam and a 2.5-mW, 635-nm laser module with power circuit. The webcam, laser, and circuit components are housed in a 5.25 inch by 3 inch by 2 inch box painted black on the inside to minimize interference from outside light. The box fits around the glass tube and has a removable lid so that the box may be taken on and off the tube. The box has slots cut on each side that allow the tube to pass through and maintain consistent alignment between the tube, camera, and laser. To measure the film at different circumferential locations, the entire box is rotated around the tube and held in place by aluminum support blocks if necessary. Drawings of the support blocks are included in Appendix B. The glass tube must have a layer of paint or tape to diffuse the light from the laser. Various masking, Teflon, and paper tapes as well as white spray paint were tested and a thin masking tape was found to produce the clearest images, although some graininess from the tape is still present. Measurements were taken by switching on the laser so that it shone on the center of the tube in front of the camera. The webcam was then used to capture still images of the tube and light ellipse since this allowed for higher resolution than video.

After the film thickness section, the refrigerant flows through a short copper connecting section and enters the visualization section. CAD drawings of the visualization section components are included in Appendix B. The visualization section consists of two concentric glass tubes approximately 20 cm long that are encased in a clear plastic shielding box. Refrigerant flows through the inner tube, which has an inner diameter of 6 mm and a wall thickness of 3 mm. Water flows through the outer tube, which has an inner diameter of 17 mm and a wall thickness

of 1.5 mm. The water is provided by the closed cooling water loop; it exits the test section, enters the downstream end of the visualization section via a manifold for a counterflow arrangement, and exits at the upstream end, where the outlet temperature is measured with a thermocouple. Temperature change between the test section outlet and visualization section inlet is assumed to be negligible. High-speed video of the condensing refrigerant is captured with a Vision Research SR-CMOS black and white camera using a 55-mm Nikon lens. The magnification is set such that a portion of tube approximately 2 cm long in the center of the visualization section is recorded. Due to the high magnification and short exposure time, intense lighting is necessary. The tube is backlit by a 300 W halogen lamp located about 15 cm behind the tube and separated from it by a translucent plastic sheet to diffuse the light.

### 3.2 Measurements and data reduction

#### 3.2.1 Heat transfer and pressure drop

The instruments used and uncertainties of experimental measurements are summarized in Table 1. The refrigerant temperature and pressure are measured in the mixer and the enthalpy is calculated under the assumption of equilibrium using Refprop 8.0 (Lemmon *et al.*, 2007). The changes in enthalpy over the pre-cooler and test section are obtained from water-side energy balances using the measured mass flow rates and inlet and outlet water temperatures, according to equations (1) and (2):

$$\Delta h_{PC} = \left[ (T_{H_2O,PCo} - T_{H_2O,PCi}) \dot{m}_{H_2O,PC} c_{PH_2O} - \dot{Q}_{gain,PC} \right] / \dot{m}_r \quad (1)$$

$$\Delta h_{TS} = \left[ (T_{H_2O,TSo} - T_{H_2O,TSi}) \dot{m}_{H_2O,TS} c_{PH_2O} - \dot{Q}_{gain,TS} \right] / \dot{m}_r \quad (2)$$

where  $\dot{Q}_{gain,PC}$  and  $\dot{Q}_{gain,TS}$  are preliminarily-measured heat leaks to ambient air through the insulation. The bulk mean temperature of the refrigerant in the test section is calculated from the

bulk enthalpy and pressure with Refprop's equilibrium state function, as shown in equations (3)-(5).

$$T_{rb,i} = f_{\text{equilibrium}}(h_{b,MC} - \Delta h_{PC}, P_{MC} - \Delta P_{PC}) \quad (3)$$

$$T_{rb,o} = f_{\text{equilibrium}}(h_{b,MC} - \Delta h_{PC} - \Delta h_{TS}, P_{MC} - \Delta P_{PC} - \Delta P_{TS}) \quad (4)$$

$$T_{rb} = (T_{rb,i} + T_{rb,o}) / 2 \quad (5)$$

The average heat flux on the interior wall of the test section is given by equation (6):

$$q_{wi} = \left[ (T_{H_2O,TS_o} - T_{H_2O,TS_i}) \dot{m}_{H_2O,TS} c_{pH_2O} - \dot{Q}_{\text{gain,TS}} - \dot{Q}_{\text{cond}} \right] / (\pi d_i L) \quad (6)$$

where  $\dot{Q}_{\text{cond}}$  is heat conducted from upstream of the test section, numerically estimated for each set of test conditions. The average heat transfer coefficient is defined by equation (7):

$$HTC = q_{wi} / (T_{rb} - T_{wi}) \quad (7)$$

where  $T_{wi}$  is the average of the twelve temperature measurements in the wall of the test section.

The average pressure drop gradient is defined by equation (8):

$$dP/dZ = \Delta P_{TS} / \Delta Z \quad (8)$$

where  $\Delta Z$  is the distance between the pressure ports. The measurements and data reduction procedure are illustrated in Figure 9.

The uncertainties listed in Table 1 are obtained from two standard deviations of calibration, the resolution of calibration equipment and data loggers, and the stability of excitation voltages. The combined uncertainties are calculated according to ASME Performance Test Codes (1985) and Moffat (1988) and are shown as error bars in the plots in later chapters. Details of the uncertainty analysis are included in Appendix C.

### 3.2.2 Film thickness

The film thickness was measured with a resolution of 1800 by 1600 pixels at angles of  $0^\circ$ ,  $60^\circ$ ,  $90^\circ$ ,  $135^\circ$ ,  $180^\circ$ ,  $225^\circ$ ,  $270^\circ$ , and  $300^\circ$  clockwise from the bottom of the tube. For each angle and quality, four measurements were taken and averaged. There are two main data reduction steps for the film thickness: determine the minor diameter of the light ellipse in each image, and relate the minor diameter to a film thickness.

For the first step, image processing was performed using MATLAB. The code is included in Appendix D, but a brief overview is given here. The code is based on a program developed by Wujek (2011) that was then modified for this project's different image type and desired information. The program first converts the raw JPEG image file to a matrix of grayscale pixel values, and a Gaussian filter is applied to smooth out noise. A sample smoothed grayscale image is shown in Figure 10. The laser dot is identified by locating the circle of saturated pixels near the center of the image. Starting from the center of the laser dot, a set of vectors is defined at increments of  $2.5^\circ$ . Along each vector, the pixel values tend to follow the same general trend, as seen in Figure 11. Initially saturated by the laser dot, the values drop off and remain fairly flat as little light is reflected before the critical angle for reflection from the liquid-vapor or glass-vapor interface. As the critical angle is approached, the pixel intensity increases, reaches a maximum, and decreases again because little light is reflected at very wide angles. The program finds the local minimum and maximum pixel values corresponding to the pre-critical angle dark region and the reflection peak. The average of the minimum and maximum is calculated, and the program searches between those two extrema for the outermost pixel with a value less than or equal to the average. This point corresponds to the location of the critically reflected light, where

the intensity of light is changing most rapidly and the slope of the intensity plot is highest. After the critical point is found along each radial vector, an ellipse is fitted to the set of points, ignoring any outliers. The example image with its resulting ellipse is shown in Figure 12.

The scale of the image in pixels per millimeter is determined by identifying the dark areas at the top and bottom of the image, thus marking the boundaries of the tube, and counting the pixels between these boundaries. The tube diameter with the layer of tape was measured with calipers and found to be 10.1 mm. These two measurements provide a known scale by which the minor axis of the fitted ellipse is multiplied, giving the minor diameter in mm.

The second phase of the data reduction is to convert the minor diameter to a film thickness. This is achieved using a computational model developed and described by Wujek (2011). The model is necessary because the critical angle and film thickness in a round tube cannot be easily related by analytical equations like the ones for planar surfaces given by Shedd and Newell (1998). Instead, the model simulates the interactions of light with a tube and film. The MATLAB code is included in Appendix D and the complete description is provided by Wujek (2011), but again a brief overview is given here. The tube, liquid film, and vapor are assumed to be smooth coaxial cylinders with user-provided dimensions and indices of refraction. The model assumes a point source emitting light with intensity following a hemispherical Gaussian distribution. The light is divided into rays with initial angles from  $-\pi/2$  to  $\pi/2$  exclusive in increments of  $0.0025\pi$  relative to the normal of the tube outer surface. Each time a ray reaches an interface, it is either reflected or transmitted with a certain intensity and angle according to Snell's Law for transmission angles and Fresnel's equations for reflection intensities. The intensity is also affected by absorption

according to the Beer-Lambert law and diffusion as indicated by the inverse square law. The model follows each ray and records its location and intensity when it again reaches the outer surface of the tube. By collecting and interpolating the results of all of the rays, an image is created depicting the light intensity on the tube as viewed from the side. An example of a simulated image is shown in Figure 13. From the computed intensities, the minor diameter of the reflected light ellipse is determined and linked to the known liquid film thickness that was input into the model.

To use the model with the current experiments, the indices of refraction of the glass tube, liquid, and vapor were required. The refractive index of R134a vapor is essentially 1.00, but only approximate refractive indices for the tube and liquid were known from manufacturer specifications and scientific literature. Therefore, the model was calibrated using experimental results from each extreme of the range of enthalpies tested, where the tube was filled either with only superheated vapor or only condensed liquid. The average minor diameter measured under superheated conditions was compared to the diameter predicted by the model when given various tube indices of refraction. The index of refraction found to most closely match the experimental results was 1.385. Using this value for the tube, the predicted minor diameters for zero film thickness and various vapor indices of refraction were compared to the average measured diameter under subcooled conditions. The resolution of the model is such that the predicted diameter never quite matches the measured value. Since the refractive index decreases as the temperature rises, and the liquid temperature in the subcooled zone is the lowest in the range of experiments, the lower of the two refractive indices generating the closest match was chosen for liquid R134a. The selected value was 1.195, which is near the value reported by Fukuta et al.

(2004) of 1.197 for R134a at 50°C. Once the indices of refraction were determined, the model was run for a range of film thicknesses from zero to 3 mm. The computed minor diameters are plotted in Figure 14. A curve fit from the model results is applied to the experimental results to convert the minor diameters to film thicknesses. The refractive indices are assumed to be constant, and variations in the tube thickness are assumed to be negligible. The effect of viewing angle is also neglected.

The perceived minor diameter is affected by the viewing angle, the angle between a line passing through the center of the light ellipse and a line normal to the camera. In practice, a change in viewing angle would be caused by the tube not being centered around the laser dot, since the position of the laser is fixed relative to the camera. The effect of viewing angle on the calculated minor diameter is illustrated in Figure 15. The largest viewing angle possible with the measurement method used is 45°, if the center of the laser dot were even with one of the tube edges. Based on the distance between the laser dot center and the tube centerline in the images, the actual maximum is approximately 15°, and most of the images have viewing angles less than 10°. Therefore, the effect of viewing angle was neglected.

Variations in the viewing angle are one potential source of uncertainty in the film thickness measurements. Other sources include uncertainty in the indices of refraction and tube dimensions input into the model, noise in the pixel values of the image, and uncertainty associated with the curve fit from the model results. Based on the standard deviation of measurements of the dry tube with only vapor inside, the first order uncertainty is estimated to be approximately  $\pm 0.05$

mm. Additional uncertainty arises in the liquid film thickness measurements due to waviness or temporal variations in the film.

### 3.2.3 Visualization

In the visualization section, video was recorded at 1000 frames per second at a resolution of 512 by 512 pixels. The recorded videos were processed using Phantom Cine Viewer software from Vision Research. For the purposes of viewing flow regimes, the only processing performed was the application of a sharpening filter and the adjustment of brightness, gain, and gamma settings as necessary. The average enthalpy of the refrigerant in the visualization section is determined from a water side energy balance as shown in equations (9) - (12).

$$\Delta h_{\text{vis}} = \left[ (T_{\text{H}_2\text{O,vis,o}} - T_{\text{H}_2\text{O,TS,o}}) \dot{m}_{\text{H}_2\text{O,TS}} c_{\text{PH}_2\text{O}} \right] / \dot{m}_{\text{r}} \quad (9)$$

$$h_{\text{vis,i}} = h_{\text{TS,o}} = h_{\text{b,MC}} - \Delta h_{\text{PC}} - \Delta h_{\text{TS}} \quad (10)$$

$$h_{\text{vis,o}} = h_{\text{vis,i}} - \Delta h_{\text{vis}} \quad (11)$$

$$h_{\text{vis}} = (h_{\text{vis,i}} + h_{\text{vis,o}}) / 2 \quad (12)$$

### 3.3 Figures

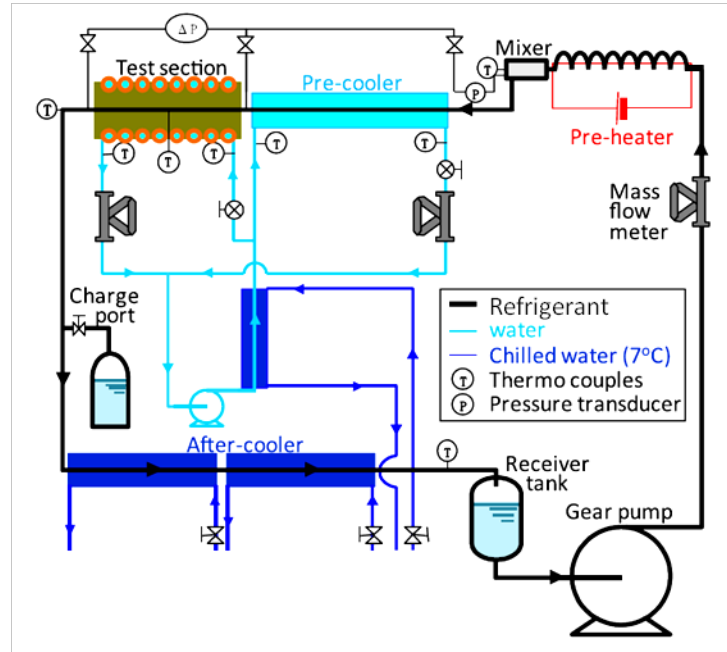


Figure 5: Schematic of experimental facility used for previous heat transfer and pressure drop measurements (Kondou and Hrnjak, 2011a)

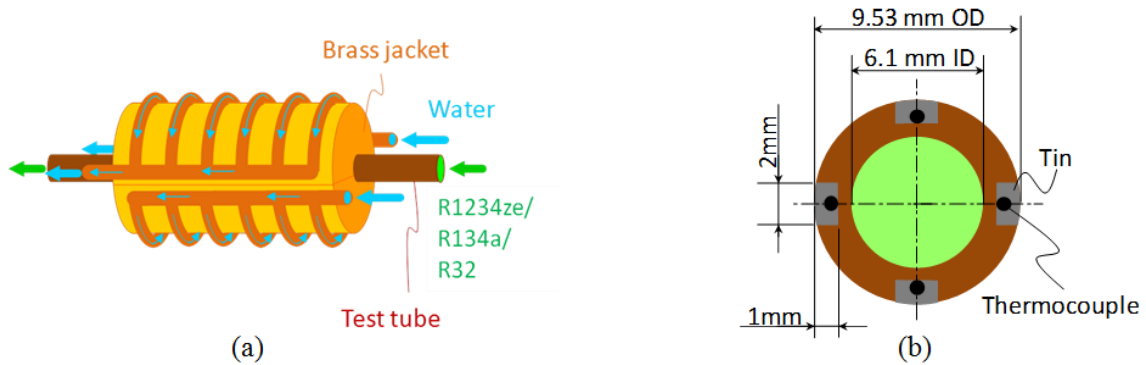


Figure 6: (a) Test section with fluid flow directions (b) Cross-section of test tube (Kondou and Hrnjak, 2011b)

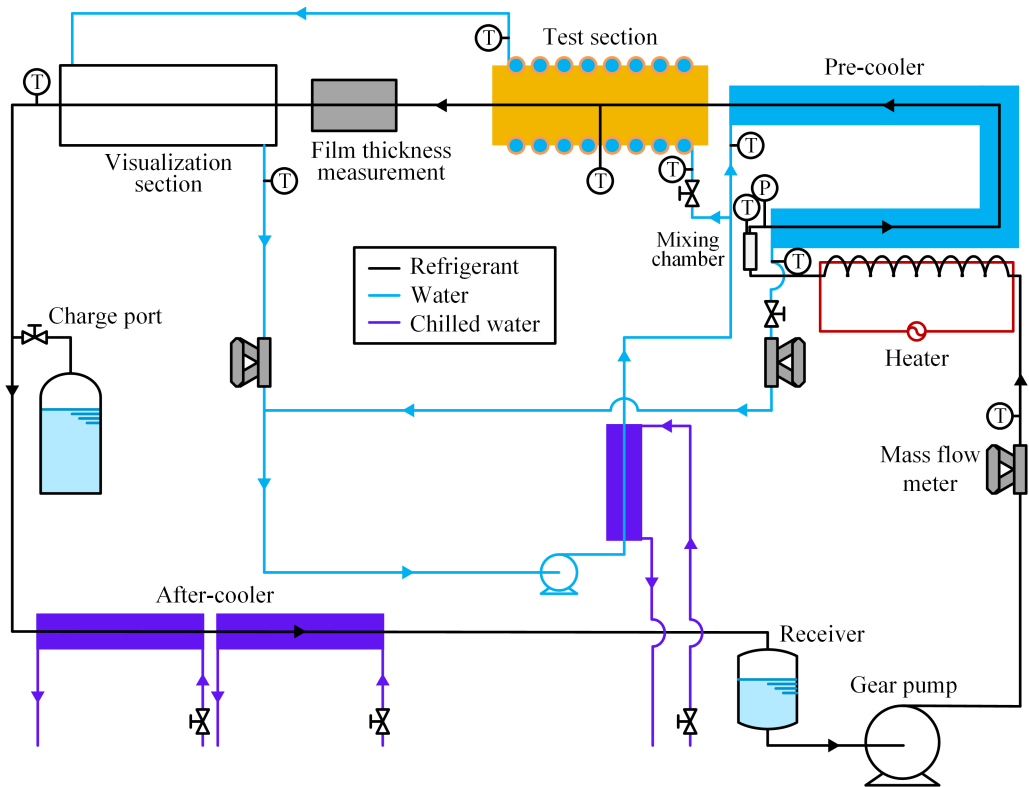


Figure 7: Schematic of experimental facility used for visualization, heat transfer, and film thickness measurements

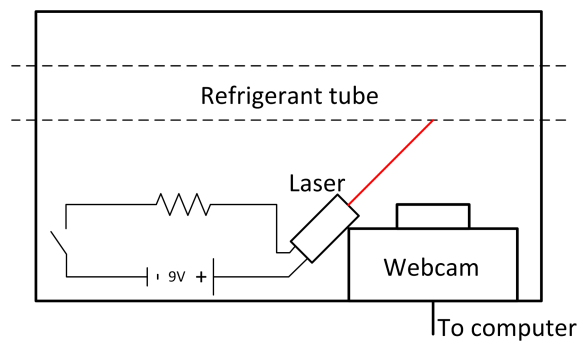


Figure 8: Top view of film thickness measurement device

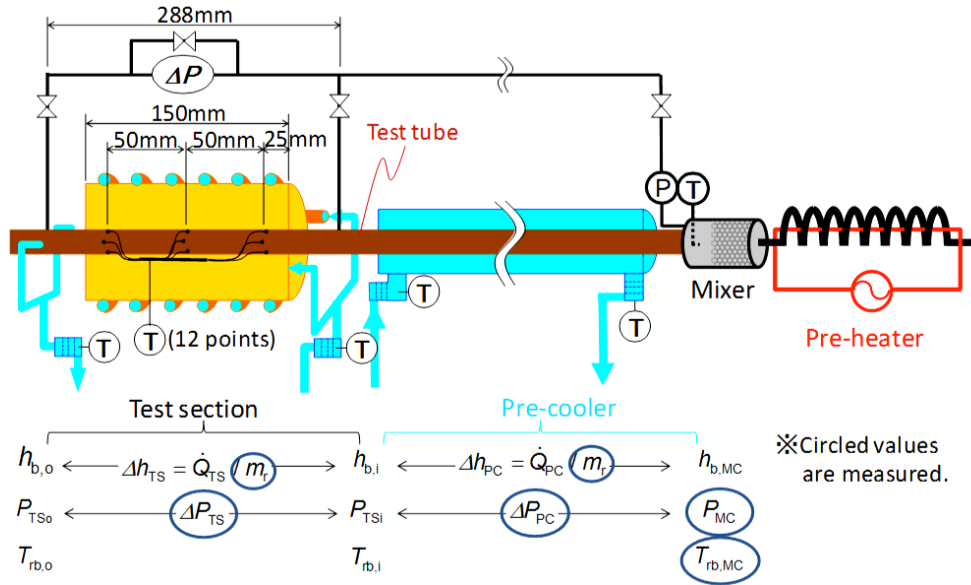


Figure 9: Measurement locations and data reduction procedure (Kondou and Hrnjak, 2011b)

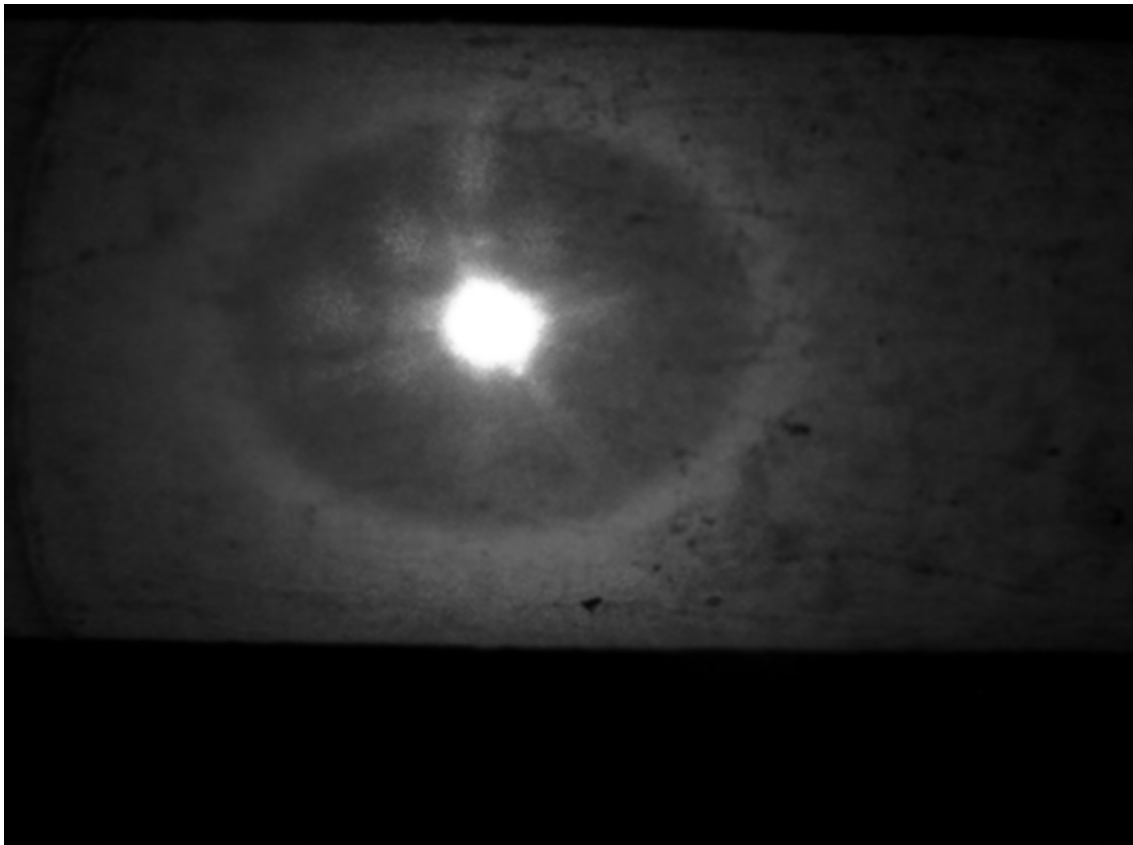


Figure 10: Film thickness image example after conversion to grayscale and application of a smoothing filter

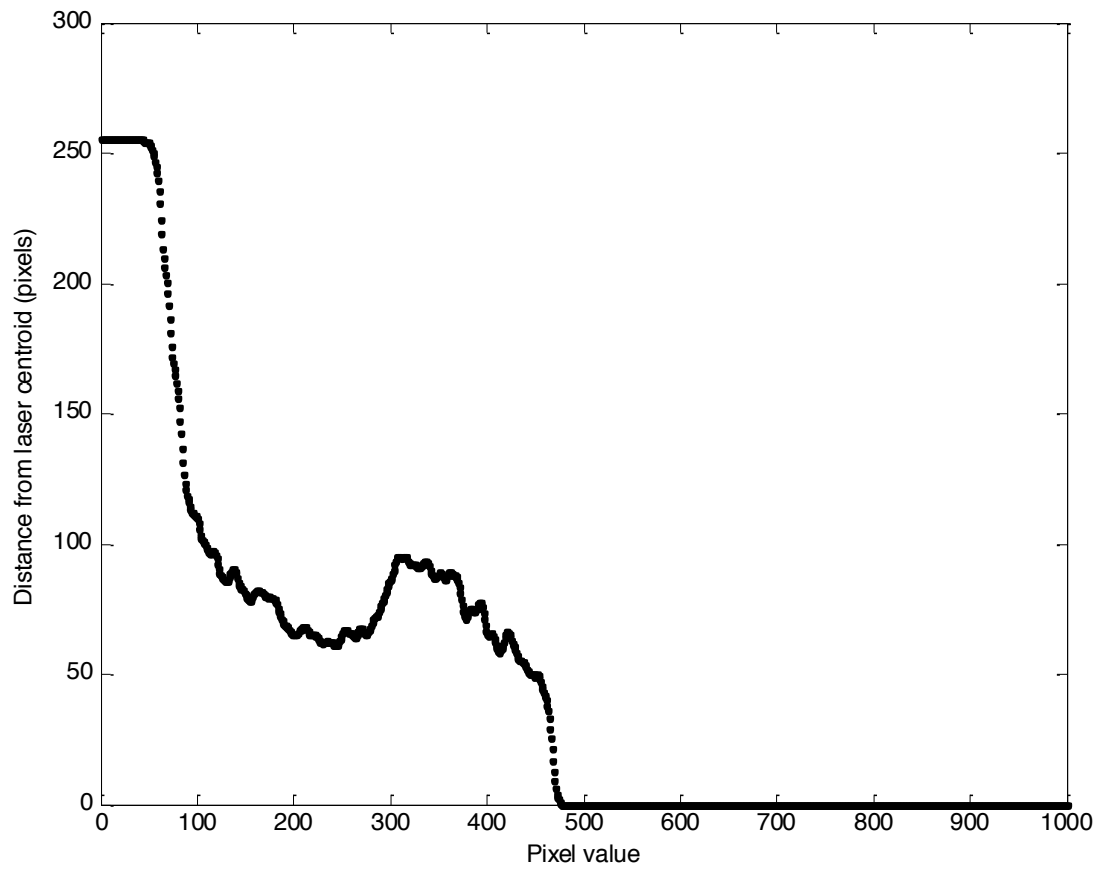


Figure 11: Pixel values along one vector radiating out from the laser centroid, taken from the sample image in Figure 10

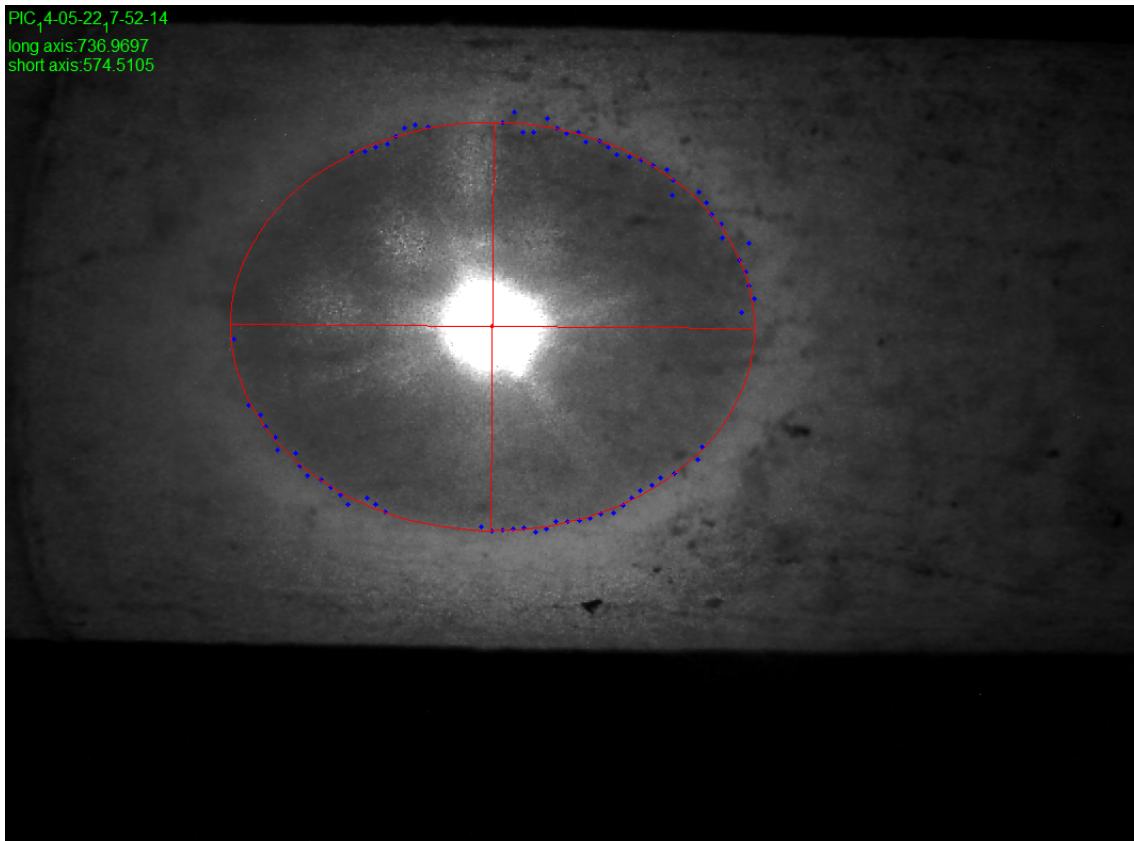


Figure 12: Sample image with critical reflection points and best fit ellipse

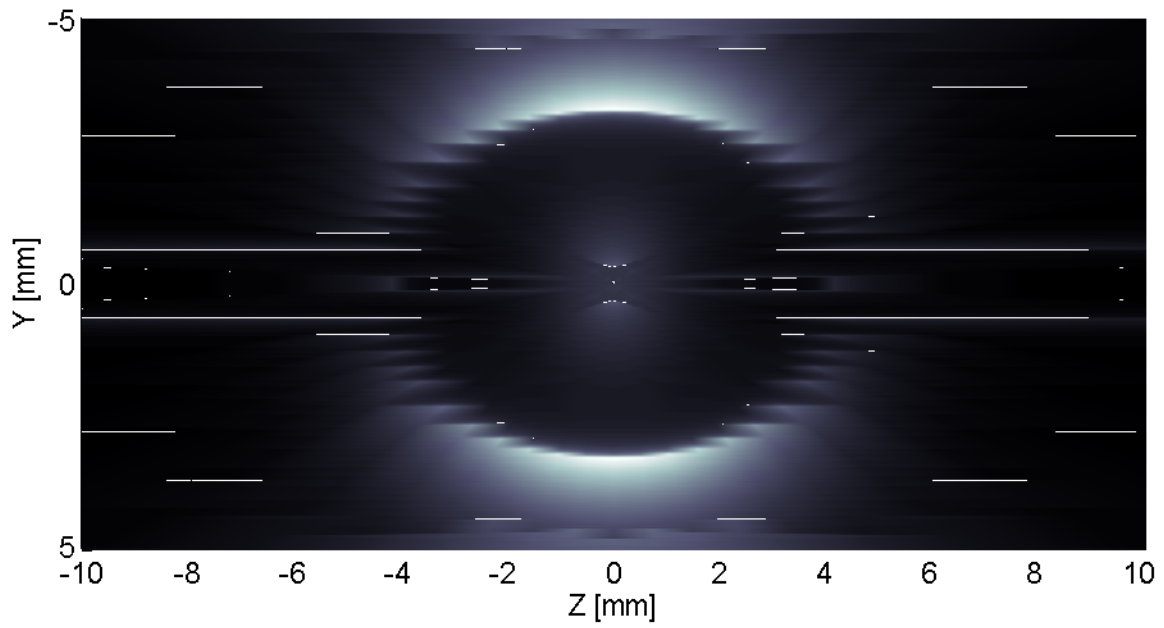


Figure 13: Example light reflection image simulated by the optical model used for film thickness calibration

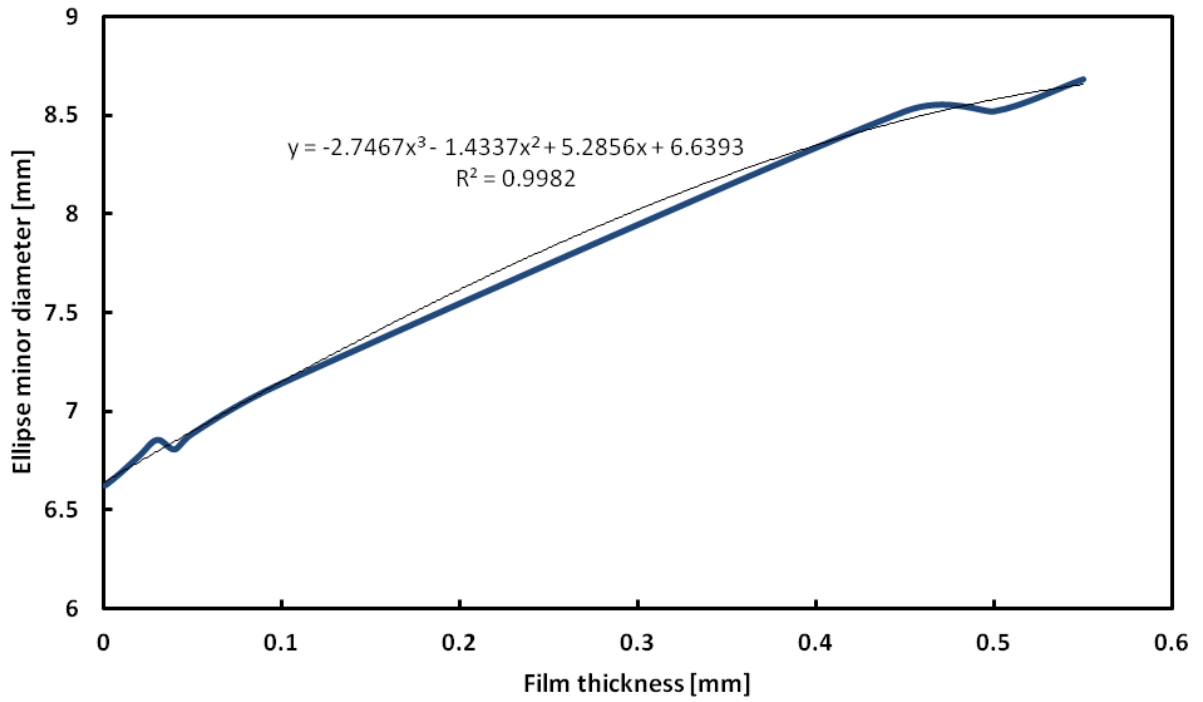


Figure 14: Optical model results and calibration curve fit

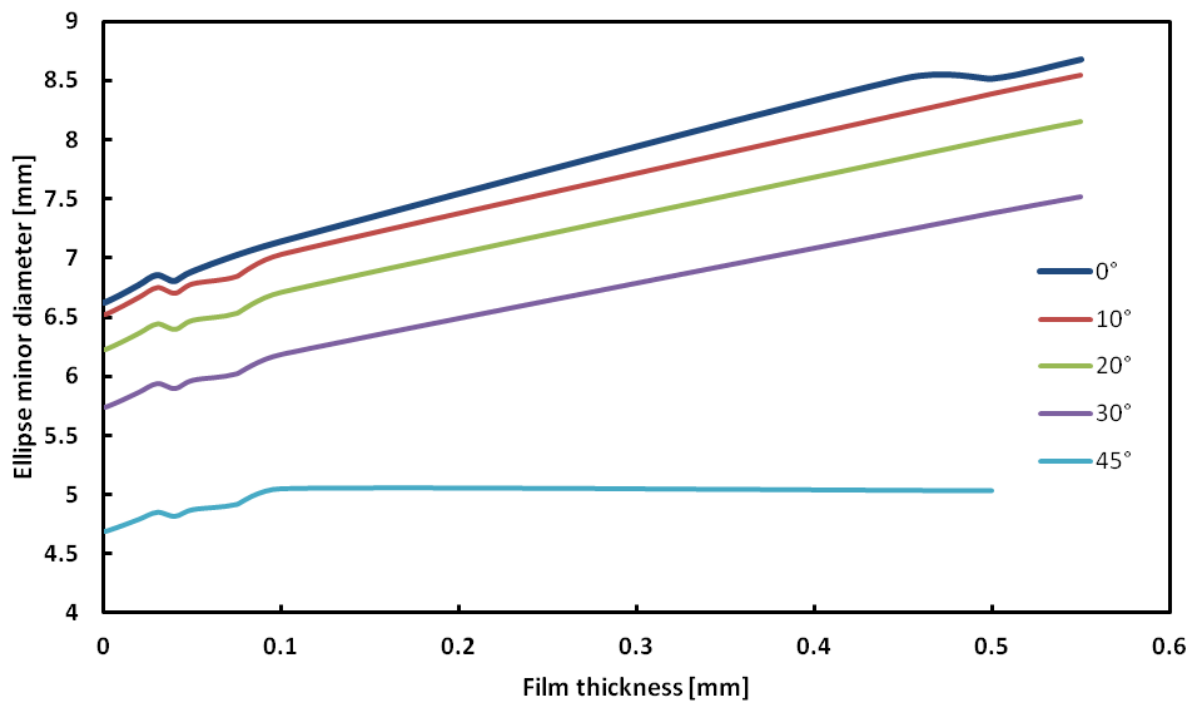


Figure 15: Effect of viewing angle on the apparent minor diameter in film thickness images

### 3.4 Tables

Table 1: Measurement uncertainties

<b>Measured variable</b>	<b>Instrument</b>	<b>Uncertainty</b>
$T_{rb}, T_{H_2O}$	Sheathed T-type thermocouple	$\pm 0.05$ K
$T_{wi}$	Twisted T-type thermocouple	$\pm 0.16$ K
$P_{MC}$	Diaphragm absolute pressure transducer	$\pm 4$ kPa
$\Delta P$	Diaphragm differential pressure transducer	$\pm 0.13$ kPa
$\dot{m}_{H_2O,TS}, \dot{m}_r$	Coriolis mass flow meter	$\pm 0.1$ g/s
$\dot{m}_{H_2O,PC}$	Coriolis mass flow meter	$\pm 0.5$ g/s

## CHAPTER 4: RESULTS AND DISCUSSION

### 4.1 Heat transfer

Figure 16 shows the heat transfer results for R134a at 1.319 MPa with a mass flux of  $100 \text{ kg m}^{-2} \text{ s}^{-1}$ , a heat flux of  $10 \text{ kW m}^{-2}$ , and bulk enthalpies ranging from  $227 \text{ kJ kg}^{-1}$  to  $483 \text{ kJ kg}^{-1}$ . The heat transfer coefficients display the same trend seen in earlier results reported by Kondou and Hrnjak (2011a, 2011b, 2012) and Agarwal and Hrnjak (2013), i.e. the dramatic increase prior to the saturated vapor point and the smooth transition from the single-phase region to the two-phase region. The vertical dashed lines indicate the borders of the superheated (SH), condensing superheated (CSH), two-phase (TP), condensing subcooled (CSC), and subcooled (SC) regions. The beginning of the CSH zone is identified as the point at which the wall temperature falls below the saturation temperature, as seen in Figure 16(a). In the CSH zone, the outlet temperature of the refrigerant is lower than the inlet temperature, indicating sensible heat loss in addition to the latent heat loss as condensation begins. The CSH zone ends and the TP zone begins at the saturated vapor enthalpy. This transition is visible experimentally by the overlapping inlet and outlet refrigerant temperatures, indicating that the bulk refrigerant temperature has reached the saturation temperature and latent heat transfer is dominant. The inlet and outlet bulk refrigerant temperatures are also shown in Figure 16(a).

The solid line in Figure 16(b) represents the HTC's predicted by the model proposed by Agarwal and Hrnjak (2013), which utilizes the Gnielinski (1976), Kondou-Hrnjak (2012), and Cavallini et al. (2006) correlations. The model assumes the nominal experimental conditions at all points. The experimental results agree with the predictions within 40 percent, with the greatest discrepancy occurring in the two-phase region at high qualities.

## 4.2 Visualization

High-speed video footage was recorded for R134a at a pressure of 1.319 MPa with a mass flux of  $100 \text{ kg m}^{-2} \text{ s}^{-1}$  and bulk enthalpies ranging from  $223 \text{ kJ kg}^{-1}$  to  $469 \text{ kJ kg}^{-1}$ . The heat flux in the visualization section varied from 20 to 60 percent of the heat flux in the test section. The video conditions are summarized on a T-h diagram in Figure 17. Figure 18 through Figure 43 are representative still images from the videos, in order of decreasing enthalpy. The dark horizontal lines near the top and bottom of each image are the boundaries of the glass refrigerant tube; since the images are a flat projection of a curved surface, multiple lines are present and indicate the front and back inner surfaces of the tube as well as the outer surface of the refrigerant tube. The magnification of the images is such that the edges of the water tube are not shown. The water itself is also not visible since no air or vapor was in the water to allow waves or bubbles to form. Therefore, the fluid movement seen in the videos and indicated in the still images is the movement of the refrigerant.

In Figure 18, the bulk refrigerant enthalpy is just at the border of the superheated and condensing superheated zones, and only vapor is visible (the droplets seen in the image are stationary and located on the outside of the visualization section). Figure 19 and Figure 20 are taken from the first video with evidence of condensation. Although difficult to see in the still image, traces of slow-moving fog were barely visible at the top and bottom of the tube in the video. Condensation is more apparent in Figure 21, with a bulk enthalpy of  $451 \text{ kJ kg}^{-1}$ . In the video corresponding to this image, liquid droplets are seen entrained in the vapor in the center of the tube and moving along the wall of the tube, forming rivulets. These rivulets then merge and spiral downward along the tube wall, beginning to form a film, particularly at the bottom of the tube, as shown in

Figure 22. Figure 23, at a bulk enthalpy of  $446 \text{ kJ kg}^{-1}$ , shows an annular film with fast-moving waves, while Figure 24 at  $444 \text{ kJ kg}^{-1}$  shows a similar film as well as many small droplets entrained in the vapor. In Figure 25 through Figure 36, the annular film continues to deepen at the bottom of the tube, and larger waves form. Eventually, the waves become so large that they sometimes reach the top of the tube, as seen in Figure 37, which corresponds to a bulk enthalpy of  $322 \text{ kJ kg}^{-1}$ . Transitions to slug and plug flow follow, with periods of liquid-filled tube alternating with large vapor pockets near the top of the tube, as illustrated in Figure 38. As the enthalpy continues to decrease, the air pockets shrink and become less frequent, as represented in Figure 39. By an enthalpy of  $262 \text{ kJ kg}^{-1}$ , liquid fills the entire tube, but the presence of vapor is still indicated by light-colored swirls flowing in the middle of the tube, as shown in Figure 41 and Figure 42. Eventually, these swirls disappear and the refrigerant is completely liquid, as seen in Figure 43. During the video represented by Figure 43, condensation from the ambient air was present on the outer surface of the water tube in the visualization section, which accounts for the droplets appearing in the image.

The videos discussed above support the hypothesis behind the five-zone model of condensation. Liquid is clearly present at bulk enthalpies above saturation; Figure 19 through Figure 25 correspond to the CSH zone. Similarly, Figure 41 and Figure 42 show refrigerant with bulk enthalpies in the CSC zone, and some vapor is still perceptible. In addition to this qualitative confirmation, the videos can be used to advance the five-zone condensation model by indicating the physical flow patterns and thus the correlation types which should be applied in the CSH zone. For instance, initially the condensation appears similar to the Nusselt falling-film model, while later it displays annular flow with waves.

### 4.3 Film thickness

The liquid film thickness was measured for condensing R134a at 1.319 MPa with a mass flux of  $100 \text{ kg m}^{-2} \text{ s}^{-1}$ , a heat flux of  $10 \text{ kW m}^{-2}$ , and bulk enthalpies ranging from  $225 \text{ kJ kg}^{-1}$  to  $479 \text{ kJ kg}^{-1}$ . The measured film thicknesses at each enthalpy are plotted as cross-sectional views of the refrigerant tube in Figure 44 through Figure 70. The film is generally thicker on the bottom of the tube than on the sides and top, as the videos also revealed. The film thickness increases overall as the enthalpy decreases. This trend is illustrated in Figure 71 through Figure 78, which show the film thickness at each circumferential location as a function of enthalpy. These figures show that the film on the upper half of the tube remains very thin until a bulk enthalpy of about  $325 \text{ kJ kg}^{-1}$ , a quality of about 0.35. However, the film thickness on the bottom half of the tube increases fairly consistently as the bulk enthalpy falls below approximately  $450 \text{ kJ kg}^{-1}$ , while the two-phase zone does not begin until the saturated vapor point at a bulk enthalpy of  $423 \text{ kJ kg}^{-1}$ . These results thus further support the hypothesis of a condensing superheated zone.

The film thicknesses at each enthalpy were integrated with respect to the radial angle to estimate the cross-sectional area occupied by liquid. This liquid area was then used to calculate the void fraction. The estimated void fractions are plotted as a function of enthalpy in Figure 79. The void fraction starts around 1.0 in the superheated region and then slowly decreases with decreasing enthalpy, remaining above 0.9 until the refrigerant reaches a bulk enthalpy of approximately  $325 \text{ kJ kg}^{-1}$ , corresponding to a quality of 0.35. The void fraction then begins to drop more sharply but somewhat levels out around 0.65 as the refrigerant reaches the subcooled zone instead of falling to zero as expected. This discrepancy is likely due to the inaccuracy of the film thickness measurements at lower qualities. The film thickness measurement and calibration method relies

on the assumption of essentially annular flow, but this assumption becomes less valid as condensation progresses and the flow transitions to wavy, slug, and plug flow regimes. The experimentally estimated void fractions are compared to those predicted by the five-zone model proposed by Agarwal and Hrnjak (2013) for R134a at 1.319 MPa with a mass flux of  $100 \text{ kg m}^{-2} \text{ s}^{-1}$ . The model predictions are calculated from the Smith (1969) correlation (see equation (13)), and are shown as a solid line in Figure 79. The experimental values are near the model values until a bulk enthalpy of approximately  $350 \text{ kJ kg}^{-1}$ , corresponding to a quality of about 0.5, after which the deviation increases as the model void fractions fall to zero. In the initial similar region, the experimental void fractions are consistently lower than the model predictions.

$$\varepsilon = \left[ 1 + \frac{\rho_v}{\rho_l} \left( \frac{1-x}{x} \right) \left( 0.4 + 0.6 \left( \frac{\rho_l/\rho_v + 0.4(1-x)/x}{1 + 0.4(1-x)/x} \right)^{0.5} \right) \right]^{-1} \quad (13)$$

#### 4.4 Pressure drop

The start of condensation prior to the bulk saturated vapor point that is suggested by the heat transfer results and supported by the visualization and film thickness results is also manifested in the pressure drop. Figure 80 shows previous experimental heat transfer and pressure drop results for R32 at a pressure of 3.141 MPa (corresponding to a saturation temperature of  $50 \text{ }^\circ\text{C}$ ), a mass flux of  $300 \text{ kg m}^{-2} \text{ s}^{-1}$ , and a heat flux of  $10 \text{ kW m}^{-2}$ . Figure 80 is based on data collected by Agarwal and Hrnjak (2013). The Cavallini et al. (2006), Kondou-Hrnjak (2012), and Gnielinski (1976) correlations are shown as a solid line in the two-phase, CSH, and superheated zone, respectively, of Figure 80(b). The Colburn (1933) and Friedel (1979) are shown as examples of single-phase and two-phase pressure drop correlations in Figure 80(c). The dashed vertical lines indicate the boundaries of the CSH zone, which is identified using the experimentally measured

temperatures shown in Figure 80(a). The CSH zone begins when the test section wall temperature falls below the saturation temperature. At that point, condensation begins and is indicated by the sharp rise in heat transfer coefficient and pressure drop gradient, as seen in Figure 80(b) and (c). However, the bulk refrigerant temperature at the test section is still superheated and drops from the inlet to the outlet, as seen in Figure 80(a), due to continuing sensible heat transfer. Once the bulk refrigerant reaches saturated vapor conditions, it enters the two-phase zone and there is primarily latent heat transfer. The trends shown in Figure 80(a) and (b) are thus similar to those for R134a discussed in Section 3.1, and likewise demonstrate the existence of a condensing superheated region. Figure 80(c) shows that the existence of the CSH region is also revealed in the pattern of the pressure drop.

In the superheated region, the experimental pressure drop is near to the value predicted by the Colburn (1933) correlation, which predicts that the pressure drop will decrease as the bulk enthalpy decreases due to the reduction in specific volume and thus velocity. However, rather than continuing to follow that trend in the CSH region, the pressure drop increases as the bulk enthalpy decreases once condensation begins. In the two-phase region, the experimental pressure drop follows the general trend predicted by the Friedel (1979) correlation, first increasing to a maximum at a quality of about 0.92 and then decreasing as the enthalpy decreases further, as seen in Figure 80(c).

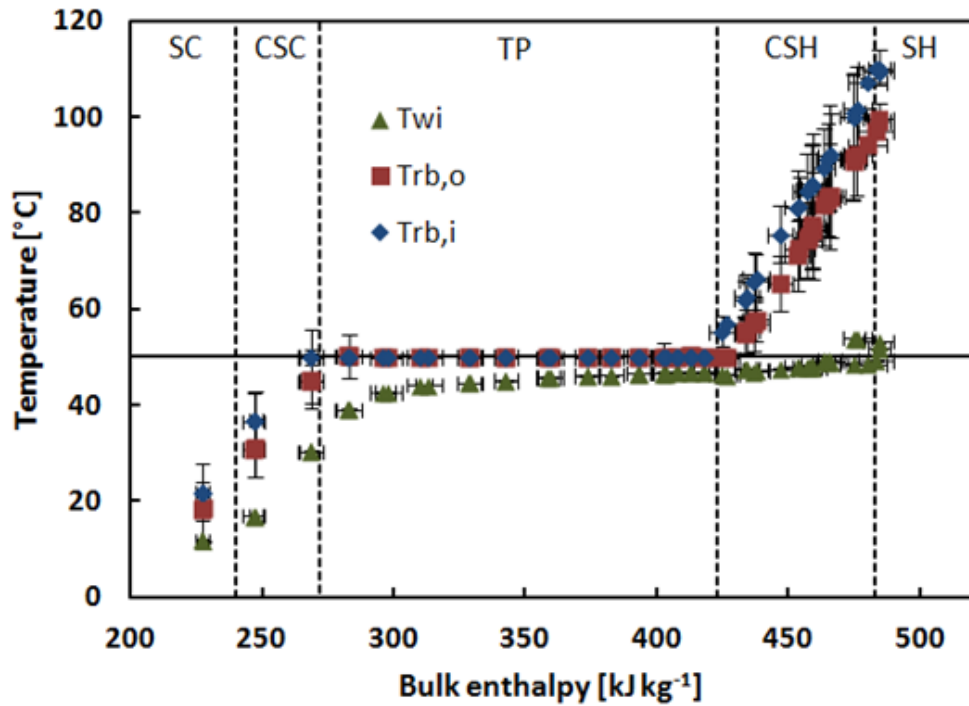
The pressure drop is higher than predicted by the Colburn (1933) correlation in the CSH zone because the single-phase model does not take into account the shear interactions between the vapor and the liquid film that begins to form as condensation starts before the two-phase region.

The energy dissipated by these interactions leads to an escalation in pressure drop. The phenomenon is indicated by the Friedel (1979) correlation, which predicts an initial increase in pressure drop during the early stages of condensation. However, the Friedel (1979) correlation, applied only in the two-phase region, shows the rise in pressure drop beginning too late. The causes for the observed trend are therefore accepted already but have been assumed to be relevant only in the two-phase region, when actually they should be considered as soon as condensation starts in the condensing superheated zone. The assumptions about the appearance of condensate under the three-zone and five-zone models are illustrated in Figure 81.

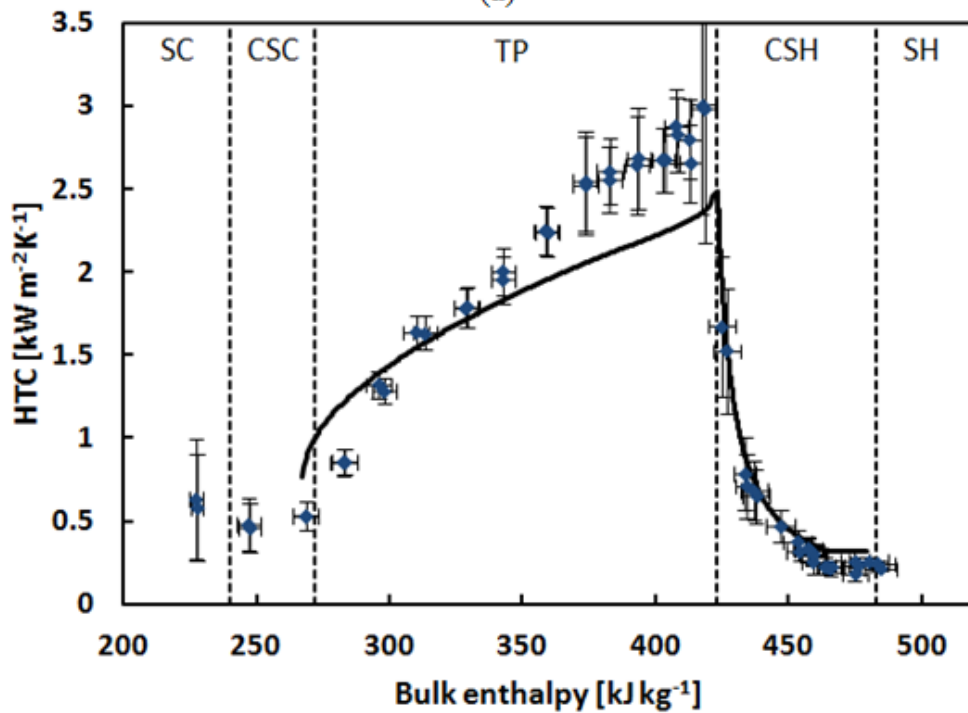
The pressure drop begins to rise at the beginning of condensation as enough liquid condenses to form a film all around the tube. As condensation continues and the liquid film thickens, more waves form and increase the shear at the liquid-vapor interface, further increasing the pressure drop. Simultaneously however, the density of the refrigerant is increasing, so the velocity is decreasing with a constant mass flux. The refrigerant density and velocity are shown as functions of specific enthalpy in Figure 82, assuming no slip. As the velocity decreases, friction and momentum loss from the refrigerant are reduced. The peak and subsequent decrease in pressure drop as condensation progresses may be caused by the reduction of velocity enough to offset the effect of the thicker, wavier film. The liquid velocity appeared to decrease in the videos as the film deepened and became more wavy. The wave size and velocity can be quantified by analyzing the high-speed videos of the condensing refrigerant, but the videos immediately provide qualitative confirmation for the existence and flow pattern of the condensate in the CSH and two-phase zones. Although the fluid and conditions differ for the pressure drop and visualization results presented, the basic behavior of the refrigerant is expected to be similar, and the heat

transfer results demonstrate comparable trends.

#### 4.5 Figures



(a)



(b)

Figure 16: Experimental average wall temperatures, test section inlet and outlet bulk refrigerant temperatures, and heat transfer coefficients for R134a at 1.319 MPa with a mass flux of 100 kg m<sup>-2</sup> s<sup>-1</sup> and a heat flux of 10 kW m<sup>-2</sup>

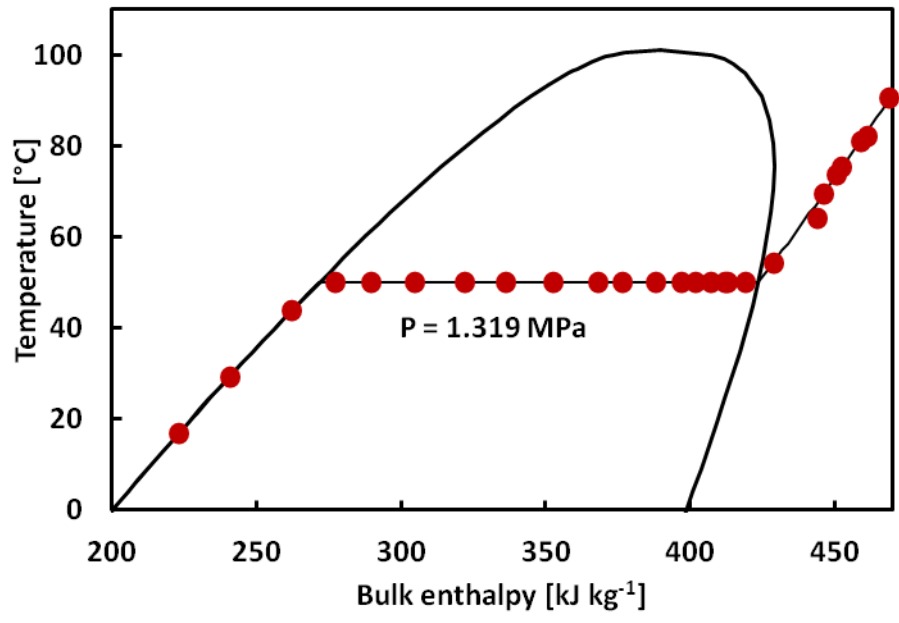


Figure 17: Average conditions of refrigerant during the recorded videos

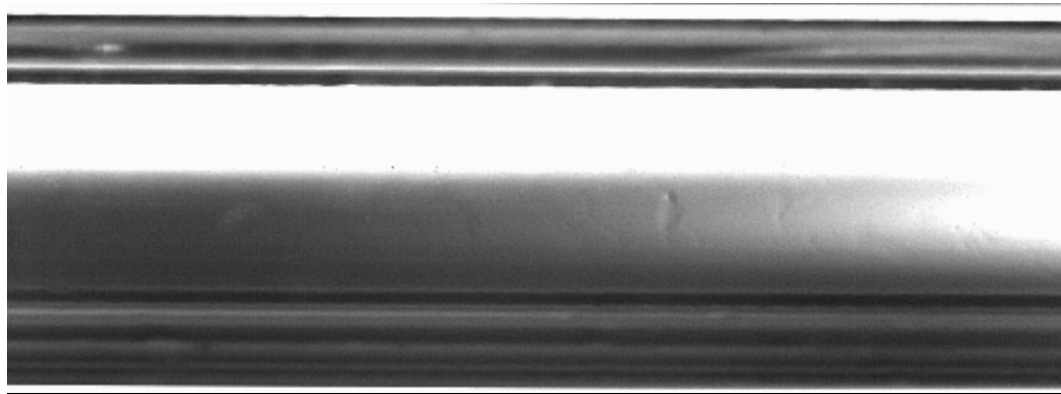


Figure 18: Still image from high-speed video of R134a with a bulk enthalpy of 469 kJ kg<sup>-1</sup>

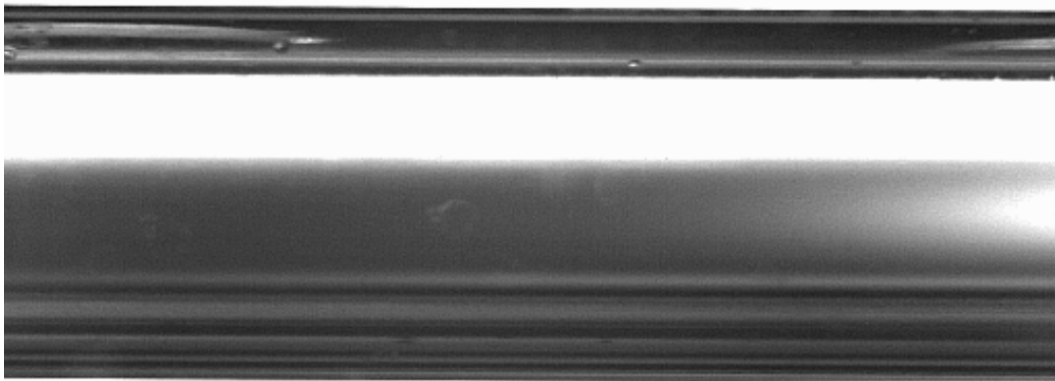


Figure 19: Still image from high-speed video of R134a with a bulk enthalpy of  $461 \text{ kJ kg}^{-1}$

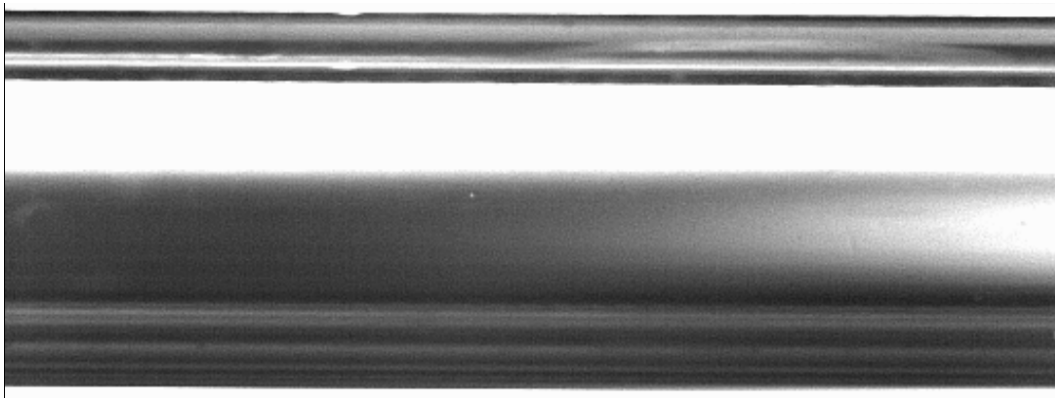


Figure 20: Still image from high-speed video of R134a with a bulk enthalpy of  $459 \text{ kJ kg}^{-1}$

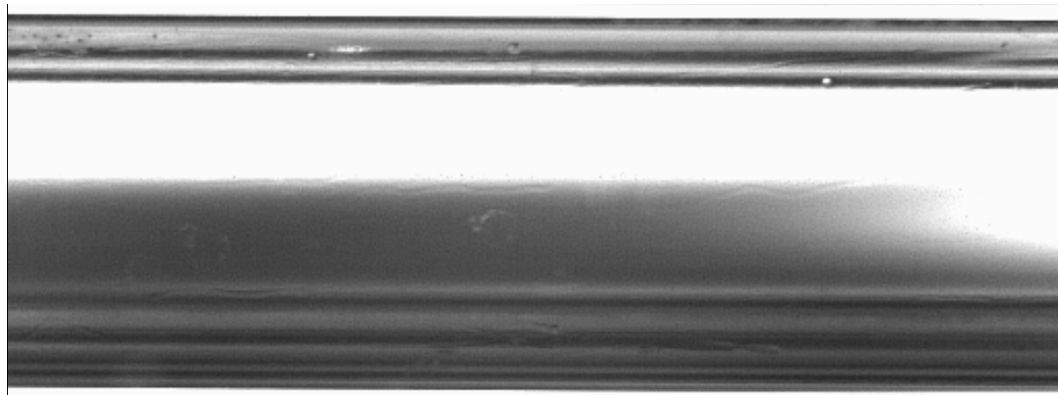


Figure 21: Still image from high-speed video of R134a with a bulk enthalpy of  $451 \text{ kJ kg}^{-1}$

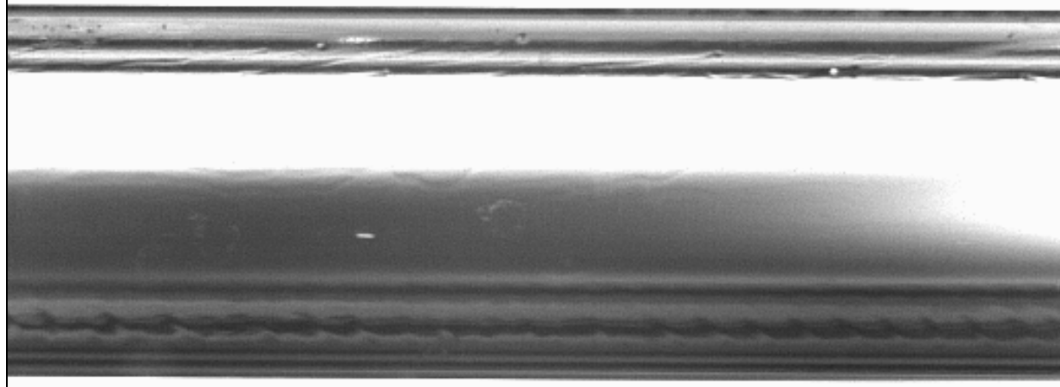


Figure 22: Still image from high-speed video of R134a with a bulk enthalpy of  $453 \text{ kJ kg}^{-1}$

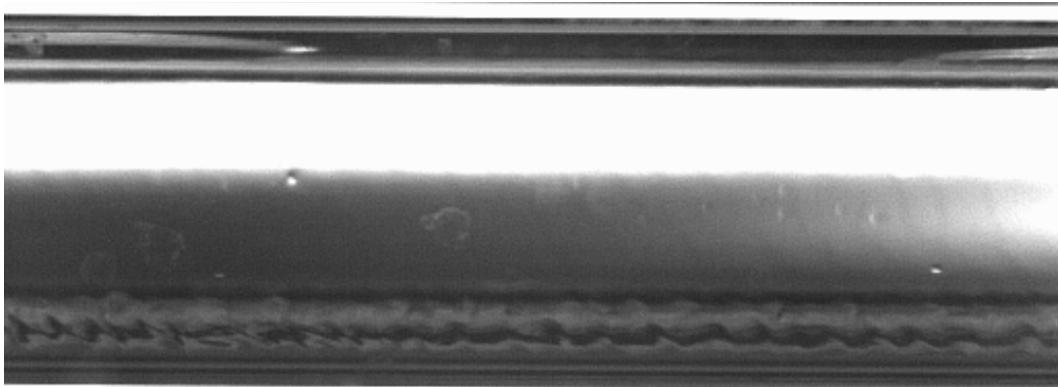


Figure 23: Still image from high-speed video of R134a with a bulk enthalpy of  $446 \text{ kJ kg}^{-1}$

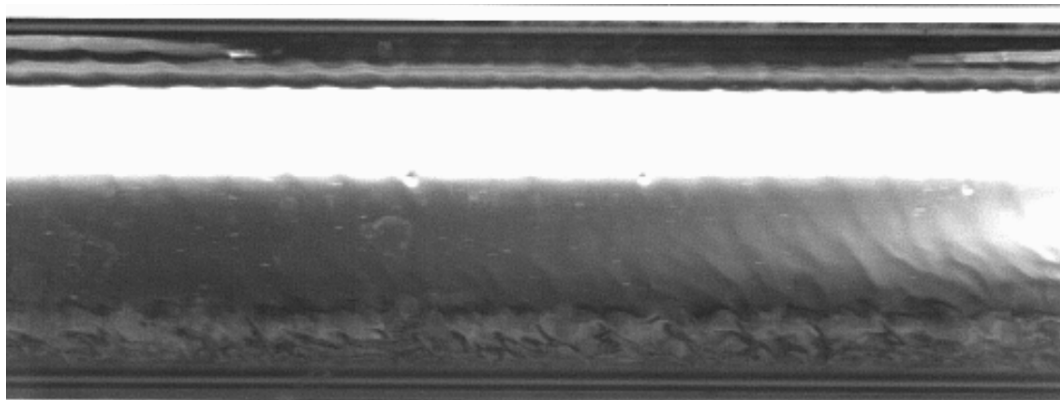


Figure 24: Still image from high-speed video of R134a with a bulk enthalpy of  $444 \text{ kJ kg}^{-1}$

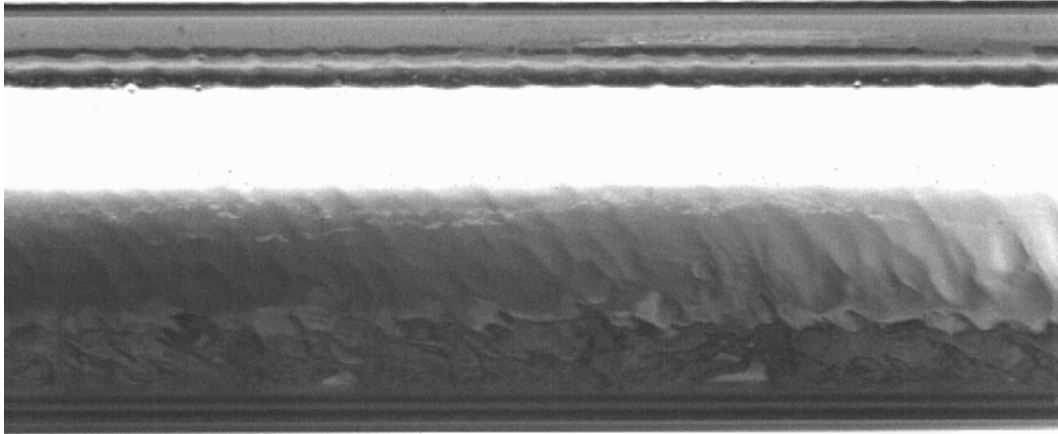


Figure 25: Still image from high-speed video of R134a with a bulk enthalpy of  $429 \text{ kJ kg}^{-1}$

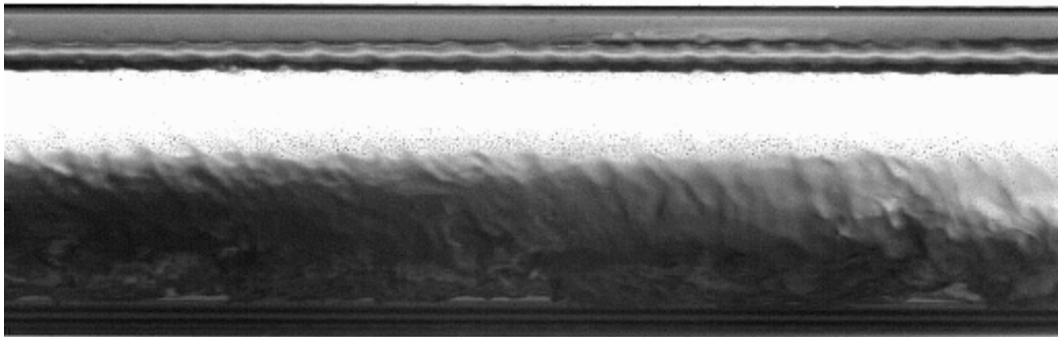


Figure 26: Still image from high-speed video of R134a with a bulk enthalpy of  $419 \text{ kJ kg}^{-1}$   
( $x=0.97$ )

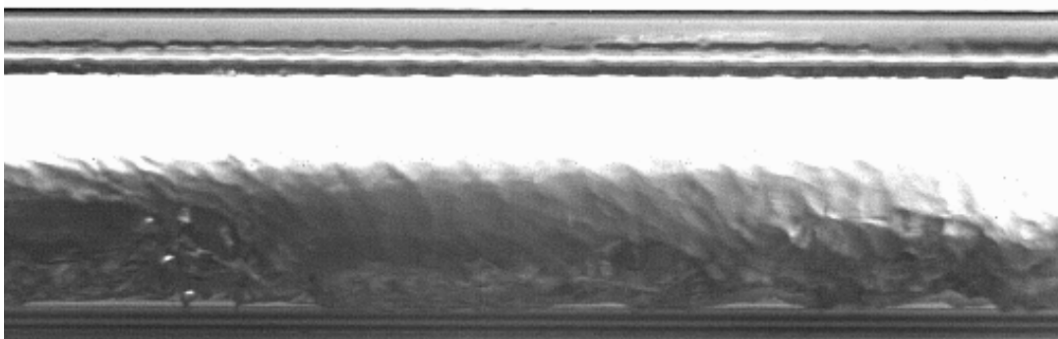


Figure 27: Still image from high-speed video of R134a with a bulk enthalpy of  $413 \text{ kJ kg}^{-1}$   
( $x=0.93$ )

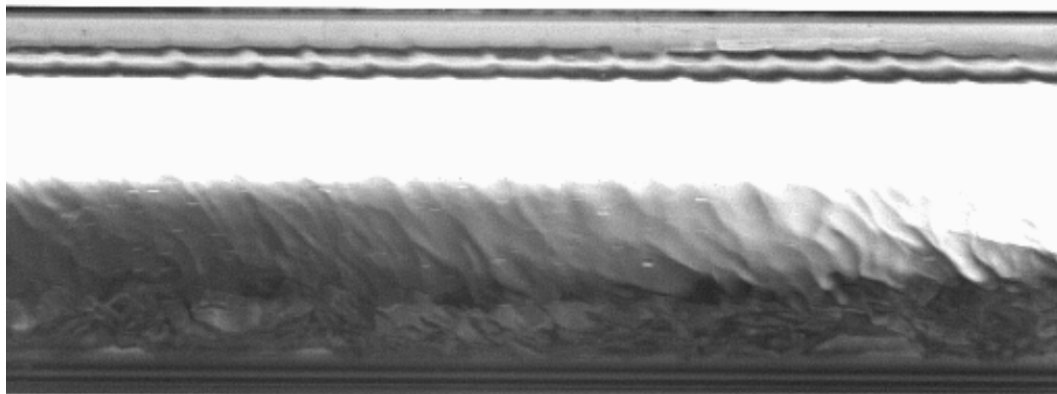


Figure 28: Still image from high-speed video of R134a with a bulk enthalpy of  $412 \text{ kJ kg}^{-1}$   
( $x=0.93$ )

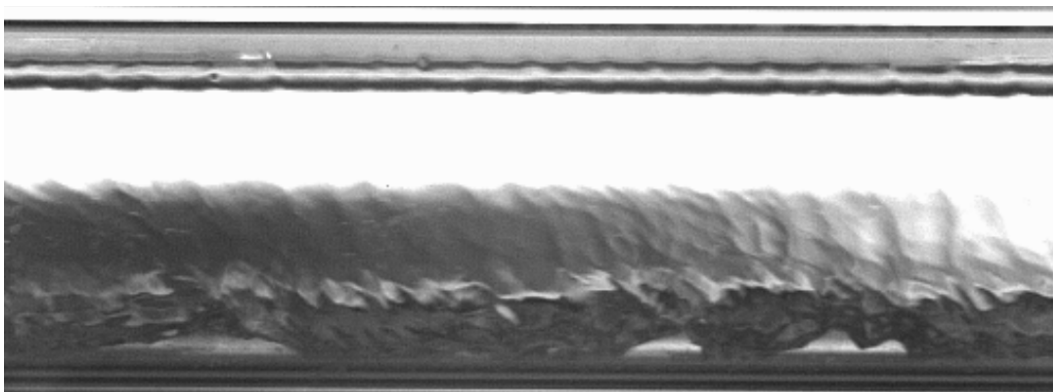


Figure 29: Still image from high-speed video of R134a with a bulk enthalpy of  $407 \text{ kJ kg}^{-1}$   
( $x=0.89$ )



Figure 30: Still image from high-speed video of R134a with a bulk enthalpy of  $402 \text{ kJ kg}^{-1}$   
( $x=0.86$ )

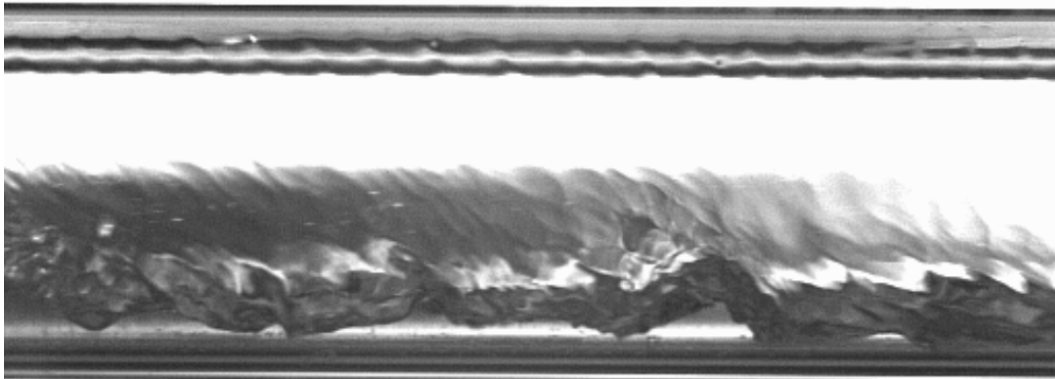


Figure 31: Still image from high-speed video of R134a with a bulk enthalpy of  $397 \text{ kJ kg}^{-1}$  ( $x=0.82$ )

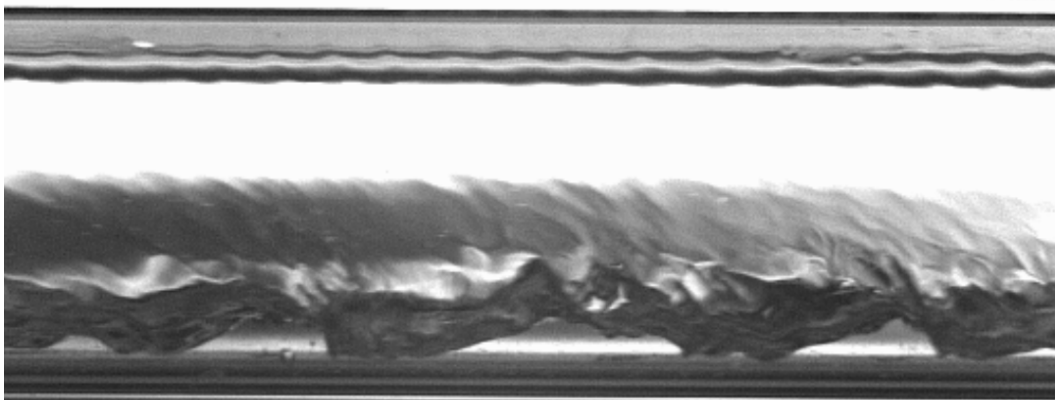


Figure 32: Still image from high-speed video of R134a with a bulk enthalpy of  $388 \text{ kJ kg}^{-1}$  ( $x=0.77$ )



Figure 33: Still image from high-speed video of R134a with a bulk enthalpy of  $376 \text{ kJ kg}^{-1}$  ( $x=0.69$ )

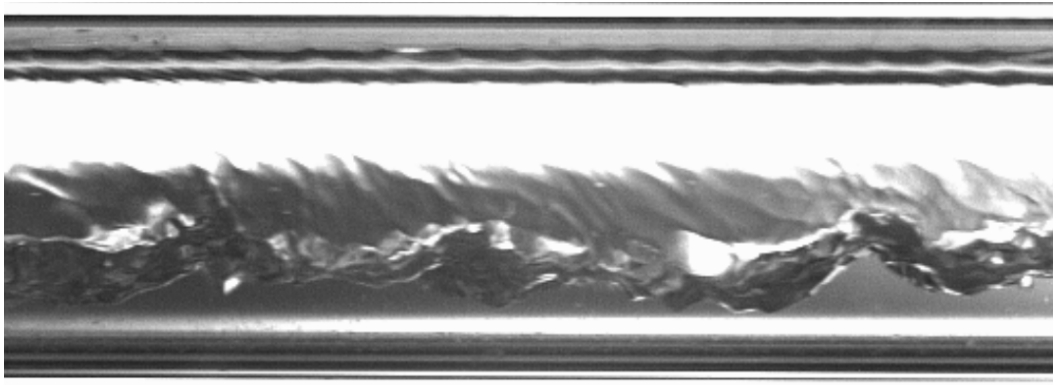


Figure 34: Still image from high-speed video of R134a with a bulk enthalpy of  $368 \text{ kJ kg}^{-1}$  ( $x=0.64$ )

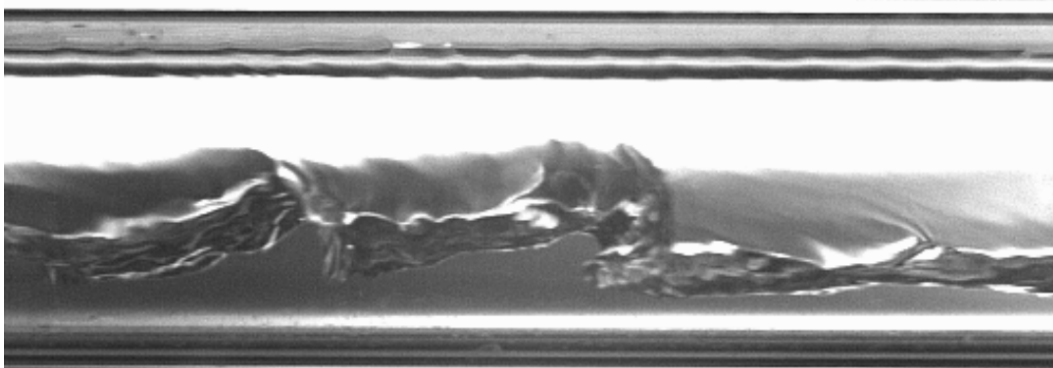


Figure 35: Still image from high-speed video of R134a with a bulk enthalpy of  $352 \text{ kJ kg}^{-1}$  ( $x=0.53$ )

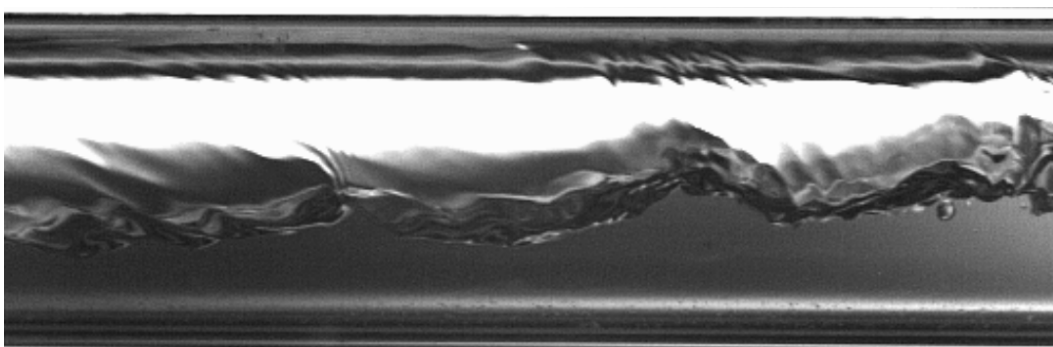


Figure 36: Still image from high-speed video of R134a with a bulk enthalpy of  $336 \text{ kJ kg}^{-1}$  ( $x=0.42$ )

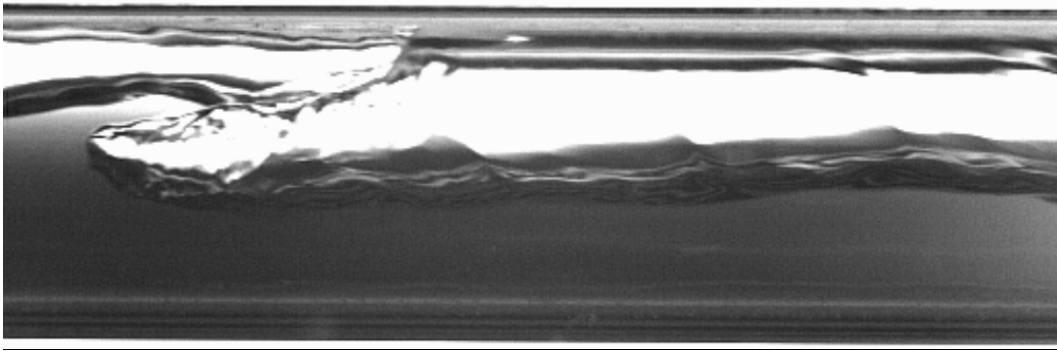


Figure 37: Still image from high-speed video of R134a with a bulk enthalpy of  $322 \text{ kJ kg}^{-1}$   
( $x=0.33$ )

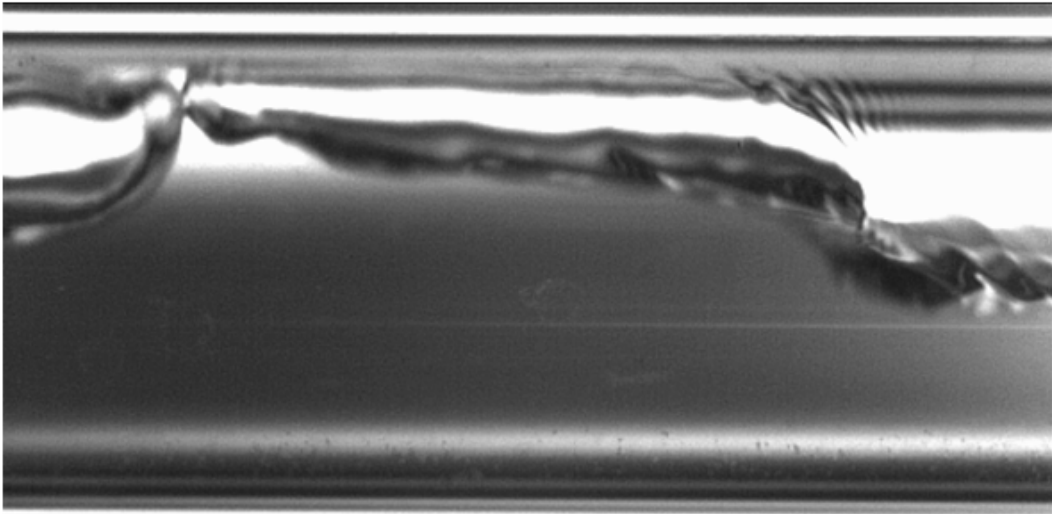
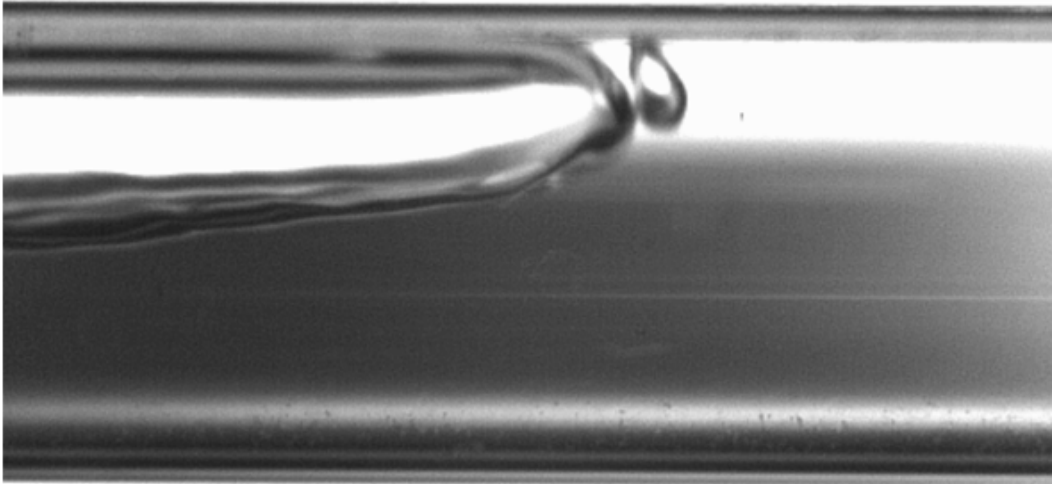


Figure 38: Still images from high-speed video of R134a with a bulk enthalpy of  $305 \text{ kJ kg}^{-1}$  ( $x=0.22$ )

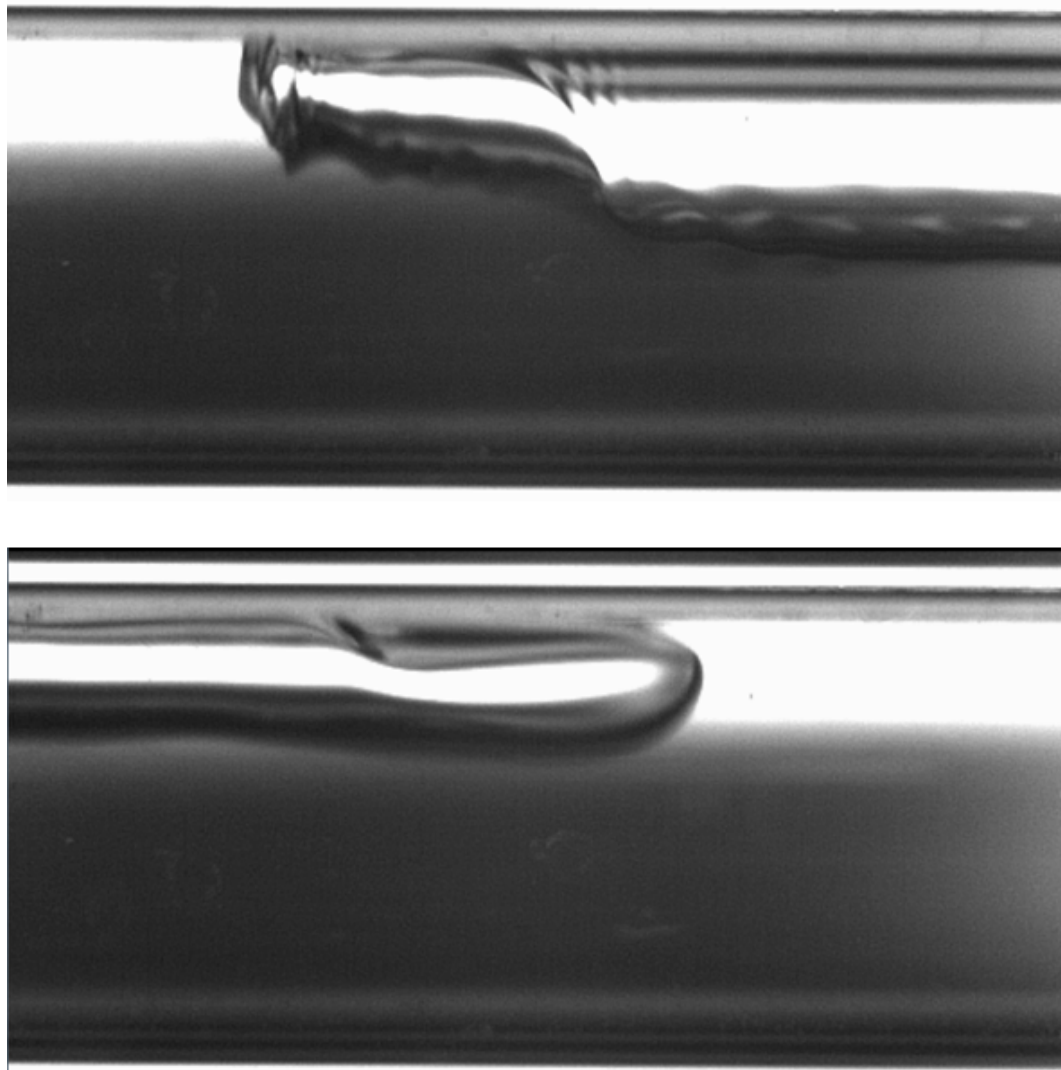


Figure 39: Still images from high-speed video of R134a with a bulk enthalpy of  $290 \text{ kJ kg}^{-1}$  ( $x=0.12$ )

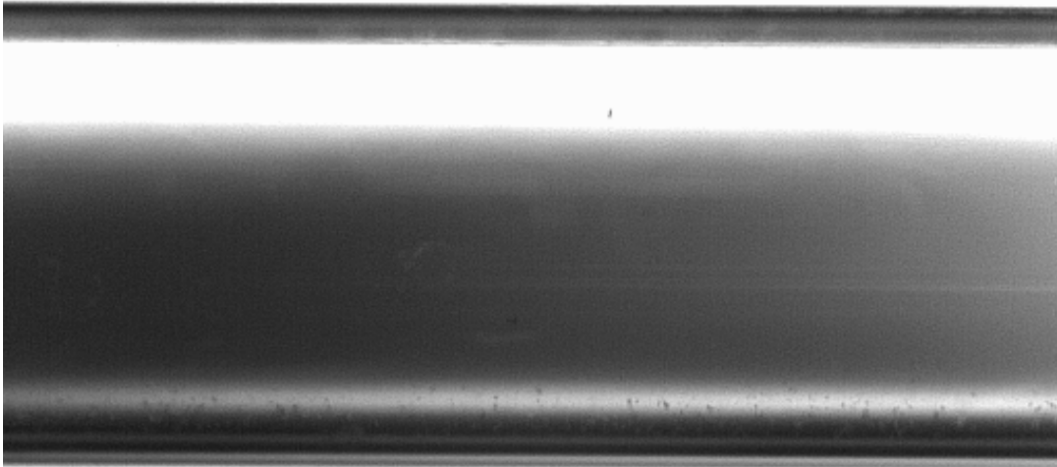


Figure 40: Still image from high-speed video of R134a with a bulk enthalpy of  $277 \text{ kJ kg}^{-1}$  ( $x=0.03$ )



Figure 41: Still image from high-speed video of R134a with a bulk enthalpy of  $262 \text{ kJ kg}^{-1}$

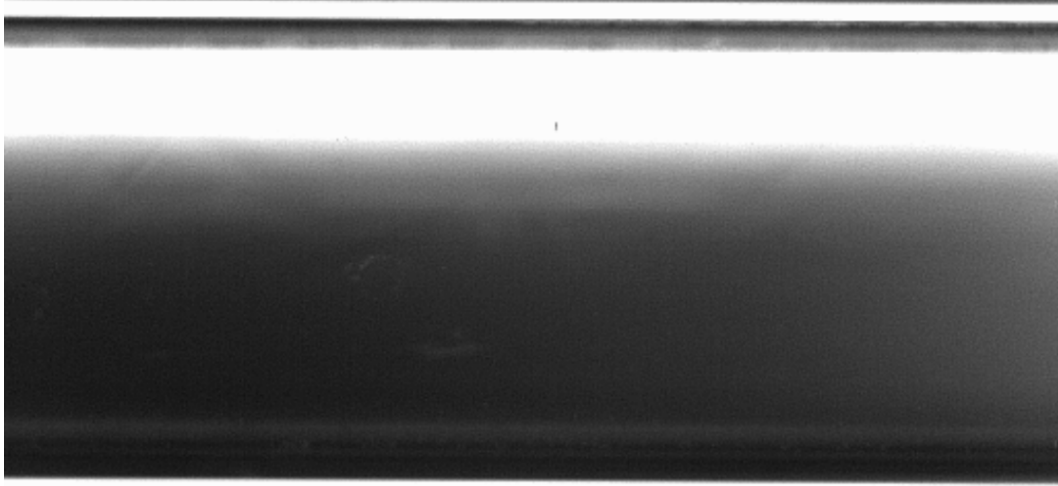


Figure 42: Still image from high-speed video of R134a with a bulk enthalpy of  $241 \text{ kJ kg}^{-1}$

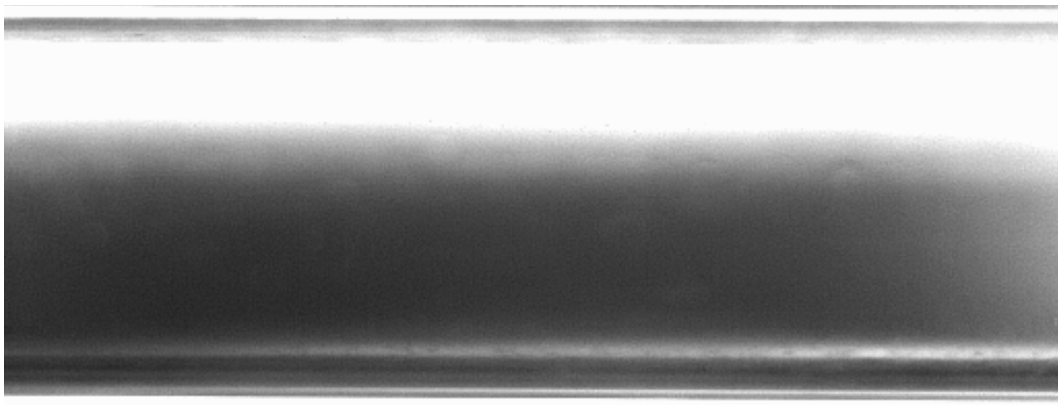


Figure 43: Still image from high-speed video of R134a with a bulk enthalpy of  $223 \text{ kJ kg}^{-1}$

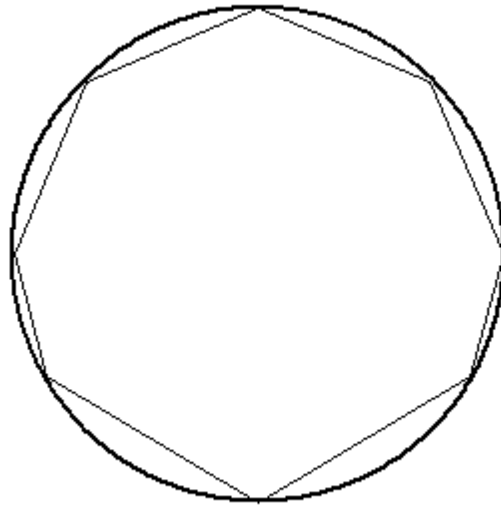


Figure 44: Cross-sectional view of measured film thicknesses for R134a at a bulk enthalpy of  $479 \text{ kJ kg}^{-1}$

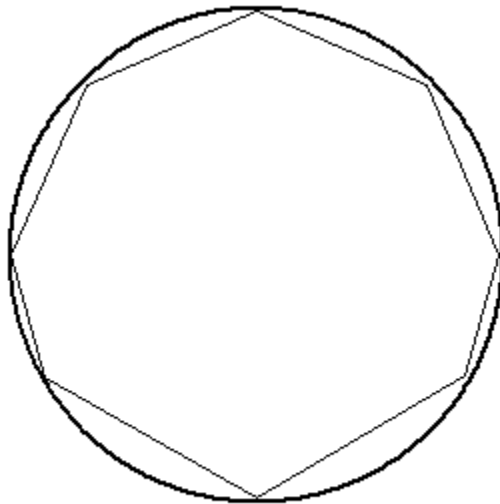


Figure 45: Cross-sectional view of measured film thicknesses for R134a at a bulk enthalpy of  $470 \text{ kJ kg}^{-1}$

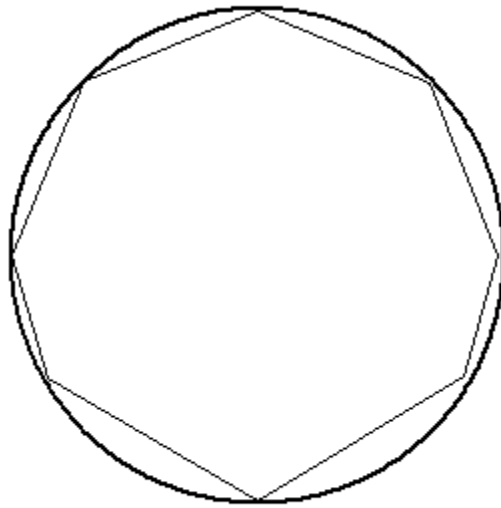


Figure 46: Cross-sectional view of measured film thicknesses for R134a at a bulk enthalpy of  $463 \text{ kJ kg}^{-1}$

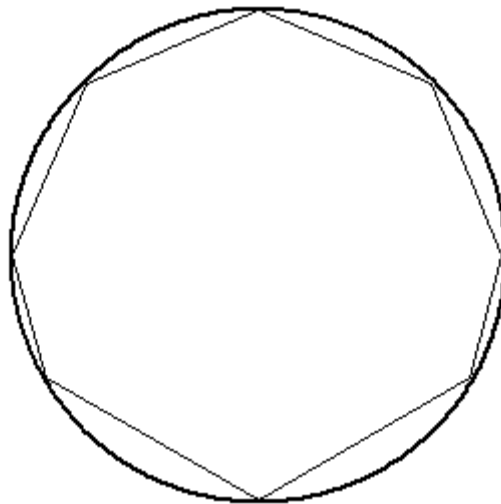


Figure 47: Cross-sectional view of measured film thicknesses for R134a at a bulk enthalpy of  $461 \text{ kJ kg}^{-1}$

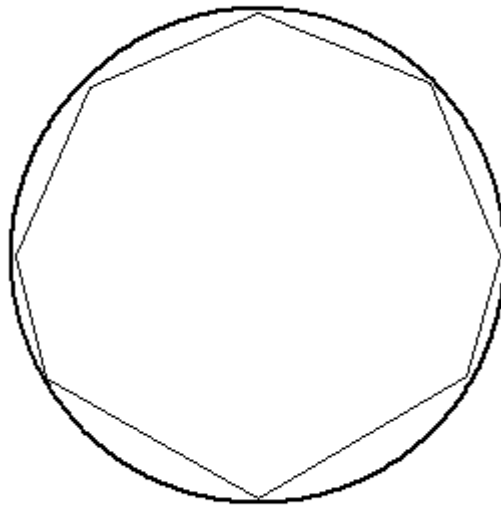


Figure 48: Cross-sectional view of measured film thicknesses for R134a at a bulk enthalpy of  $460 \text{ kJ kg}^{-1}$

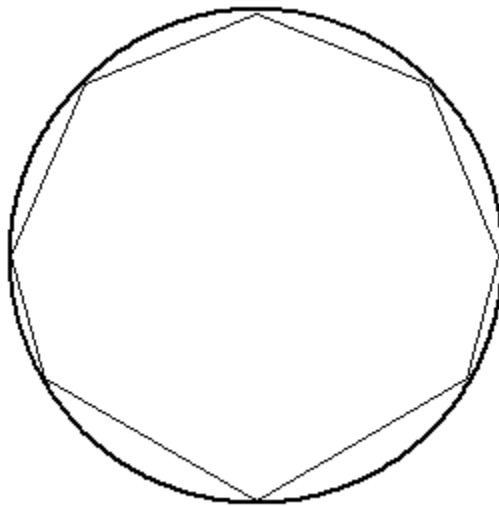


Figure 49: Cross-sectional view of measured film thicknesses for R134a at a bulk enthalpy of  $454 \text{ kJ kg}^{-1}$

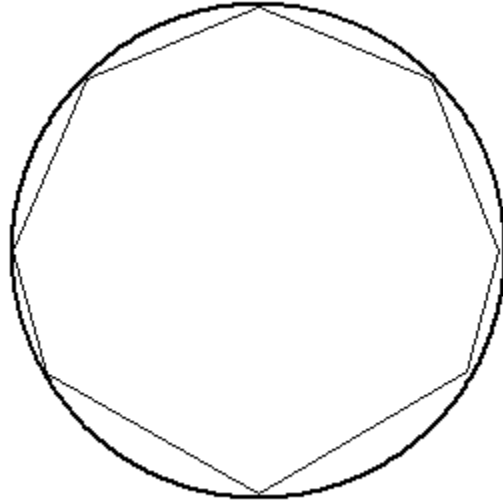


Figure 50: Cross-sectional view of measured film thicknesses for R134a at a bulk enthalpy of  $452 \text{ kJ kg}^{-1}$

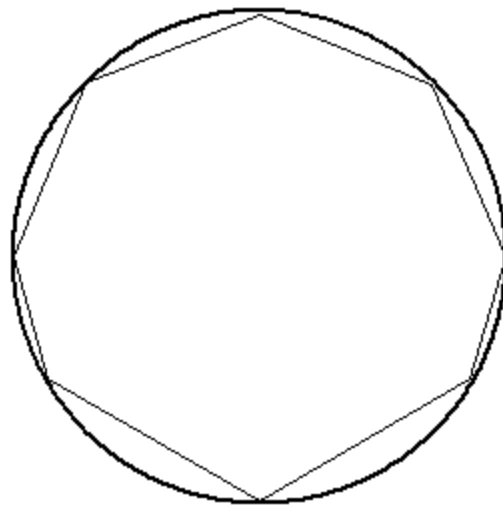


Figure 51: Cross-sectional view of measured film thicknesses for R134a at a bulk enthalpy of  $448 \text{ kJ kg}^{-1}$

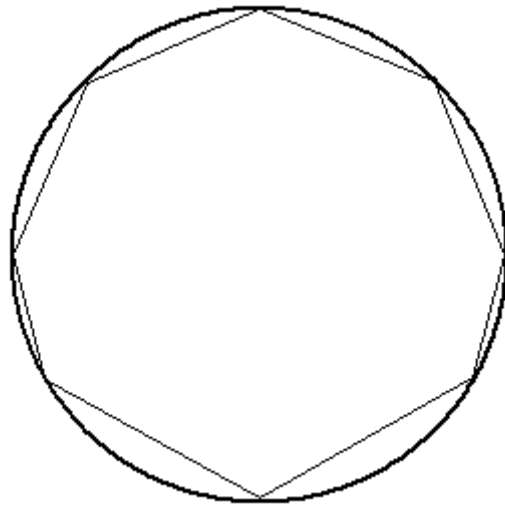


Figure 52: Cross-sectional view of measured film thicknesses for R134a at a bulk enthalpy of  $445 \text{ kJ kg}^{-1}$

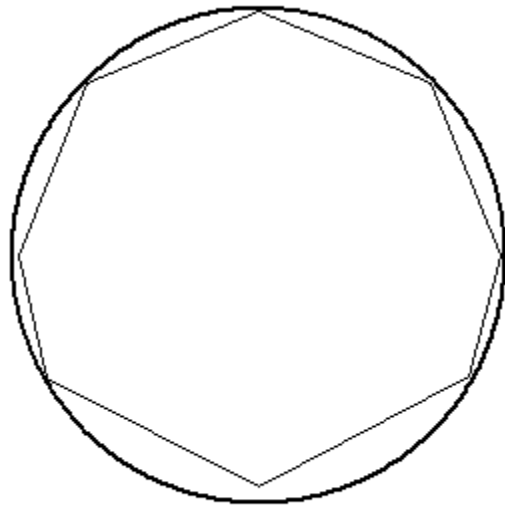


Figure 53: Cross-sectional view of measured film thicknesses for R134a at a bulk enthalpy of  $430 \text{ kJ kg}^{-1}$

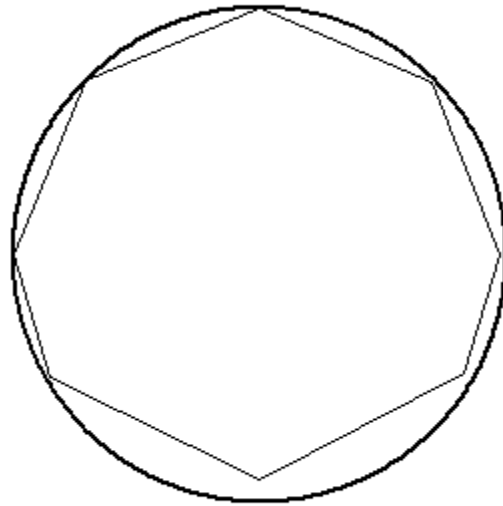


Figure 54: Cross-sectional view of measured film thicknesses for R134a at a bulk enthalpy of  $421 \text{ kJ kg}^{-1}$  ( $x=0.99$ )

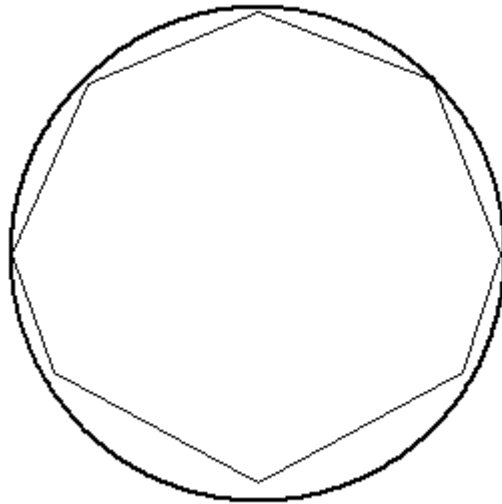


Figure 55: Cross-sectional view of measured film thicknesses for R134a at a bulk enthalpy of  $413 \text{ kJ kg}^{-1}$  ( $x=0.93$ )

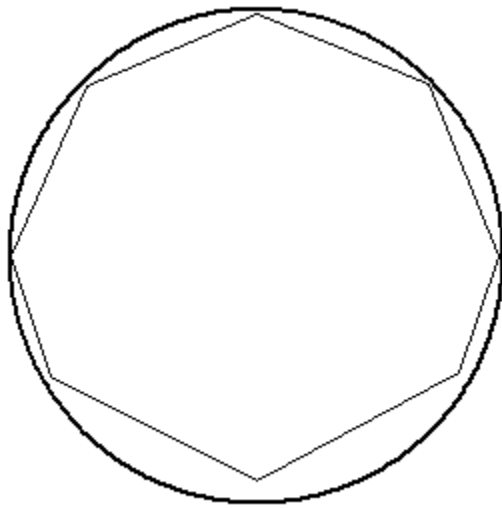


Figure 56: Cross-sectional view of measured film thicknesses for R134a at a bulk enthalpy of  $409 \text{ kJ kg}^{-1}$  ( $x=0.90$ )

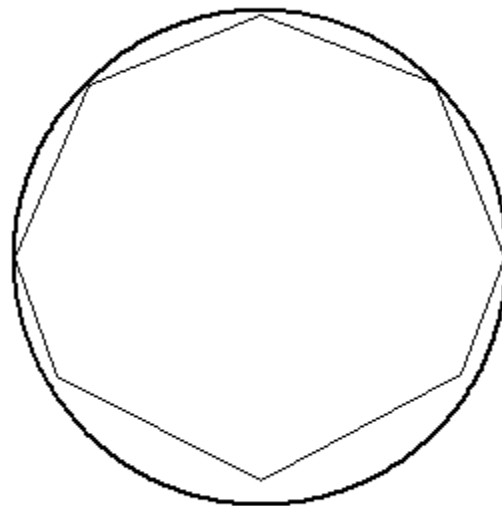


Figure 57: Cross-sectional view of measured film thicknesses for R134a at a bulk enthalpy of  $403 \text{ kJ kg}^{-1}$  ( $x=0.87$ )

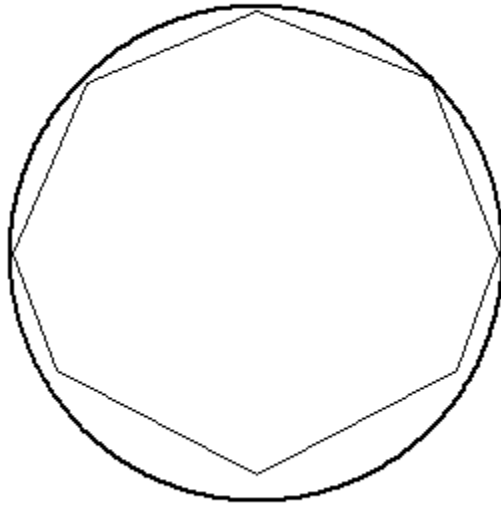


Figure 58: Cross-sectional view of measured film thicknesses for R134a at a bulk enthalpy of  $399 \text{ kJ kg}^{-1}$  ( $x=0.84$ )

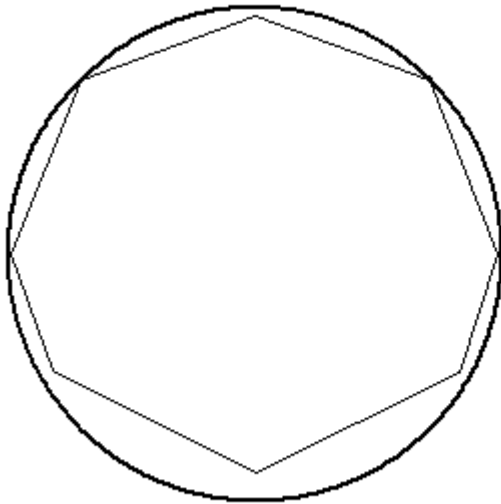


Figure 59: Cross-sectional view of measured film thicknesses for R134a at a bulk enthalpy of  $389 \text{ kJ kg}^{-1}$  ( $x=0.77$ )

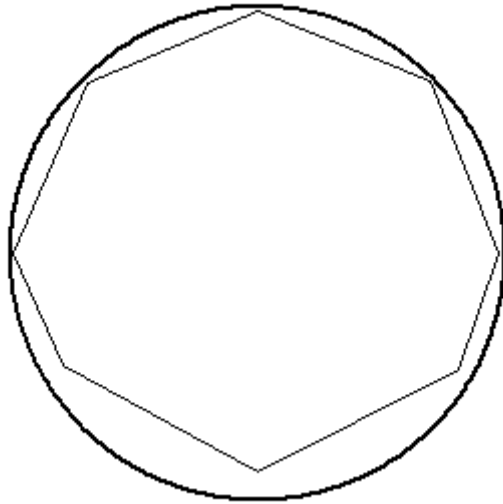


Figure 60: Cross-sectional view of measured film thicknesses for R134a at a bulk enthalpy of  $378 \text{ kJ kg}^{-1}$  ( $x=0.70$ )

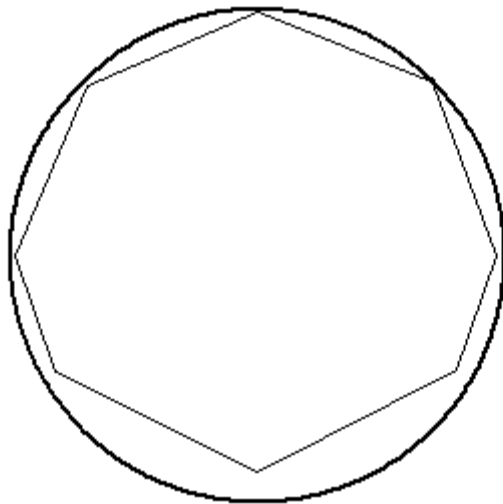


Figure 61: Cross-sectional view of measured film thicknesses for R134a at a bulk enthalpy of  $369 \text{ kJ kg}^{-1}$  ( $x=0.64$ )

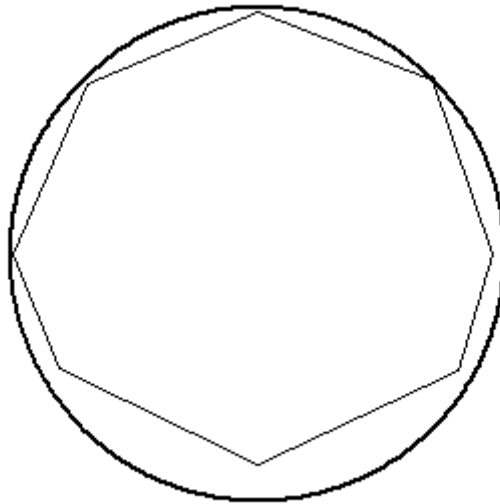


Figure 62: Cross-sectional view of measured film thicknesses for R134a at a bulk enthalpy of  $355 \text{ kJ kg}^{-1}$  ( $x=0.55$ )

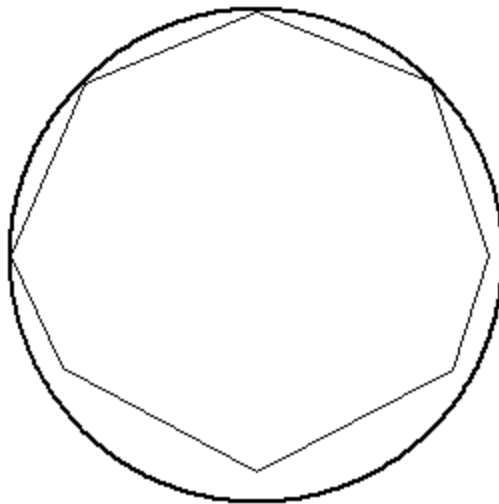


Figure 63: Cross-sectional view of measured film thicknesses for R134a at a bulk enthalpy of  $338 \text{ kJ kg}^{-1}$  ( $x=0.44$ )

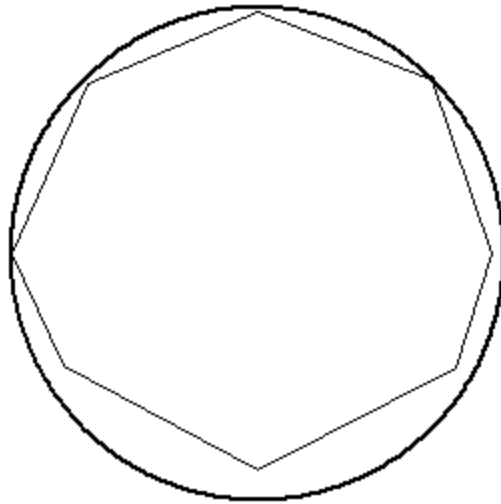


Figure 64: Cross-sectional view of measured film thicknesses for R134a at a bulk enthalpy of  $324 \text{ kJ kg}^{-1}$  ( $x=0.35$ )

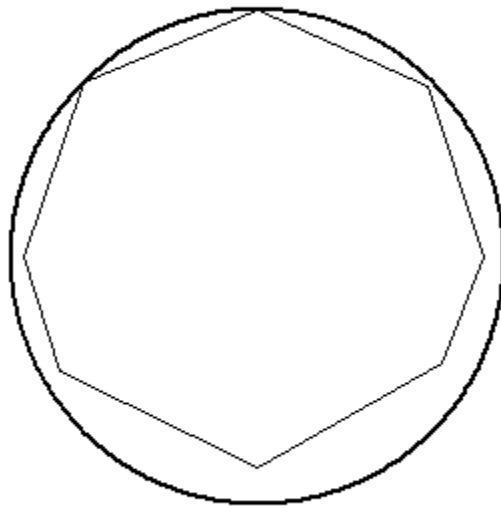


Figure 65: Cross-sectional view of measured film thicknesses for R134a at a bulk enthalpy of  $307 \text{ kJ kg}^{-1}$  ( $x=0.23$ )

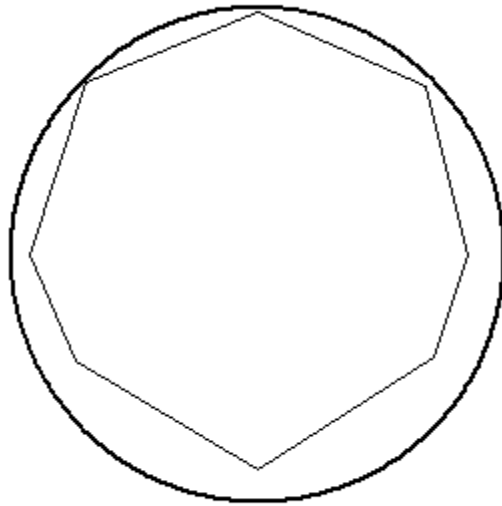


Figure 66: Cross-sectional view of measured film thicknesses for R134a at a bulk enthalpy of  $292 \text{ kJ kg}^{-1}$  ( $x=0.13$ )

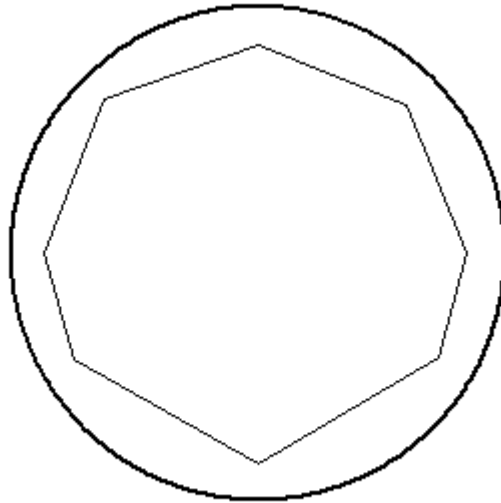


Figure 67: Cross-sectional view of measured film thicknesses for R134a at a bulk enthalpy of  $278 \text{ kJ kg}^{-1}$  ( $x=0.04$ )

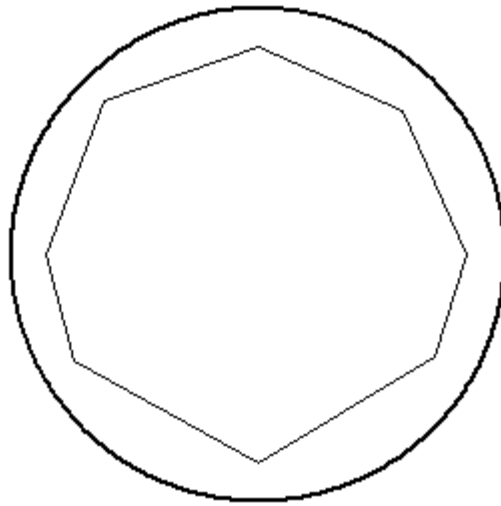


Figure 68: Cross-sectional view of measured film thicknesses for R134a at a bulk enthalpy of  $264 \text{ kJ kg}^{-1}$

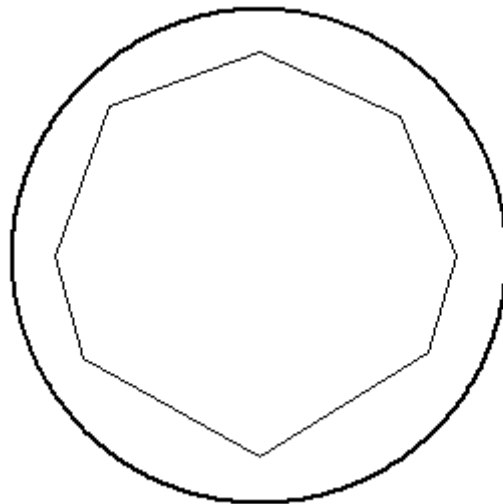


Figure 69: Cross-sectional view of measured film thicknesses for R134a at a bulk enthalpy of  $243 \text{ kJ kg}^{-1}$

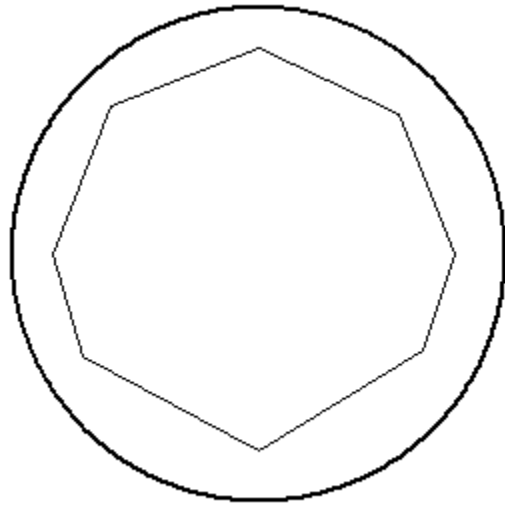


Figure 70: Cross-sectional view of measured film thicknesses for R134a at a bulk enthalpy of  $225 \text{ kJ kg}^{-1}$

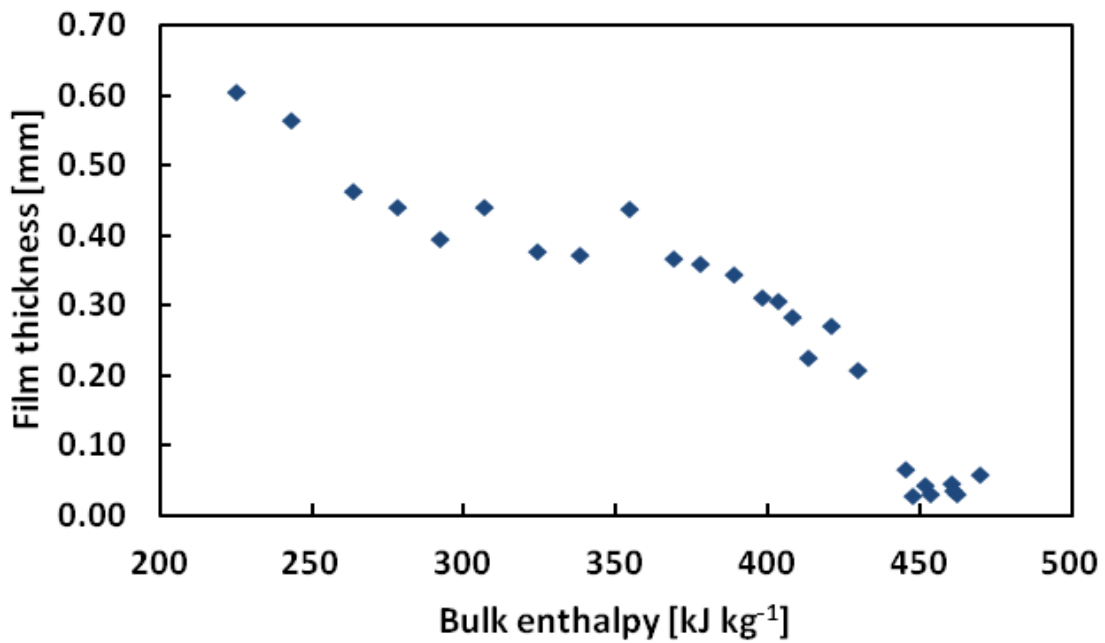


Figure 71: Measured film thicknesses for R134a at 1.319 MPa with a mass flux of  $100 \text{ kg m}^{-2} \text{ s}^{-1}$  at a position  $0^\circ$  clockwise from the bottom of the tube

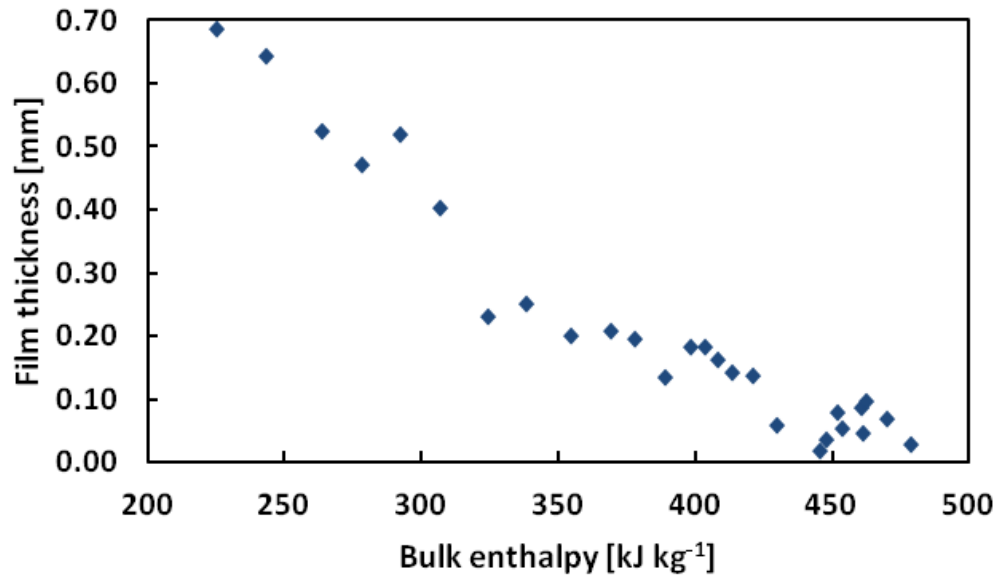


Figure 72: Measured film thicknesses for R134a at 1.319 MPa with a mass flux of  $100 \text{ kg m}^{-2} \text{ s}^{-1}$  at a position  $60^\circ$  clockwise from the bottom of the tube

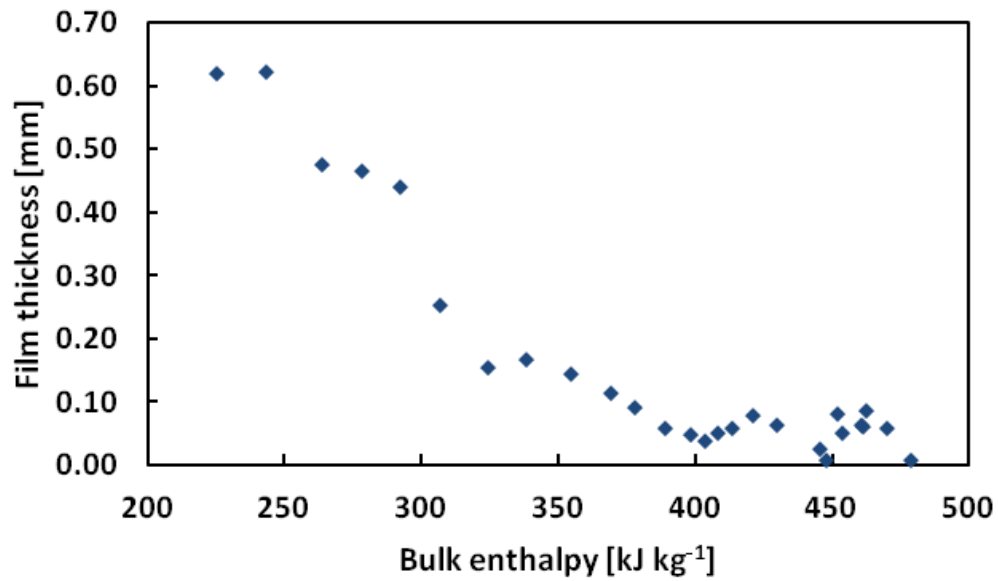


Figure 73: Measured film thicknesses for R134a at 1.319 MPa with a mass flux of  $100 \text{ kg m}^{-2} \text{ s}^{-1}$  at a position  $90^\circ$  clockwise from the bottom of the tube

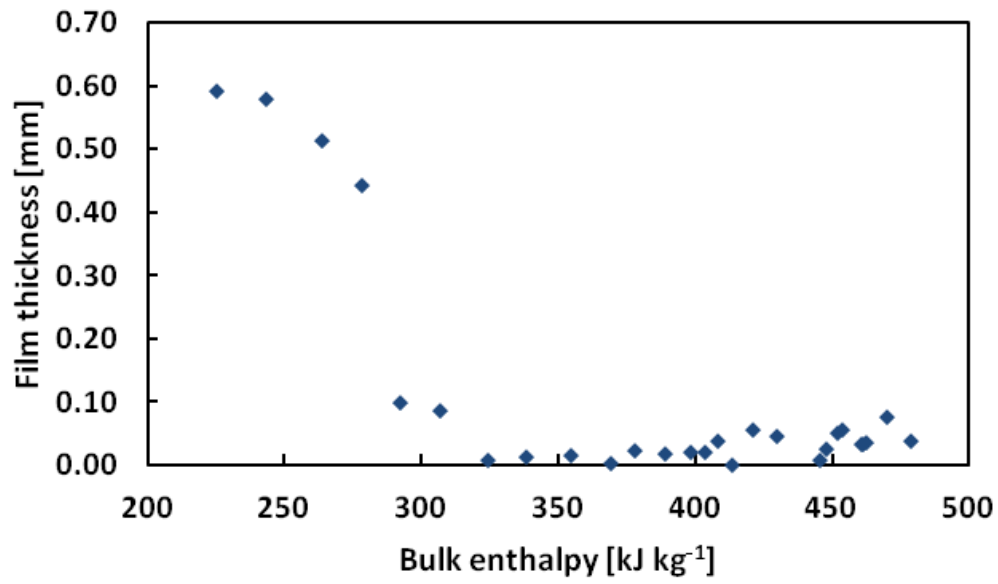


Figure 74: Measured film thicknesses for R134a at 1.319 MPa with a mass flux of  $100 \text{ kg m}^{-2} \text{ s}^{-1}$  at a position  $135^\circ$  clockwise from the bottom of the tube

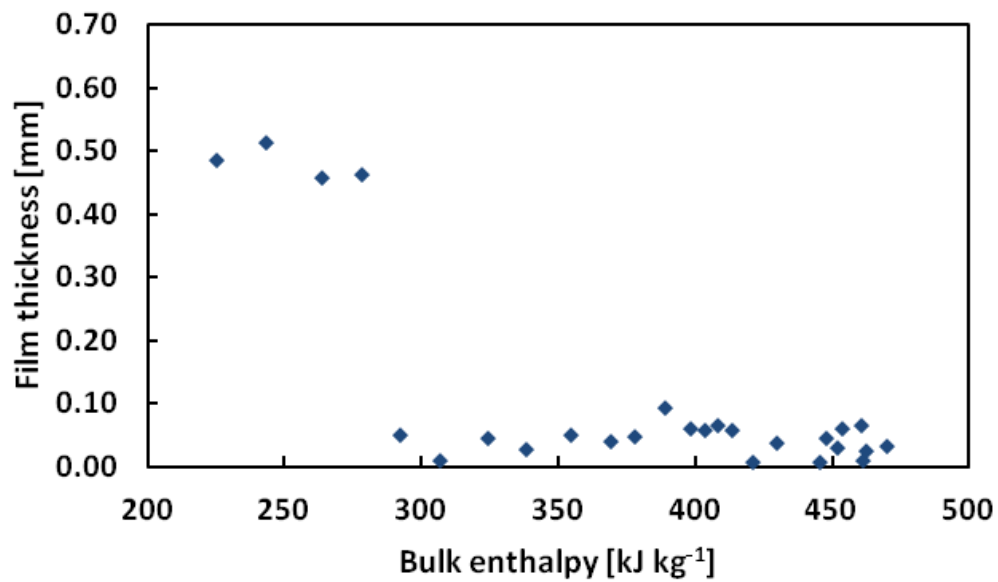


Figure 75: Measured film thicknesses for R134a at 1.319 MPa with a mass flux of  $100 \text{ kg m}^{-2} \text{ s}^{-1}$  at a position  $180^\circ$  clockwise from the bottom of the tube

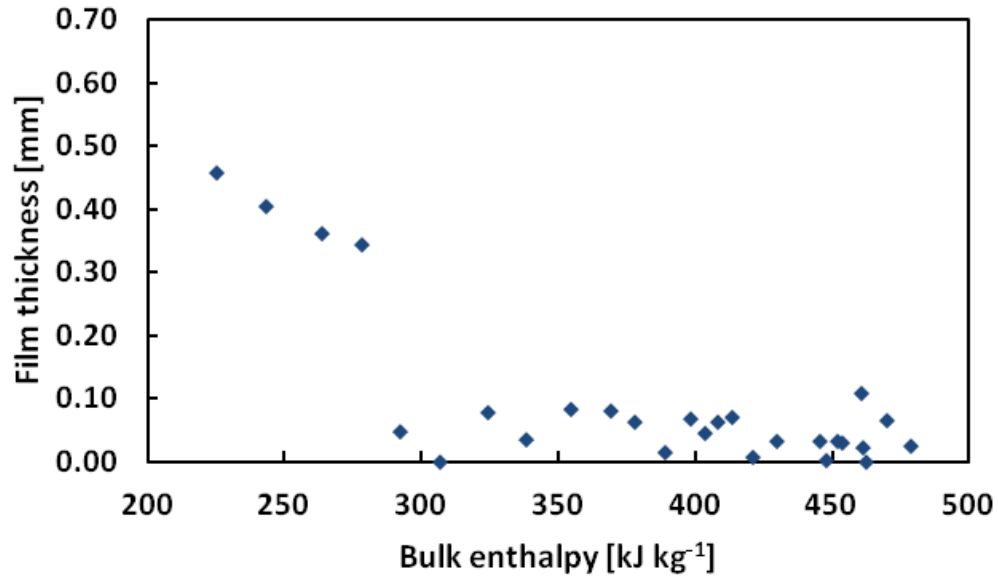


Figure 76: Measured film thicknesses for R134a at 1.319 MPa with a mass flux of  $100 \text{ kg m}^{-2} \text{ s}^{-1}$  at a position  $225^\circ$  clockwise from the bottom of the tube

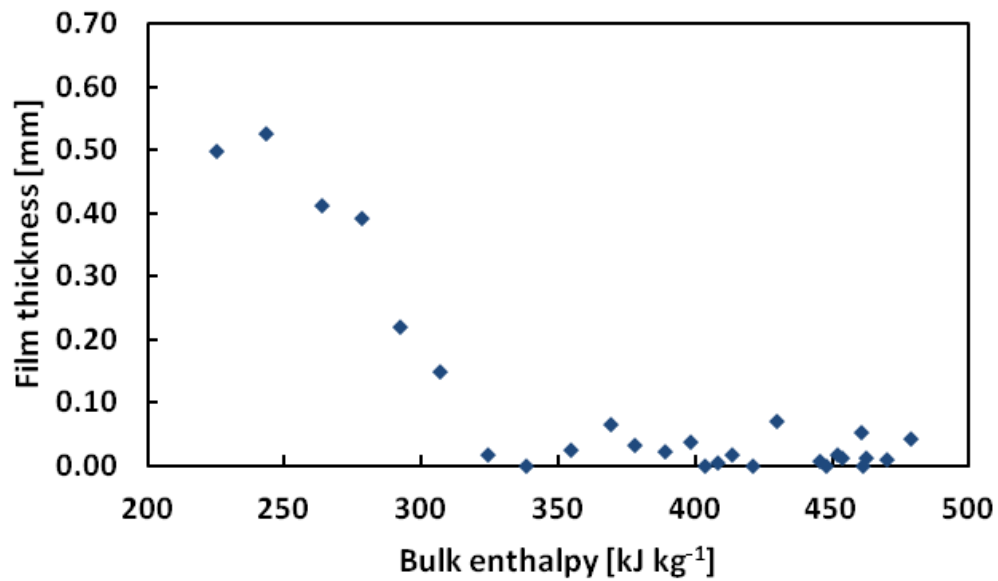


Figure 77: Measured film thicknesses for R134a at 1.319 MPa with a mass flux of  $100 \text{ kg m}^{-2} \text{ s}^{-1}$  at a position  $270^\circ$  clockwise from the bottom of the tube

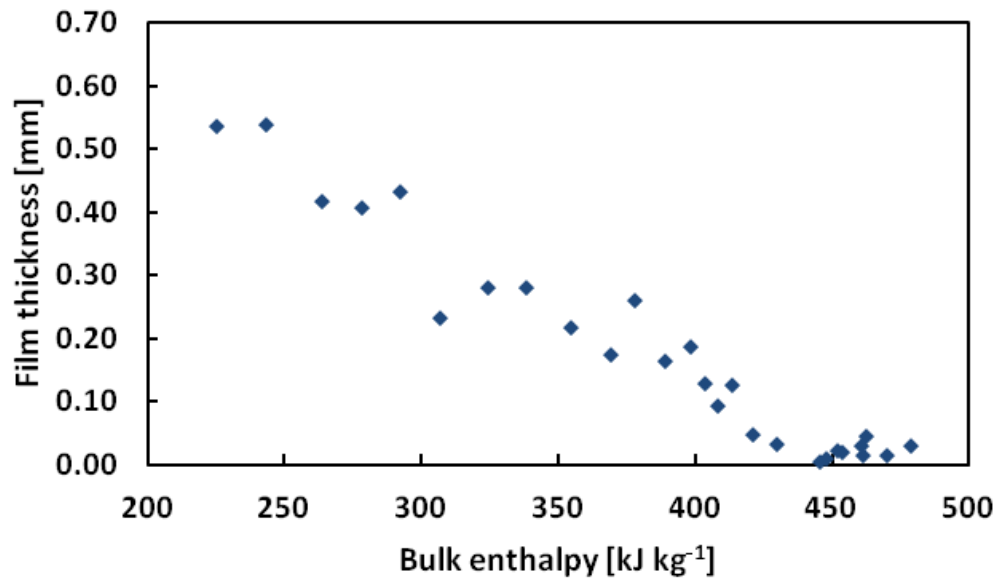


Figure 78: Measured film thicknesses for R134a at 1.319 MPa with a mass flux of  $100 \text{ kg m}^{-2} \text{ s}^{-1}$  at a position  $300^\circ$  clockwise from the bottom of the tube

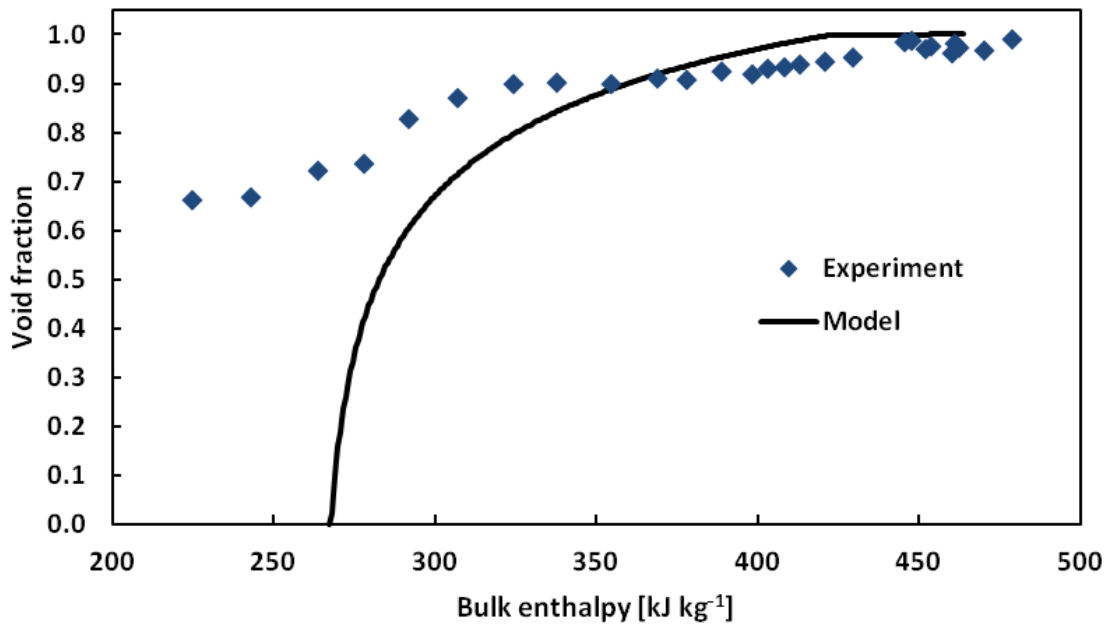
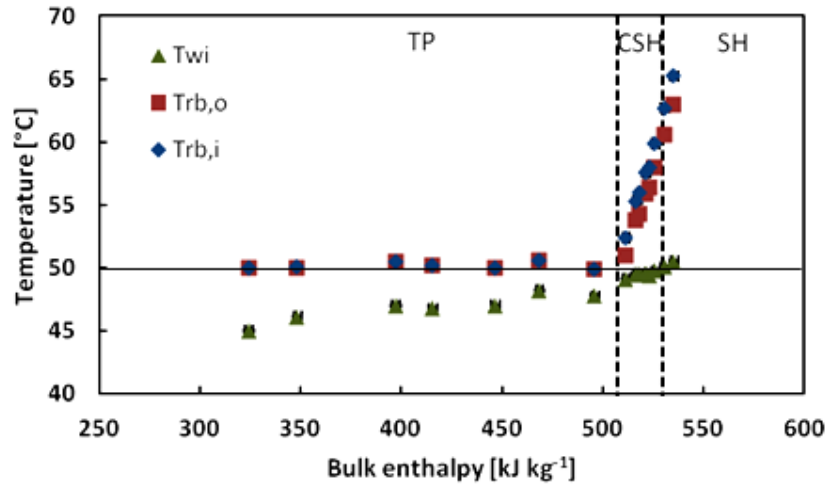
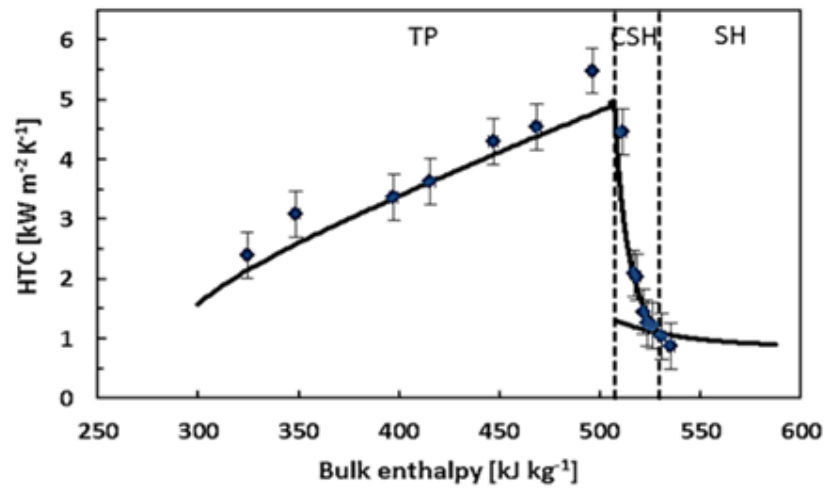


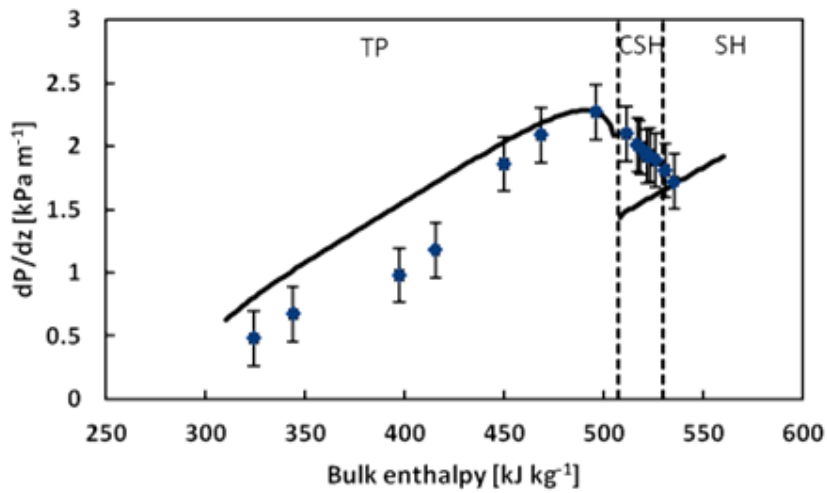
Figure 79: Comparison of void fraction calculated from measured film thicknesses and from five-zone model proposed by Agarwal and Hrnjak (2013)



(a)



(b)



(c)

Figure 80: Experimental test section refrigerant and wall temperatures, heat transfer coefficients, and pressure drop gradients for R32 at 3.141 MPa ( $T_{\text{sat}} = 50^\circ\text{C}$ ) and  $300 \text{ kg m}^{-2} \text{ s}^{-1}$

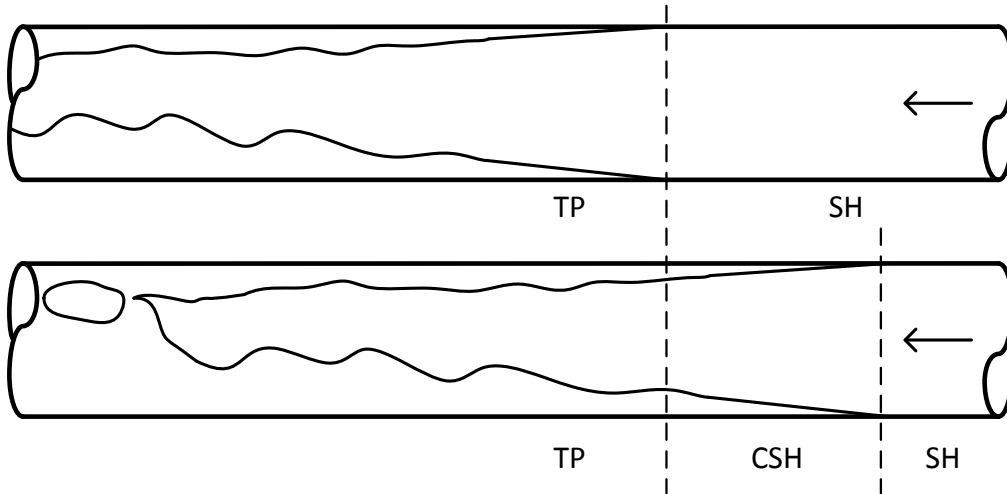


Figure 81: Simplified representations of how condensate is assumed to form with a conventional three-zone model (top) and a five-zone model including the condensing superheated zone (bottom)

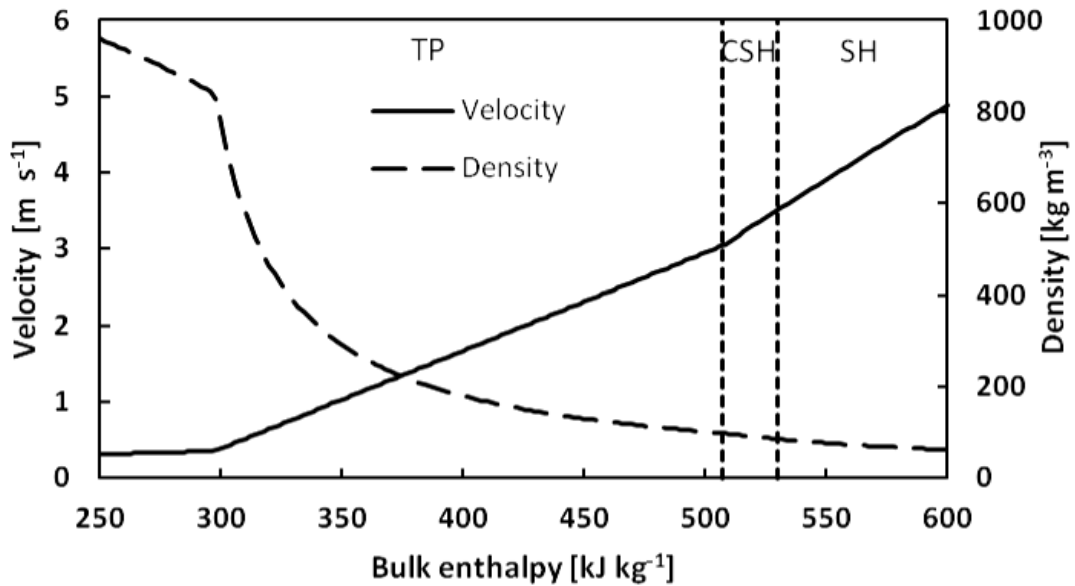


Figure 82: Homogeneous model predictions for refrigerant velocity and density for R32 at 3.141 MPa ( $T_{\text{sat}} = 50^{\circ}\text{C}$ ) and  $300 \text{ kg m}^{-2} \text{ s}^{-1}$

## CHAPTER 5: CONCLUSION

### 5.1 Summary

Experimental results verifying the existence of a condensing superheated zone have been presented for R134a in a horizontal smooth tube. The five-zone condensation model posits that condensation begins when the tube wall temperature falls below the saturation temperature, even in the presence of superheated vapor, and condensation continues in the presence of subcooled liquid even if the bulk enthalpy is lower than the saturated liquid point. These theories were confirmed visually, as high-speed videos of the condensing refrigerant revealed the presence of liquid at superheated bulk enthalpies and the presence of vapor at subcooled bulk enthalpies. The videos show that refrigerant at these conditions in a diabatic section begins to condense as droplets, rivulets, and a very thin film. As condensation continues, the flow regime changes to misty annular, wavy semi-annular, slug, plug, and bubbly flow. Film thickness measurements further support the trends seen in the videos. The liquid film begins to thicken at bulk enthalpies well above the saturated vapor enthalpy and is thicker on the lower surface of the tube than on the top and upper sides. Experimental heat transfer coefficients are consistent with the five-zone condensation model, increasing significantly in the condensing superheated region and transitioning smoothly between all 5 zones. The experimental HTC's were predicted within 40 percent by a 5-zone model proposed by Agarwal and Hrnjak (2013b).

Pressure drop in the CSH zone was examined as well. As the enthalpy decreases in the superheated region, the pressure drop also tends to decline as predicted by single-phase correlations. However, the experimental pressure drop, as shown for R32 in a horizontal smooth

tube, deviates from the single-phase correlation prior to the saturated vapor point. This deviation is due to the presence of condensate in the CSH zone that was confirmed by the visualization experiments. In the CSH region, the interaction of the condensate film with the vapor increases the pressure drop compared to what is expected for vapor alone. The pressure drop gradient then reaches a peak early in the two-phase region and decreases due to the tradeoff between increased shear interactions and a reduction in velocity.

## **5.2 Recommendations for future study**

Further study in this area is recommended in several different directions. The experimental results presented above could be applied more quantitatively to further their impact. The film thickness, by allowing the calculation of the liquid-vapor interface area and rate of change in the liquid mass, can be related directly to the proportions of latent and sensible heat transfer during condensation. Knowledge of these proportions is key to developing a physical model for the CSH zone. The comprehensive model of condensation can also be improved by applying the insight gained through the videos into the relevant flow regimes, particularly around the transition points between the single and two-phase regions. In addition to improving the heat transfer model, a model for pressure drop must be developed that properly accounts for the CSH zone. This effort may be aided by determining the liquid and mist velocities from the high-speed videos, as well as quantifying the waviness of the liquid, in order to gauge the shear and velocity-controlled effects on pressure drop.

The modeling work recommended above would also benefit from further experimental work. Accurate pressure drop measurements in the CSH region are needed for more fluids and

conditions. The film thickness measurements could be improved by reducing the uncertainty and possibly by taking measurements at more locations around the tube. The entire experimental scheme could be repeated for other refrigerants, pressures, heat fluxes and mass fluxes to verify the generality of the findings and to assess the effects of various parameters. Furthermore, the effect of oil or mixtures of refrigerants should be investigated to ensure that the research is applicable to a wide range of real systems.

## REFERENCES

- Agarwal, R., Hrnjak, P., 2013a, "Condensation in two phase and desuperheating zone for R1234ze(E), R134a and R32 in horizontal smooth tubes," *Int. J. Refrigeration*, in print.
- Agarwal, R., 2013b, Master's thesis, University of Illinois at Urbana-Champaign, Urbana, IL.
- Altman, M., Staub, F. W., and Norris, R. H., 1960, "Local Heat Transfer and Pressure Drop for Refrigerant-22 Condensing in Horizontal Tubes," *Chem. Eng. Progress Symp. Ser.*, vol. 56, no. 30, p. 151-159.
- ASME Performance Test Codes, 1985, Supplement on Instruments & Apparatus, P.1, *ANSI/ASME PTC: 19.1-1985*.
- Cavallini, A., Del Col, D., Doretti, L., Matkovic, M., Rossetto, L., Zilio, C., Censi, G., 2006, "Condensation in horizontal smooth tubes: a new heat transfer model for heat exchanger design," *Heat Tran. Eng.*, vol. 27, no. 8, p. 31-38.
- Colburn, A.P., 1933, "A method of correlating forced convection heat transfer data and comparison with fluid friction," *Trans. AIChE*, vol. 29, p. 174-210.
- Dobson, M.K., Chato, J.C., 1998, "Condensation in smooth horizontal tubes," *J. Heat Tran.*, vol. 120, p. 193-213.
- El Hajal, J., Thome, J.R., Cavallini, A., 2003, "Condensation in horizontal tubes, part 1: two-phase flow pattern map," *Int. J. Heat Mass Transfer*, vol. 46, no. 18, p. 3349-3363.
- Friedel, L., 1979, "Improved friction pressure drop correlations for horizontal and vertical two phase pipe flow," *Proc. European Two-Phase Flow Group Meeting*, Ispra, Italy, Paper no. E2.

- Fujii, T., Honda, H., Nozu, S., and Nakarai, S., 1978, "Condensation of Superheated Vapor Inside a Horizontal Tube," *Heat Transfer—Japanese Research*, vol. 4, no. 3, p. 1-48.
- Fukuta, M., Yanagisawa, T., Miyamura, S., Ogi, Y., 2004, "Concentration measurement of refrigerant/refrigeration oil mixture by refractive indices," *Int. J. Refrigeration*, vol. 27, no. 4, p. 346-352.
- Gnielinski, V., 1976, "New equation of heat and mass transfer in turbulent pipe and channel flow," *Int. Chem. Eng.*, vol. 16, p. 359-367.
- Hurlburt, E. T., Newell, T. A., 1996, "Optical measurement of liquid film thickness and wave velocity in liquid film flows," *Experiments in Fluids*, vol. 21, p. 357-362.
- Kattan, N., Thome, J.R., Favrat, D., 1998, "Flow boiling in horizontal tubes: part I- development of a diabatic two phase flow pattern map," *J. Heat Transfer* vol. 120, p. 140-147.
- Kondou, C., Hrnjak, P., 2011a, "Heat rejection from R744 flow under uniform temperature cooling in a horizontal smooth tube around the critical point," *Int. J. Refrigeration*, vol. 34, no. 3, p. 719-731.
- Kondou, C., Hrnjak, P., 2011b, "Heat rejection in condensers close to critical point-desuperheating, condensation in superheated region and condensation of two phase fluid," *Int. Conf. Heat Trans. Fluid Mech. and Thermodynamics*, Mauritius.
- Kondou, C., Hrnjak, P., 2012, "Condensation from superheated vapor flow of R744 and R410A at subcritical pressures in a horizontal smooth tube," *Int. J. Heat Mass Transfer*, vol. 55, p. 2779-2791.
- Kondou, C., 2012, "De-superheating and condensation from R744 and R410A in smooth and microfin tubes near critical point (final report)," ACRC, UIUC, Project 264.

- Lee, C. C, Teng, Y. J., and Lu, D. C , 1991, "An Investigation of Condensation Heat Transfer of Superheated R-22 Vapor in a Horizontal Tube," *Proc. World Conf. on Experimental Heat Transfer, Fluid Mechanics, and Thermodynamics*, p. 1051-1057.
- Lemmon, E.W., Huber, M.L., McLinden, M.O., 2007, Reference Fluid Thermodynamic and Transport Properties-REFPROP Ver.8.0, National Institute of Standards and Technology, Boulder, CO, USA.
- Miropolsky, Z. L., Shneersva, R. I., Teernakova, L. M., 1974, "Heat Transfer at Superheated Steam Condensation Inside Tubes," *Proc. 5th Int. Heat Transfer Conference*, vol. 3, p. 246-249.
- Moffat, R.J., 1988, "Describing the uncertainties in experimental results," *Exp. Therm. Fluid Sci.*, vol. 1, p. 3-17.
- Shedd, T. A., Newell, T. A., 1998, "Automated optical liquid film thickness measurement method," *Review of Scientific Instruments*, vol. 69, no. 12, p. 4205-4213.
- Smith S.L., 1969, "Void fractions in two-phase flow: a correlation based upon an equal velocity head model," *Proc. Instn. Mech Engrs.*, vol. 184, no. 36, p. 647-664.
- Webb, R.L., 1998, "Convective Condensation of Superheated Vapor," *J. Heat Transfer*, vol. 120, p. 418-421.
- Wujek, S., 2011, Doctoral dissertation, University of Illinois at Urbana-Champaign, Urbana, IL.

## **APPENDIX A: REPEATABILITY TEST AND PRESSURE DROP SENSITIVITY ANALYSIS**

Figure 83 displays the repeatability of the heat transfer coefficient results. The HTC's determined from the recent experiments including visualization show satisfactory agreement with the results of experiments previously performed by Agarwal and Hrnjak (2013). Figure 84 illustrates the results of an analysis of the sensitivity of the HTC to the pressure drop values used in the data reduction. In the figure legend, dP high corresponds to a maximum pressure drop across the test section but no pressure drop across the precooler. dP low corresponds to zero pressure drop across the test section and the precooler. dP mid corresponds to a maximum total pressure drop distributed equally across the test section and precooler. The maximum total pressure drop reading was chosen as (2.0-0.967) mV because 0.967 mV was the consistent reading for the pressure drop in just the line to the differential pressure transducer, and 2.0 mV is 15% higher than the highest pressure drop reading recorded for these experimental conditions.

## A.1 Figures

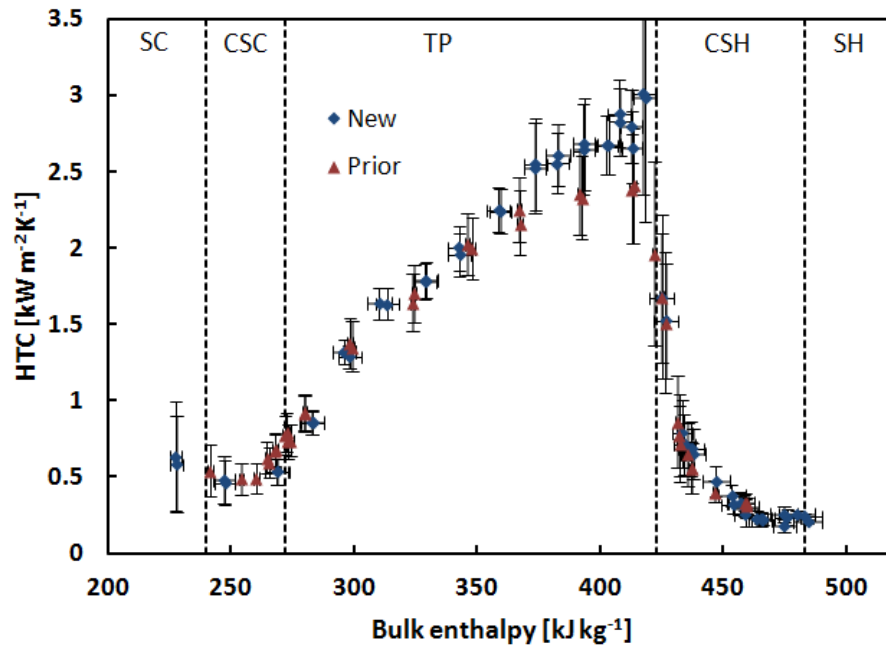


Figure 83: Comparison of experimental heat transfer results of this work with results presented by Agarwal and Hrnjak (2013), both for R134a at 1.319 MPa with a mass flux of  $100 \text{ kg m}^{-2} \text{ s}^{-1}$  and a heat flux of  $10 \text{ kW m}^{-2}$

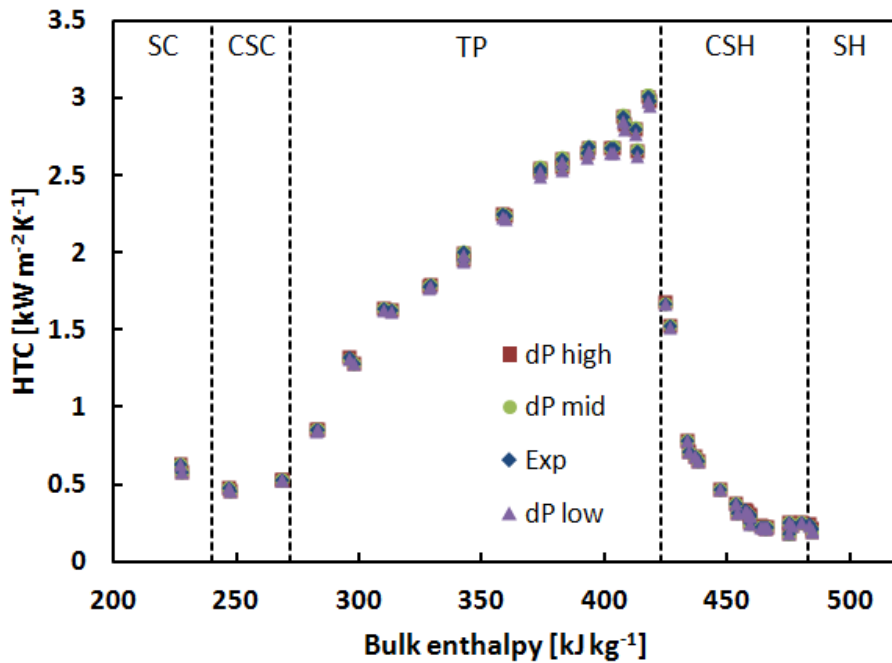
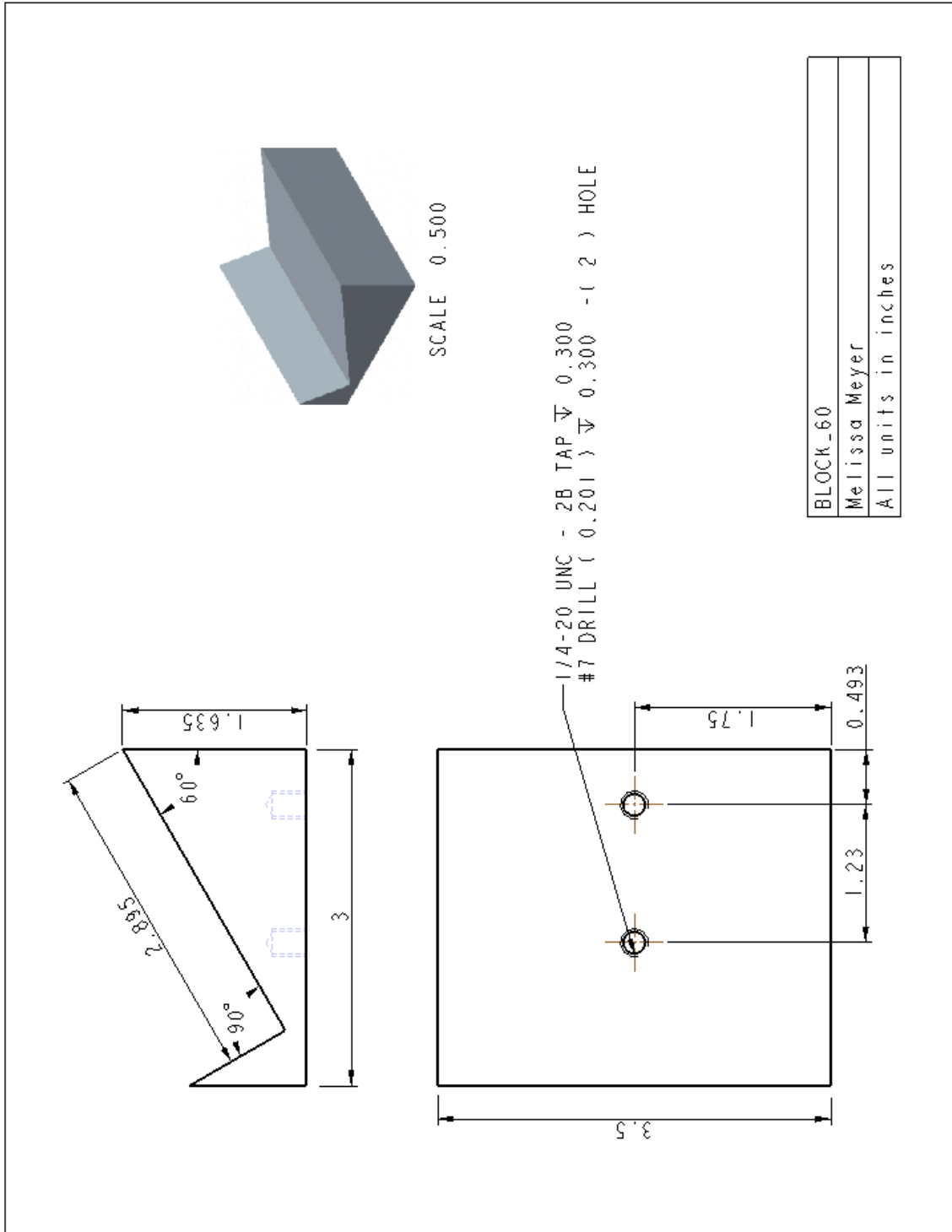
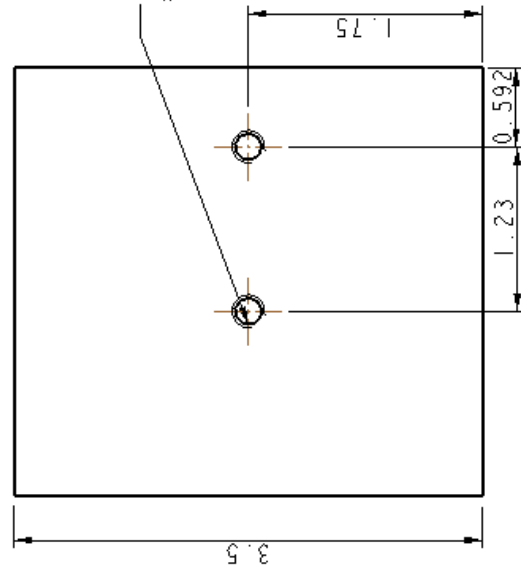
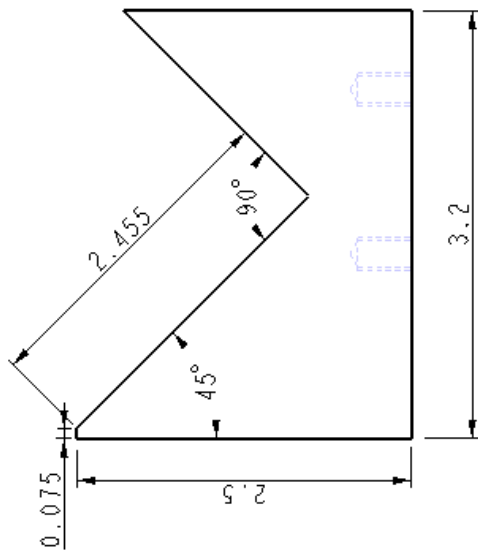


Figure 84: Effect of different pressure drop values on heat transfer coefficients for R134a at 1.319 MPa with a mass flux of  $100 \text{ kg m}^{-2} \text{ s}^{-1}$  and a heat flux of  $10 \text{ kW m}^{-2}$

## APPENDIX B: CAD DRAWINGS

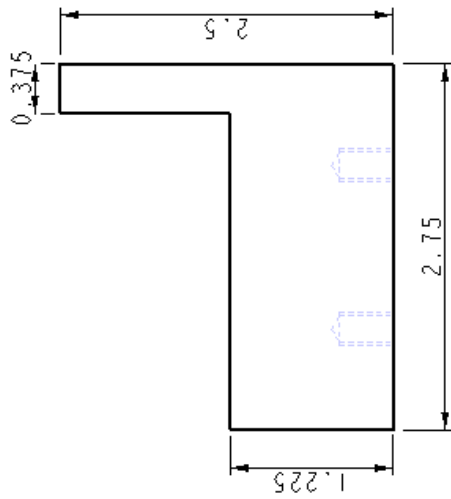
### B.1 Film thickness measurement support blocks





SCALE 0.500

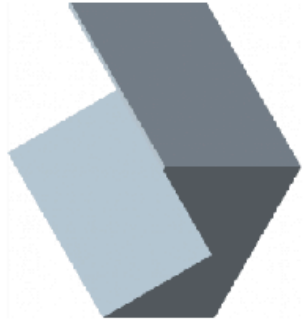
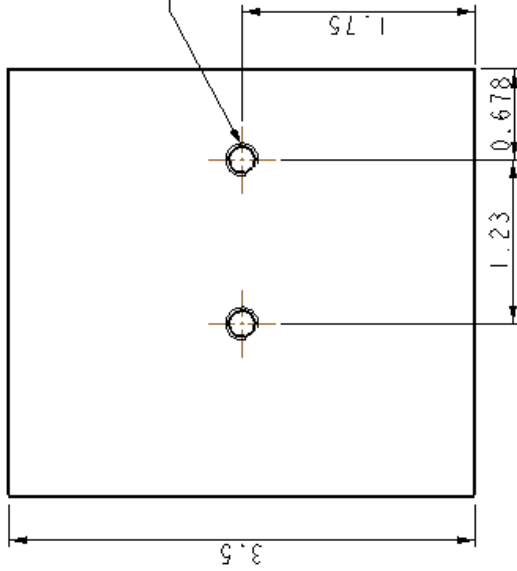
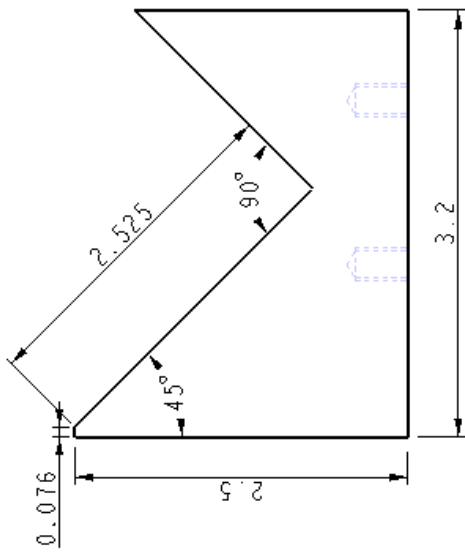
BLOCK_135
Melissa Meyer
All units in inches



SCALE 0.500



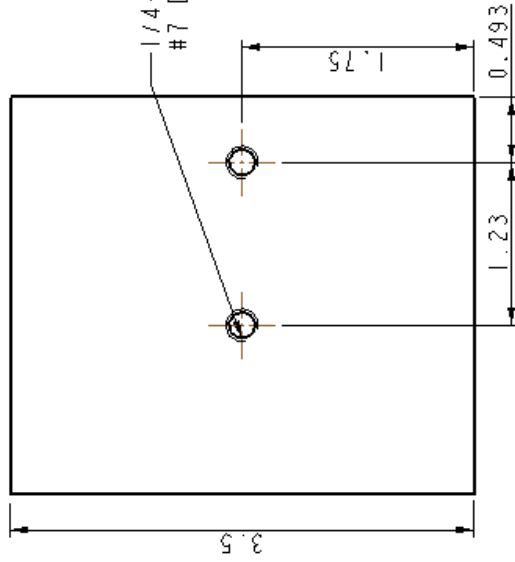
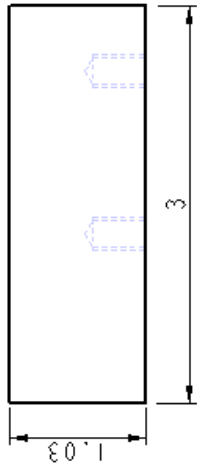
BLOCK_180
Melissa Meyer
All units in inches



SCALE 0.500

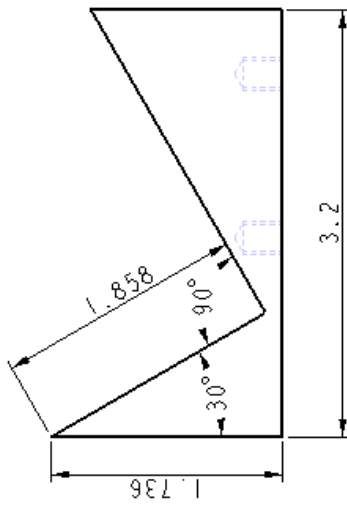
1/4-20 UNC - 2B TAP  $\nabla$  0.400  
 #7 DRILL ( 0.201 )  $\nabla$  0.400 - ( 2 ) HOLE

BLOCK_225
Melissa Meyer
All units in inches



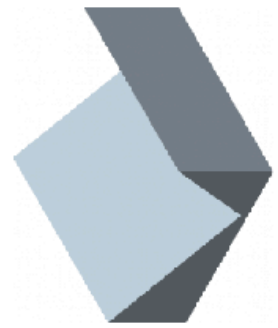
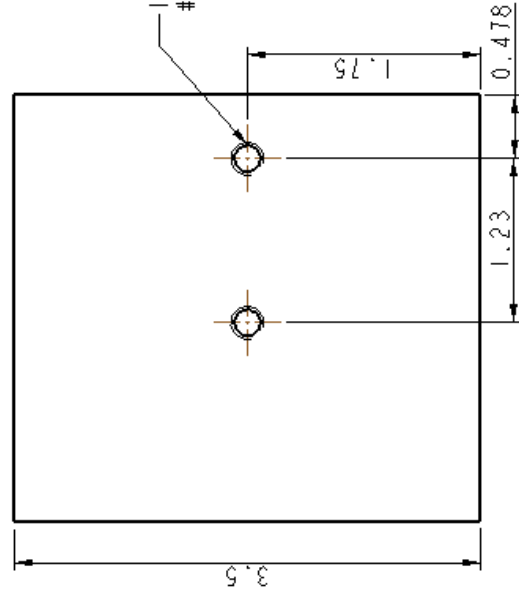
SCALE 0.500

BLOCK_270
Melissa Meyer
All units in inches

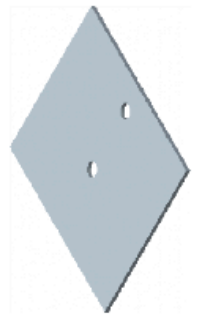
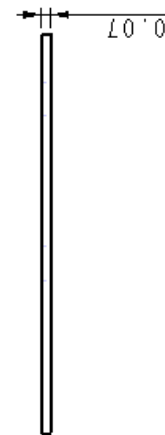
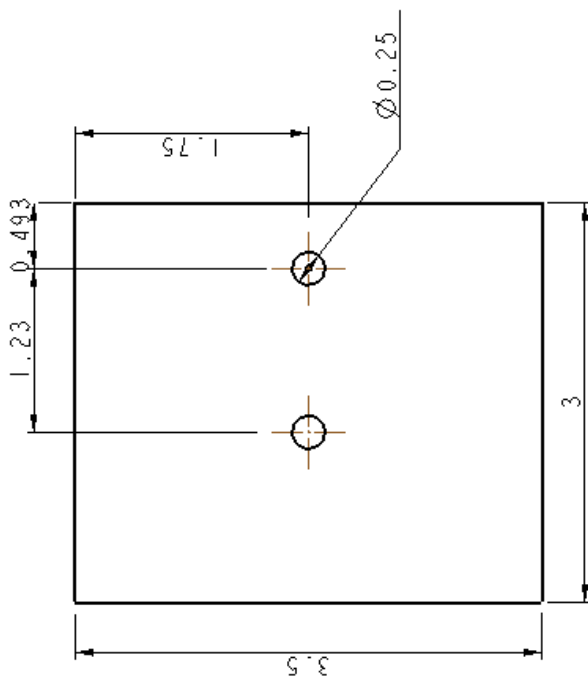


1/4-20 UNC - 2B TAP  $\nabla$  0.300  
#7 DRILL ( 0.201 )  $\nabla$  0.300 - ( 2 ) HOLE

SCALE 0.500



BLOCK_300
Melissd Meyer
All units in inches



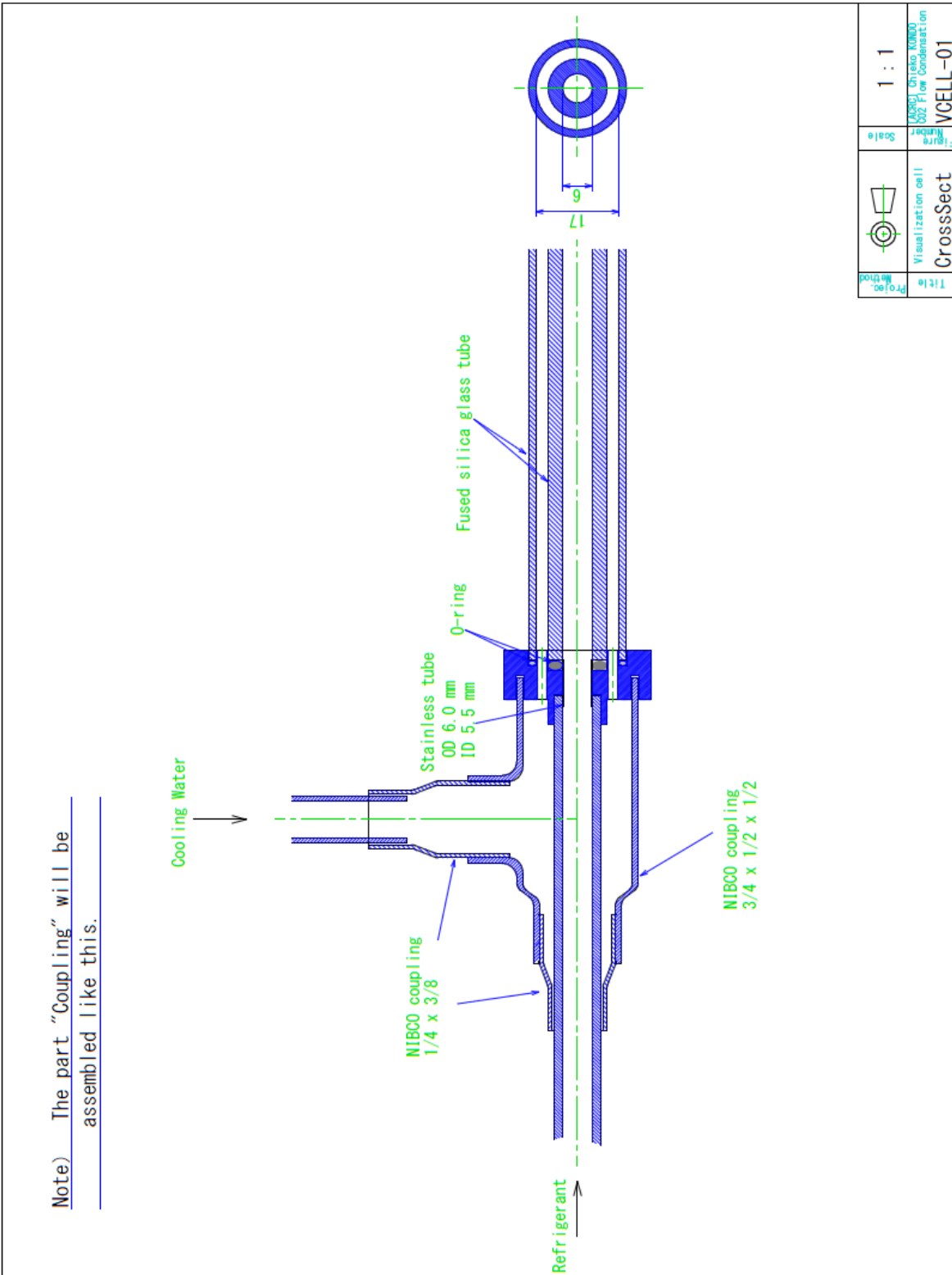
SCALE 0.500

BLOCK\_INSERT\_07

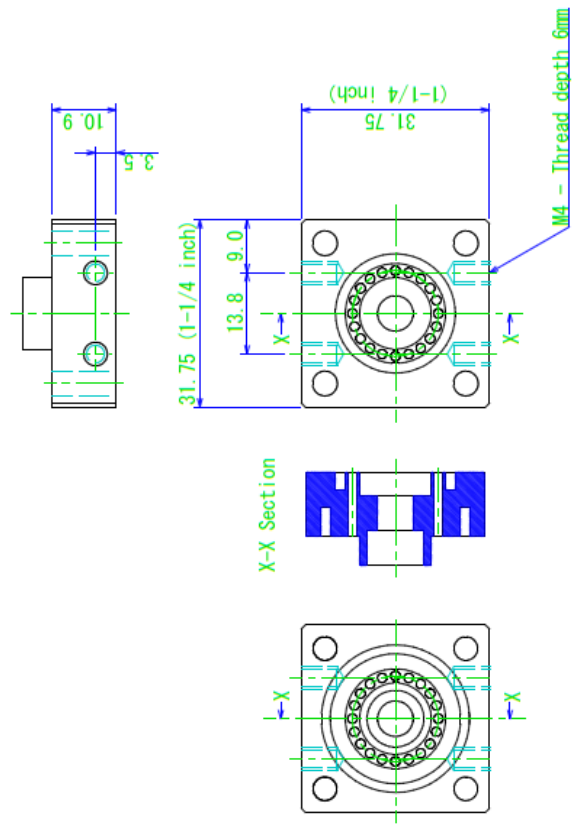
Melissa Meyer

All units in inches

## B.2 Visualization section components (courtesy of C. Kondou)



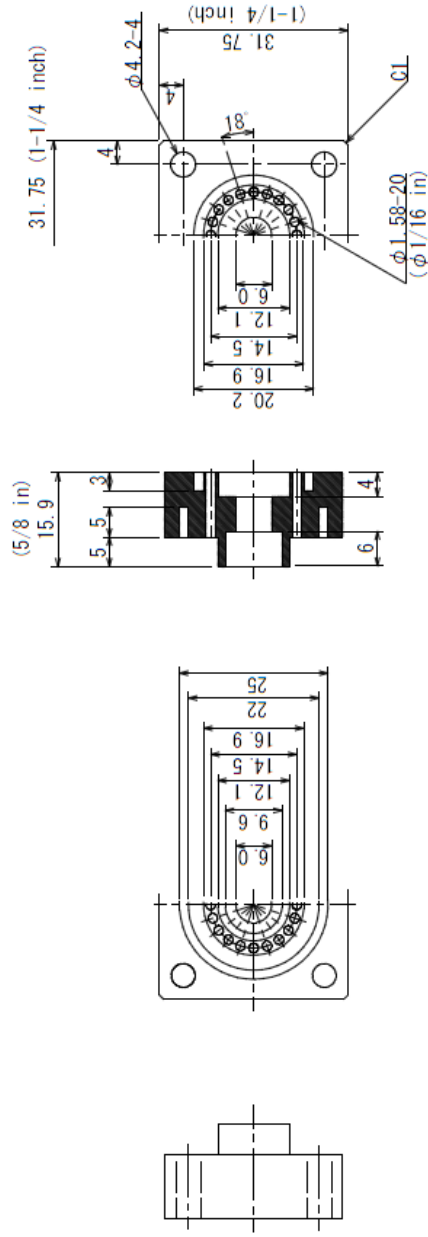
Note) Please thread at four places.  
Size of threads: M4-female. Thread depth 6mm  
Four couplings are provided.



Unit [mm]

Proj Method	Scale	1 : 1
Visualization cell	Scale	1 : 1
Coupling#2	Scale	1 : 1
Title	Scale	1 : 1
COND-VCCELL		

**Note)** Please make 4 parts of Coupling.  
 Provided material is machinable Brass (Alloy 360)  
 5/8" Thick, 1-1/4" Width, 1" Length.



Unit [mm]

Figure Number	Scale	1 : 1
Method	Visualization cell	
	Coupling	
		COND-VCELL

**APPENDIX C: UNCERTAINTY ANALYSIS**  
(Kondou, ACRC 2012)

When an experimental result  $R$  has a symmetric uncertainty, the range of 95% coverage can be written:

$$R = \hat{R} \text{ (center of experimental value or reading value)} \pm U_R \text{ (uncertainty)} \quad (C.1)$$

$$U_R = \left[ (B_R)^2 + (tS_R)^2 \right]^{1/2}$$

where,  $B$ ,  $S$ , and  $t$  are the degree of accuracy, accuracy degree of average value, symmetric student factor of 95%. In following uncertainty analysis, it is assumed that the effect of human error  $tS$  is negligible. Hence, the uncertainty of the measurement value  $R$  having measurement parameters  $X_1 \sim X_i$  is determined as,

$$U_R \approx B_R = \left[ \sum_{i=1}^N \left( \frac{\partial R}{\partial X_i} U_{X_i} \right)^2 \right]^{1/2} \quad (C.2)$$

$$R = f(X_1, X_2, \dots, X_i, \dots, X_N) \quad (C.3)$$

Followings are the procedure of uncertainty analysis for main measurement results of this study.

**Pressure drop gradient  $\Delta P/\Delta Z$**

The uncertainty of pressure drop gradient at the test section is,

$$U_{\Delta P/\Delta Z}^2 = \left[ \frac{\partial(\Delta P/\Delta Z)}{\partial \Delta P_{TS}} U_{\Delta P_{TS}} \right]^2 + \left[ \frac{\partial(\Delta P/\Delta Z)}{\partial \Delta Z_{\Delta P/\Delta Z}} U_{\Delta Z_{\Delta P/\Delta Z}} \right]^2 \quad (C.4)$$

$$= U_{\Delta P_{TS}}^2 + \left[ \frac{-1}{\Delta Z_{\Delta P/\Delta Z}^2} U_{\Delta Z_{\Delta P/\Delta Z}} \right]^2 = U_{\Delta P_{TS}}^2 + \frac{1}{\Delta Z_{\Delta P/\Delta Z}^4} U_{\Delta Z_{\Delta P/\Delta Z}}^2$$

Here,

$$U_{\Delta P_{TS}} = 0.257[\text{kPa}]$$

$$\Delta Z_{\Delta P/\Delta Z} = 0.288[\text{m}]$$

$$U_{\Delta Z_{\Delta P/\Delta Z}} = \Delta Z_{\Delta P/\Delta Z} \times 5\% = 0.0144[\text{m}]$$

This  $\Delta Z_{\Delta P/\Delta Z}$  is the length between pressure taps.

**Inlet pressure of test section  $P_{TSi}$**

The inlet pressure of test section is obtained with measured pressure of mixing chamber  $P_{MC}$  and differential pressure through the pre-cooler  $\Delta P_{PC}$ .

$$P_{\text{TSi}} = P_{\text{MC}} - \Delta P_{\text{PC}} \quad (\text{C.5})$$

Hence, the uncertainty is determined as bellow.

$$U_{P_{\text{TSi}}}^2 = U_{P_{\text{MC}}}^2 + U_{\Delta P_{\text{PC}}}^2 \approx U_{P_{\text{MC}}}^2 \quad (\text{C.6})$$

$$\because U_{P_{\text{MC}}} \gg U_{\Delta P_{\text{PC}}}$$

### Outlet pressure of test section $P_{\text{TSo}}$

Similarly, the outlet pressure of test section and its uncertainty are,

$$P_{\text{TSo}} = P_{\text{MC}} - \Delta P_{\text{PC}} - \Delta P_{\text{TS}} \quad (\text{C.7})$$

$$U_{P_{\text{TSi}}}^2 = U_{P_{\text{MC}}}^2 + U_{\Delta P_{\text{PC}}}^2 + U_{\Delta P_{\text{TS}}}^2 \approx U_{P_{\text{MC}}}^2 \quad (\text{C.8})$$

$$\because U_{P_{\text{MC}}} \gg U_{\Delta P_{\text{PC}}} \approx U_{\Delta P_{\text{TS}}}$$

### Enthalpy in mixing chamber $h_{\text{MC}}$

The specific enthalpy in the mixing chamber, located just after the pre-heater, is obtained from measured bulk mean temperature  $T_{\text{r,MC}}$  and pressure  $P_{\text{MC}}$  with Refprop ver.8.0. Therefore, the uncertainty of this enthalpy is the function of Refprop ver.8.0 and determined from measuring uncertainty of  $T_{\text{r,MC}}$  and  $P_{\text{MC}}$ .

$$U_{h_{\text{MC}}} = \left[ f_{\text{Refprop8.0}}(P_{\text{MC}} + U_{P_{\text{MC}}}, T_{\text{MC}} + U_{T_{\text{MC}}}) - f_{\text{Refprop8.0}}(P_{\text{MC}} - U_{P_{\text{MC}}}, T_{\text{MC}} - U_{T_{\text{MC}}}) \right] / 2 \quad (\text{C.9})$$

### Inlet enthalpy of the test section $h_{\text{TSi}}$

The inlet enthalpy of test section is obtained waterside heat-balance through the pre-cooler beginning at the mixing chamber just after the pre-heater.

$$\begin{aligned} h_{\text{TSi}} &= h_{\text{MC}} - (Q_{\text{H}_2\text{O}} - Q_{\text{gain,PC}}) / m_{\text{r}} \\ &= h_{\text{MC}} - \left[ (T_{\text{H}_2\text{O,PCo}} - T_{\text{H}_2\text{O,PCi}}) C_{p_{\text{H}_2\text{O}}} m_{\text{H}_2\text{O,PC}} - Q_{\text{gain,PC}} \right] / m_{\text{r}} \end{aligned} \quad (\text{C.10})$$

The measured values, bulk mean temperature  $T_{\text{H}_2\text{O,PCo}}$ ,  $T_{\text{H}_2\text{O,PCi}}$  and mass flow rate  $W_{\text{H}_2\text{O,PC}}$  and  $W_{\text{r}}$ , dominant the uncertainty of the inlet enthalpy.

$$\begin{aligned} U_{h_{\text{TSi}}}^2 &= \left( \frac{\partial h_{\text{TSi}}}{\partial h_{\text{MC}}} U_{h_{\text{MC}}} \right)^2 + \left( \frac{\partial h_{\text{TSi}}}{\partial T_{\text{H}_2\text{O,PCo}}} U_{T_{\text{H}_2\text{O,PCo}}} \right)^2 + \\ &\quad \left( \frac{\partial h_{\text{TSi}}}{\partial T_{\text{H}_2\text{O,PCi}}} U_{T_{\text{H}_2\text{O,PCi}}} \right)^2 + \left( \frac{\partial h_{\text{TSi}}}{\partial m_{\text{H}_2\text{O,PC}}} U_{m_{\text{H}_2\text{O,PC}}} \right)^2 + \left( \frac{\partial h_{\text{TSi}}}{\partial m_{\text{r}}} U_{m_{\text{r}}} \right)^2 \end{aligned} \quad (\text{C.11})$$

$$\frac{\partial h_{\text{TSi}}}{\partial h_{\text{MC}}} = 1.0 \quad (\text{C.12})$$

$$\frac{\partial h_{\text{TSi}}}{\partial T_{\text{H}_2\text{O,PCo}}} = - \frac{C_{p_{\text{H}_2\text{O}}} m_{\text{H}_2\text{O,PC}}}{m_{\text{r}}} \quad (\text{C.13})$$

$$\frac{\partial h_{\text{TSi}}}{\partial T_{\text{H2O,PCi}}} = \frac{Cp_{\text{H2O}} m_{\text{H2O,PC}}}{m_r} \quad (\text{C.14})$$

$$\frac{\partial h_{\text{TSi}}}{\partial m_{\text{H2O,PC}}} = -\frac{(T_{\text{H2O,PCo}} - T_{\text{H2O,PCi}}) Cp_{\text{H2O}}}{m_r} \quad (\text{C.15})$$

$$\frac{\partial h_{\text{TSi}}}{\partial m_r} = \frac{(T_{\text{H2O,PCo}} - T_{\text{H2O,PCi}}) Cp_{\text{H2O}} m_{\text{H2O,PC}}}{m_r^2} \quad (\text{C.16})$$

### Refrigerant temperature at test-section inlet $T_{\text{r,TSi}}$

$$U_{\text{r,TSi}} = \left[ f_{\text{Refprop8.0}}(P_{\text{TSi}} + U_{P_{\text{TSi}}}, h_{\text{TSi}} + U_{T_{\text{TSi}}}) - f_{\text{Refprop8.0}}(P_{\text{TSi}} - U_{P_{\text{TSi}}}, h_{\text{TSi}} - U_{T_{\text{TSi}}}) \right] / 2 \quad (\text{C.17})$$

### Refrigerant temperature at test-section outlet $h_{\text{TSo}}$

Likewise, the outlet enthalpy of test section is obtained water-side heat-balance through the test-section.

$$\begin{aligned} h_{\text{TSo}} &= h_{\text{TSi}} - (\dot{Q}_{\text{H2O,TS}} - \dot{Q}_{\text{gain,TS}} - \dot{Q}_{\text{cond,TS}}) / m_r \\ &= h_{\text{TSi}} - \left[ (T_{\text{H2O,TSo}} - T_{\text{H2O,TSi}}) Cp_{\text{H2O}} m_{\text{H2O,TS}} - \dot{Q}_{\text{gain,TS}} - \dot{Q}_{\text{cond,TS}} \right] / m_r \end{aligned} \quad (\text{C.18})$$

The measured values, bulk mean temperature  $T_{\text{H2O,TSo}}$ ,  $T_{\text{H2O,TSi}}$  and mass flow rate  $W_{\text{H2O,TS}}$  and  $W_r$ , dominant the uncertainty of the outlet enthalpy.

$$\begin{aligned} U_{h_{\text{TSo}}}^2 &= \left( \frac{\partial h_{\text{TSo}}}{\partial h_{\text{TSi}}} U_{h_{\text{TSi}}} \right)^2 + \left( \frac{\partial h_{\text{TSo}}}{\partial T_{\text{H2O,TSo}}} U_{T_{\text{H2O,TSo}}} \right)^2 \\ &\quad + \left( \frac{\partial h_{\text{TSo}}}{\partial T_{\text{H2O,TSi}}} U_{T_{\text{H2O,TSi}}} \right)^2 + \left( \frac{\partial h_{\text{TSo}}}{\partial m_{\text{H2O,TS}}} U_{m_{\text{H2O,TS}}} \right)^2 \\ &\quad + \left( \frac{\partial h_{\text{TSo}}}{\partial \dot{Q}_{\text{gain,TS}}} U_{\dot{Q}_{\text{gain,TS}}} \right)^2 + \left( \frac{\partial h_{\text{TSo}}}{\partial \dot{Q}_{\text{cond,TS}}} U_{\dot{Q}_{\text{cond,TS}}} \right)^2 + \left( \frac{\partial h_{\text{TSo}}}{\partial m_r} U_{m_r} \right)^2 \end{aligned} \quad (\text{C.19})$$

$$\frac{\partial h_{\text{TSo}}}{\partial h_{\text{TSi}}} = 1.0 \quad (\text{C.20})$$

$$\frac{\partial h_{\text{TSo}}}{\partial T_{\text{H2O,TSo}}} = -\frac{Cp_{\text{H2O}} m_{\text{H2O,TS}}}{m_r} \quad (\text{C.21})$$

$$\frac{\partial h_{\text{TSo}}}{\partial T_{\text{H2O,TSi}}} = \frac{Cp_{\text{H2O}} m_{\text{H2O,TS}}}{m_r} \quad (\text{C.22})$$

$$\frac{\partial h_{\text{TSo}}}{\partial m_{\text{H2O,TS}}} = -\frac{(T_{\text{H2O,TSo}} - T_{\text{H2O,TSi}}) Cp_{\text{H2O}}}{m_r} \quad (\text{C.23})$$

$$\frac{\partial h_{\text{TSo}}}{\partial \dot{Q}_{\text{cond,TS}}} = -\frac{1}{m_r} \quad (\text{C.24})$$

$$\frac{\partial h_{\text{TSo}}}{\partial Q_{\text{gain,TS}}} \approx 0 \quad (\text{C.25})$$

$$\frac{\partial h_{\text{TSo}}}{\partial W_r} = \frac{(T_{\text{H2O,TSO}} - T_{\text{H2O,TSi}}) C_{p_{\text{H2O}}} W_{\text{H2O,TS}}}{W_r^2} \quad (\text{C.26})$$

### Refrigerant temperature at test-section inlet $T_{r,\text{TSO}}$

$$U_{T_{r,\text{TSO}}} = \left[ f_{\text{Refprop8.0}}(P_{\text{TSO}} + U_{P_{\text{TSO}}}, h_{\text{TSO}} + U_{T_{\text{TSO}}}) - f_{\text{Refprop8.0}}(P_{\text{TSO}} - U_{P_{\text{TSO}}}, h_{\text{TSO}} - U_{T_{\text{TSO}}}) \right] / 2 \quad (\text{C.27})$$

### Bulk mean refrigerant temperature at test-section $T_{\text{rb}}$

The representing refrigerant temperature of test-section is as an arithmetic mean of inlet and outlet.

$$T_{\text{rb}} = (T_{r,\text{TSi}} + T_{r,\text{TSO}}) / 2 \quad (\text{C.28})$$

The outlet temperature  $T_{r,\text{TSO}}$  is dependent on inlet temperature  $T_{r,\text{TSi}}$ , because each temperature is obtained from upstream enthalpy. For the exact solution, to know and differentiate the internal functions of Refprop.Ver8.0 is necessary. However, these function is solved computationally and difficult to be differentiated. Alternatively, they are treated as if independent variables for solving the uncertainty of averaged refrigerant temperature.

$$U_{T_{\text{rb}}}^2 = \left( \frac{\partial T_{\text{rb}}}{\partial T_{r,\text{TSi}}} U_{T_{r,\text{TSi}}} \right)^2 + \left( \frac{\partial T_{\text{rb}}}{\partial T_{r,\text{TSO}}} U_{T_{r,\text{TSO}}} \right)^2 = (U_{T_{r,\text{TSi}}}^2 + U_{T_{r,\text{TSO}}}^2) / 4 \quad (\text{C.29})$$

### Averaged heat flux on interior tube-wall $q_{\text{wi}}$

In the way of this measurement, the heat flux on interior tube-wall is non-uniform in circumferential and axial direction of the test tube. However, the heat flux is treated as an averaged value of test section overall. The averaged heat flux through test section on interior tube-wall is obtained as,

$$q_{\text{wi}} = (Q_{\text{H2O,TS}} - Q_{\text{gain}} - Q_{\text{cond}}) / A_{\text{wi}} \quad (\text{C.30})$$

$$= \left[ (T_{\text{H2O,TSO}} - T_{\text{H2O,TSi}}) W_{\text{H2O,TS}} C_{p_{\text{H2O}}} - Q_{\text{gain}} - Q_{\text{cond}} \right] / A_{\text{wi}}$$

Hence, the uncertainty of the averaged heat flux is,

$$U_{q_{\text{wi}}}^2 = \left( \frac{\partial q_{\text{wi}}}{\partial T_{\text{H2O,TSO}}} U_{T_{\text{H2O,TSO}}} \right)^2 + \left( \frac{\partial q_{\text{wi}}}{\partial T_{\text{H2O,TSi}}} U_{T_{\text{H2O,TSi}}} \right)^2 + \left( \frac{\partial q_{\text{wi}}}{\partial m_{\text{H2O,TS}}} U_{m_{\text{H2O,TS}}} \right)^2 \quad (\text{C.31})$$

$$+ \left( \frac{\partial q_{\text{wi}}}{\partial Q_{\text{gain,TS}}} U_{Q_{\text{gain,TS}}} \right)^2 + \left( \frac{\partial q_{\text{wi}}}{\partial Q_{\text{cond,TS}}} U_{Q_{\text{cond,TS}}} \right)^2 + \left( \frac{\partial q_{\text{wi}}}{\partial A_{\text{wi}}} U_{A_{\text{wi}}} \right)^2$$

$$\frac{\partial q_{wi}}{\partial T_{H_2O,TS_o}} = \frac{m_{H_2O,TS} C_{p_{H_2O}}}{A_{wi}} \quad (C.32)$$

$$\frac{\partial q_{wi}}{\partial T_{H_2O,TS_i}} = -\frac{m_{H_2O,TS} C_{p_{H_2O}}}{A_{wi}} \quad (C.33)$$

$$\frac{\partial q_{wi}}{\partial m_{H_2O,TS}} = \frac{(T_{H_2O,TS_o} - T_{H_2O,TS_i}) C_{p_{H_2O}}}{A_{wi}} \quad (C.34)$$

$$\frac{\partial q_{wi}}{\partial Q_{gain,TS}} \approx 0 \quad (C.35)$$

$$\frac{\partial q_{wi}}{\partial Q_{cond,TS}} = -\frac{1}{A_{wi}} \quad (C.36)$$

$$\frac{\partial q_{wi}}{\partial A_{wi}} = -\frac{(T_{H_2O,TS_o} - T_{H_2O,TS_i}) m_{H_2O,TS} C_{p_{H_2O}} - Q_{gain} - Q_{cond}}{A_{wi}^2} \quad (C.37)$$

### Temperature difference $\Delta T$

The temperature difference between bulk refrigerant temperature  $T_{rb}$  and averaged interior tube-wall temperature  $T_{wi}$  is,

$$\Delta T = T_{rb} - T_{wi} \quad (C.38)$$

Hence, the uncertainty is expressed as,

$$U_{\Delta T}^2 = \left( \frac{\partial \Delta T}{\partial T_{rb}} U_{T_{rb}} \right)^2 + \left( \frac{\partial \Delta T}{\partial T_{wi}} U_{T_{wi}} \right)^2 = U_{T_{rb}}^2 + U_{T_{wi}}^2 \quad (C.39)$$

### Heat transfer coefficient $\alpha$

The heat transfer coefficient averaged through the test-section is defined with averaged heat flux and temperature difference as below,

$$\alpha = \frac{q_{wi}}{\Delta T} \quad (C.40)$$

Hence, the uncertainty is expressed as,

$$U_{\alpha}^2 = \left( \frac{\partial \alpha}{\partial q_{wi}} U_{q_{wi}} \right)^2 + \left( \frac{\partial \alpha}{\partial \Delta T} U_{\Delta T} \right)^2 = U_{q_{wi}}^2 + \left( \frac{U_{\Delta T}}{\Delta T} \right)^2 \quad (C.41)$$

## APPENDIX D: MATLAB CODE

### D.1 Film thickness image processing code

#### D.1.1 Main program: cinetofilmthick7

```
% Measures critical reflection light ellipse diameter from jpg images
to
% determine film thickness
% Shortened version of cinetofilmthick6, based on cinetofilmthick5 by
Scott
% Wujek but modified for use with a webcam instead of a high-speed
camera
% Calls user-defined functions readjpgwritematrix and filmthickness7
% Melissa Meyer 7/2/14

clear
close all

set(0,'defaultaxesfontsize',14);
iptsetpref('ImshowBorder','tight')
resultsfilename = 'R134a G100 T50 Film Thicknesses';

codepath = 'G:\Code';
filepath = 'G:\Lab data\Film thickness images\14-04-21';

Dmm = 10.1;      % tube outer diameter (including tape) [mm]
% Dmm = 8.25;      % distance between black tape strips on glass
slide [mm]
% Dmm = 10.071;    % distance between black tape strips on painted
glass slide [mm]
% Dmm = 10.0;

fileinfo=dir(strcat(filepath, '*.*.jpg')); % jpeg file names, dates,
sizes, whether name is a folder, serial date number
for i=1:size(fileinfo,1)
    fileinfo(i).name=strtok(fileinfo(i).name, '.');
end
clear i
filenames=strvcat(fileinfo.name); %#ok<VCAT>
%filenames=strvcat(filenames, 'no1 resize');
clear fileinfo

% image file conversion process
filenames2=[];
for filenum=1:size(filenames,1)
```

```

    if exist(strcat(filenamees(filenamees, :), 's1 images'), 'dir')==0 %
if a folder does not already exist for the jpg file
    disp(filenamees)
    [pxlvalues]=readjpgwritematrix(filepath,
filenamees(filenamees, :));
    filenamees2=strvcat(filenamees2, filenamees);
else
    filesubset=dir(strcat(filenamees(filenamees, :), '*images')); %
file names, dates, sizes, whether name is a folder, mod date as serial
date number
    filesubset=strvcat(filesubset.name); %
file names only
    for row=1:size(filesubset,1)
        temp=strtok(filesubset(row, :)); %
temp is the part of the string in each filesubset row up to the first
delimiter
        filenamees2=strvcat(filenamees2, temp);
    end
    clear temp
end
end

clear pxlvalues

select=zeros(1, size(filenamees, 1));

%critical reflection determination
for filenamees=1:size(filenamees2, 1)
    cd(strcat(filepath, '\', filenamees2(filenamees, :), ' images'));
    %current update is used so that filmthickness .m file is not run
if
    %information in the directory is current.
    currentupdateever=30;
    if exist('currentupdate.mat', 'file')==2
        load currentupdate
    else
        currentupdate=0;
    end

    if currentupdate<currentupdateever
        load pxlvalues
        disp(filenamees)

        cd(codepath)
        [ellipseradius, x, laserposition, maxintensity,
err]=filmthickness7(pxlvalues);

        scale = Dmm/laserposition(7); % [mm/pixel]
        minord = ellipseradius(2)*scale; % ellipse minor diameter
[mm]

```

```

imshow(px1values(:,:)*1.2)
hold on
plot(x(:,2), x(:,3), 'b.')
plot(laserposition(2), laserposition(3), 'r.')

temp=fit_ellipse(x(isfinite(x(:,2)),2), x(isfinite(x(:,2)),3),
gcf);
if isempty(temp)==0
text(10,10, strcat(filenamees2(filename, :), strcat('long axis:
', num2str(temp.long_axis)), strcat('short axis: ',
num2str(temp.short_axis)), laserposition(1) ), 'color',
'g', 'VerticalAlignment', 'top', 'HorizontalAlignment', 'left' )
%#ok<VCAT>
end
clear temp

cd(strcat(filepath, '\\', filenamees2(filename, :), ' images'));
hgsave('samplefig')
hold off

save('ellipseradius', 'ellipseradius')
save('x', 'x')
save('laserposition', 'laserposition')
save('err', 'err')
currentupdate=currentupdateever;
save('currentupdate', 'currentupdate')

cd(codepath)
[garbage, remain1] = strtok(filenamees2(filename, :), '_');
[imagedate, remain2] = strtok(remain1, '_');
imagetime = strtok(remain2, '_');
sheetname = imagedate;
col_header = {'Image Time', 'Ellipse Minor Diameter
[mm]', 'Ellipse Major Axis [pxl]', 'Ellipse Minor Axis [pxl]', 'El. Maj.
Axis Angle wrt Horiz. [rad]', 'El. Center x [pxl]', 'El. Center y
[pxl]', 'Error Msg', 'Name', 'Line'};
err_text = {err.message, err.name, err.line};
xlswrite(resultsfilename, col_header, sheetname, 'A1');
[num, txt, raw] = xlsread(resultsfilename, sheetname);
filledrows = size(raw,1);
nextrow = filledrows+1;

xlswrite(resultsfilename, {imagetime}, sheetname, strcat('A', num2str(next
row)));

xlswrite(resultsfilename, minord, sheetname, strcat('B', num2str(nextrow)
));

xlswrite(resultsfilename, ellipseradius, sheetname, strcat('C', num2str(ne
xtrow)));

```

```

xlswrite(resultsfilename,err_text,sheetname,strcat('H',num2str(nextrow
)));

    end
end

clear ellipseradius
clear x
clear laserposition
clear maxintensity
clear err
clear center
close(gcf)

```

### D.1.2 Called function: readjpgwritematrix

```

function [pxlvalues]=readjpgwritematrix(filepath, filename, varargin)
% This program is a modification of Scott Wujek's readcinwritematrix
that
% reads jpegs instead of cin files.
% Melissa Meyer 11/9/13

% outputs:
% pxlgray:  grayscale pixel values from an entire jpeg file
% saves to folder "{filepath}\{filename} images"
%
% inputs:
% filepath:  complete file path where .jpg file is located
% filename:  file name (without suffix) of jpeg file
% variables should be entered as text strings (ie using ' ')
% varargin:  1) optional cropping function
%            2) number of 90 degress counter clockwise rotations to
undergo

% save and change current directory
initialdir = cd(filepath);

%open image file to read in data
fid = fopen(strcat(filename, '.jpg'), 'r');

% read basic information about image
finfo = imfinfo(filename,'jpg');

% read the trigger time
triggertime = finfo.FileModDate;

% read the image width and height
biWidth = finfo.Width;

```

```

biHeight = finfo.Height;

% read bit per pixel
pxlbit = finfo.BitDepth;

% get pixel values and convert image to grayscale
pxlcolor = imread(filename,'jpg');
pxlgray = rgb2gray(pxlcolor);
pxlvalues = pxlgray;

% save pixel values and file info in .mat files
mkdir(strcat(filename,' images'));
cd(strcat(filename,' images'));
save('pxlvalues', 'pxlvalues')
save('finfo', 'finfo')

% go back to directory where cin file was located
cd(filepath)

fclose(fid);

% go back to main program directory
cd(initialdir)

end

```

### D.1.3 Called function: filmthickness7

```

function [ellipseradius, x, laserposition, maxintensity,
err]=filmthickness7(pxlvalues)
%function finds pertinent information for determining filmthickness
using
%critical angle reflection
%original by Scott Wujek, modified by Melissa Meyer
%
%outputs:
% "ellipse radius" simplified data on ellipse formed by critically
% reflected light
% 1st column is major axis
% 2nd column is minor axis
% 3rd column is angle of major axis w.r.t. horizontal
% 4th and 5th columns are ellipse center
% each row corresponds to frame in video
%
% "x" is raw data describing points where laser found
% 1st column of x is angle from centroid
% 2nd,3rd columns of x locations of light circle
% 4rd, 5th columns of x locations of laser circle
% 6th column of x is radius of reflected circle

```

```

% 7th column of x is radius of laser circle
% each sheet corresponds to frame in video
%
% "laserposition" how centered laser is relative to tube edge
%
%inputs:
% "pxlvalues.mat" should be found
% "Dmm"=tube diameter

numberofangles=120;

%pre allocated variables
ellipsoidradius=NaN(size(pxlvalues,3),5);
x=NaN(numberofangles,7,size(pxlvalues,3));
laserposition=NaN(size(pxlvalues,3),7);
err(1:size(pxlvalues,3))=struct('message','', 'name','', 'line','');
%tubeeq=NaN(2,2,size(cinframes,3));

%re-used variables
gaussian=[1 1 1 1 1 1 1 1; 1 2 2 2 2 2 2 2 1; 1 2 4 4 4 4 4 2 1; 1 2
4 6 6 6 4 2 1; 1 2 4 6 6 6 4 2 1;1 2 4 6 6 6 4 2 1; 1 2 4 4 4 4 4 2 1;
1 2 2 2 2 2 2 2 1; 1 1 1 1 1 1 1 1 1];
maxintensity=NaN(120, size(pxlvalues,3));
for imagenum=1:size(pxlvalues,3)
    try
        rawimage=pxlvalues(:, :, imagenum);

        %find tube diameter in pixels
        bwtube=im2bw(rawimage, 0.05);
        starttube=NaN(size(bwtube,2),1);
        endtube=NaN(size(bwtube,2),1);
        for pxlcol=1:size(bwtube,2)
            starttube(pxlcol)=find(bwtube(:,pxlcol)>0,1,'first');
            endtube(pxlcol)=find(bwtube(:,pxlcol)>0,1,'last');
        end
        Dtubepxl = endtube-starttube;
        Dtubepxavg = mean(Dtubepxl);

        %find area and centroid of area which laser directly
        illuminates (should be washed out)
        laserdot=im2bw(rawimage, 0.95);
        lasercentroid=regionprops(bwlabel(laserdot), 'centroid',
'area', 'MajorAxisLength', 'MinorAxisLength', 'Orientation');

        if size(lasercentroid,1)>1
            regionarea=zeros(size(lasercentroid,1),1);
            for region=1:size(lasercentroid,1)
                regionarea(region)=lasercentroid(region).Area;
            end
        end
    end
end

```

```

        lasercentroid=lasercentroid(regionarea==max(regionarea));
        laserdot=bwareaopen(laserdot, max(regionarea)-1);
    end
    laserposition(imagenum,:)=[imagenum,
lasercentroid.Centroid(1), lasercentroid.Centroid(2),
lasercentroid.MajorAxisLength, lasercentroid.MinorAxisLength,
lasercentroid.Orientation, Dtubepxavg];
    %create a smoothed version of the original image
    smoothimage=uint8(filter2(gaussian./sum(gaussian(:)),
single(rawimage)));

    radius=NaN(numberofangles, 7);

    for anglenumber=1:numberofangles
        angle=(360/numberofangles)*anglenumber*pi/180;
        x1=lasercentroid.Centroid(1)+(1000)*cos(angle);
        y1=lasercentroid.Centroid(2)-(1000)*sin(angle);

        vectlength=round((lasercentroid.Centroid(1)-
x1)^2+(lasercentroid.Centroid(2)- y1)^2)^0.5;
        xvalues=linspace(lasercentroid.Centroid(1),x1,vectlength);
        yvalues=linspace(lasercentroid.Centroid(2),y1,vectlength);
        if exist('Xgrid', 'var')==0 || exist('Ygrid', 'var')==0
            [Xgrid,Ygrid]=meshgrid(1:size(smoothimage,2),
1:size(smoothimage,1));
        end
        lineprofile=(qinterp2(Xgrid, Ygrid,single(smoothimage),
xvalues, yvalues))';

        lineprofile(isnan(lineprofile))=lineprofile(find(isnan(lineprofile),
1, 'first')-1);

        if anglenumber==1;
            lineprofiletemp=NaN(size(radius,1),
size(lineprofile,1));
        end

        lineprofiletemp(anglenumber,:)=lineprofile';
        radius(anglenumber,1)=angle;

    end

    %    lineprofiletemp=filter2(ones(3)/9,
[[lineprofiletemp(end,1),
lineprofiletemp(end,:),lineprofiletemp(end,end)];[lineprofiletemp(:,1)
,lineprofiletemp,lineprofiletemp(:,end)];[lineprofiletemp(1,1),
lineprofiletemp(1,:),lineprofiletemp(1,end)]], 'valid');
        slopetemp=filter2([.5, .5 , 0, -.5, -.5],
[lineprofiletemp(:,1),lineprofiletemp,lineprofiletemp(:,end)],
'valid');

```

```

laseredgetemp=NaN(size(lineprofiletemp,1),1);
startsearchedgetemp=NaN(size(lineprofiletemp,1),1);
endsearchedgetemp=NaN(size(lineprofiletemp,1),1);
AVGlineprofiletemp=NaN(size(lineprofiletemp,1),1);
edgedetect=NaN(size(lineprofiletemp,1),1);
for row=1:size(lineprofiletemp,1)
    laseredgetemp(row,1)=find(lineprofiletemp(row,:)>255*.95,
1, 'last');
end

laseredgeposition=[lasercentroid.Centroid(1)+laseredgetemp.*cos(radius
(:,1))*(1000)/size(lineprofile,1), lasercentroid.Centroid(2)-
laseredgetemp.*sin(radius(:,1))*(1000)/size(lineprofile,1)];
    %this step added incase isolated pixels are ~as bright as
laser dot
    %(would be unnecessary if used laser dot in first place, but
%interpolation along lines is slow)

redoanglenumber=find(laserdot(round(laseredgeposition(:,2))+(round(las
eredgeposition(:,1))-1)*size(laserdot, 1))==0);
for redo=1:size(redoanglenumber,1)
    anglenumber=redoanglenumber(redo);
    angle=(360/numberofangles)*anglenumber*pi/180;
    x1=lasercentroid.Centroid(1)+(1000)*cos(angle);
    y1=lasercentroid.Centroid(2)-(1000)*sin(angle);
    xvalues=linspace(lasercentroid.Centroid(1),x1,vectlength);
    yvalues=linspace(lasercentroid.Centroid(2),y1,vectlength);
    laserprofile=(qinterp2(Xgrid, Ygrid,single(laserdot),
xvalues, yvalues));
    laseredgetemp(anglenumber,1)=find(laserprofile>.95, 1,
'last');

laseredgeposition(anglenumber,:)=lasercentroid.Centroid(1)+laseredget
emp(anglenumber,1).*cos(radius(anglenumber,1))*(1000)/size(lineprofile
,1), lasercentroid.Centroid(2)-
laseredgetemp(anglenumber,1).*sin(radius(anglenumber,1))*(1000)/size(l
ineprofile,1)];
end

for row=1:size(lineprofiletemp,1)
    if sum(slopetemp(row,laseredgetemp(row):end)<0)>=1;
        if radius(row,1) > deg2rad(120) && radius(row,1) <
deg2rad(265)
            %
startsearchedgetemp(row,1)=find(slopetemp(row,laseredgetemp(row):end)<
0, 1, 'first')+laseredgetemp(row);

startsearchedgetemp(row,1)=find(lineprofiletemp(row,laseredgetemp(row)
:end)<0.25*lineprofiletemp(row,laseredgetemp(row)), 1,
'first')+laseredgetemp(row);

```

```

else

startsearchedgetemp(row,1)=find(lineprofiletemp(row,laseredgetemp(row)
:end)<0.3*lineprofiletemp(row,laseredgetemp(row)), 1,
'first')+laseredgetemp(row);
    end
    end
    if isfinite(startsearchedgetemp(row)) &&
max(lineprofiletemp(row,
startsearchedgetemp(row):end))>=1.05*lineprofiletemp(row,
startsearchedgetemp(row))

maxintensity(row,imagenum)=max(lineprofiletemp(row,startsearchedgetemp
(row):end));
    endsearchedgetemp(row,1)=startsearchedgetemp(row)-
1+find(lineprofiletemp(row,startsearchedgetemp(row):end)==maxintensity
(row,imagenum), 1, 'last');

    end
    if isfinite(startsearchedgetemp(row)) &&
isfinite(endsearchedgetemp(row)) &&
max(lineprofiletemp(row,startsearchedgetemp(row):end))>=1.05*lineprofi
letemp(row, startsearchedgetemp(row)) &&
endsearchedgetemp(row)>startsearchedgetemp(row)

AVGlineprofiletemp(row,1)=(lineprofiletemp(row,endsearchedgetemp(row))
+min(lineprofiletemp(row,startsearchedgetemp(row):endsearchedgetemp(ro
w))))/2;
    end
    if isfinite(AVGlineprofiletemp(row))
    %
    edgedetect(row,1)=endsearchedgetemp(row,1); % ellipse defined as
last point with max intensity
    %
    maxslope(row,imagenum) =
max(slopetemp(row,startsearchedgetemp(row):endsearchedgetemp(row)));
    %
    edgedetect(row,1) =
find(slopetemp(row,startsearchedgetemp(row):endsearchedgetemp(row))==m
axslope(row,imagenum),1,'last')+startsearchedgetemp(row)-1;
    edgedetect(row,1)=startsearchedgetemp(row)-
1+find(lineprofiletemp(row,startsearchedgetemp(row):endsearchedgetemp(
row))<AVGlineprofiletemp(row), 1, 'last');
    end
    end
    %
    startsearchposition=[lasercentroid.Centroid(1)+startsearchedgetemp.*co
s(radius(:,1)+tubeangle(imagenum))*(1000)/size(lineprofile,1),
lasercentroid.Centroid(2)-
startsearchedgetemp.*sin(radius(:,1)+tubeangle(imagenum))*(1000)/size(
lineprofile,1)];
    %
    endsearchposition=[lasercentroid.Centroid(1)+endsearchedgetemp.*cos(ra

```

```

dius(:,1)+tubeangle(imagenum))*(1000)/size(lineprofile,1),
lasercentroid.Centroid(2)-
endsearchedgetemp.*sin(radius(:,1)+tubeangle(imagenum))*(1000)/size(li
neprofile,1)];

edgedetectposition=[lasercentroid.Centroid(1)+edgedetect.*cos(radius(:
,1))*(1000)/size(lineprofile,1), lasercentroid.Centroid(2)-
edgedetect.*sin(radius(:,1))*(1000)/size(lineprofile,1)];
    radius(:,2:7)=[edgedetectposition, laseredgeposition,
edgedetect*(1000)/size(lineprofile,1),
laseredgetemp*(1000)/size(lineprofile,1)];

    % select which points are used to fit the ellipse
    %     distfromcenter = edgedetect-startsearchedgetemp;
    distfromcenter = edgedetect-laseredgetemp;
    for row=1:size(lineprofiletemp,1)
        %         if radius(row,1) < deg2rad(45) || radius(row,1)
> deg2rad(315) || (radius(row,1) > deg2rad(135) && radius(row,1) <
deg2rad(225))
            %             radius(row,2) = NaN;
            %         end
            %         if radius(row,2)<ledleftbound ||
radius(row,2)>ledrightbound
                %             radius(row,2) = NaN;
                %         end
                %         if distfromcenter(row)<0.5*max(distfromcenter)
                %             radius(row,2) = NaN;
                %         end
                %         if distfromcenter(row)<0.5*max(distfromcenter) ||
distfromcenter(row)>0.95*max(distfromcenter) || radius(row,1) <
deg2rad(45) || radius(row,1) > deg2rad(315) || (radius(row,1) >
deg2rad(135) && radius(row,1) < deg2rad(225))
                    radius(row,2) = NaN;
                end
            end
        end

        ellipsedata=fit_ellipse(radius(isfinite(radius(:,2)),2),
radius(isfinite(radius(:,2)),3));

        if isempty(ellipsedata)==0
            if isempty(ellipsedata.long_axis)==0
                %eliminate points which are off from ellipse

radcheckest=((ellipsedata.long_axis/2)*(ellipsedata.short_axis/2))./((
(ellipsedata.short_axis/2)*cos(radius(:,1))).^2+((ellipsedata.long_axi
s/2)*sin(radius(:,1))).^2).^0.5);
                radcheck=radcheckest-radius(:,6);
                stdradcheck=nanstd(radcheck);
                centerdistance=(sum((lasercentroid.Centroid-
[ellipsedata.X0_in, ellipsedata.Y0_in]).^2))^0.5;

```

```

        radius(abs(radcheck) -
centerdistance>stdradcheck, [2:3, 6])=NaN(sum(abs(radcheck) -
centerdistance>stdradcheck), 3);
        end
    end

    ellipsedata=fit_ellipse(radius(isfinite(radius(:,2)),2),
radius(isfinite(radius(:,2)),3));

    %ellipseradius is major and minor axis of ellipse formed by
least
    %square fit of light circle
    if isempty(ellipsedata)==0
        if isempty(ellipsedata.long_axis)==0
            ellipseradius(imagenum, :)=[ellipsedata.long_axis,
ellipsedata.short_axis, ellipsedata.phi, ellipsedata.X0_in,
ellipsedata.Y0_in];
        end
    end
    clear ellipsedata

    radius(:,1)=mod(radius(:,1),2*pi);
    %1st column of x is angle from centroid
    %2nd,3rd columns of x locations of light circle
    %4rd, 5th columns of x locations of laser circle
    %6th column of x is radius of reflected circle
    %7th column of x is radius of laser circle
    %8 column of x is pixel value slope where light circle was
found
    x(:, :, imagenum)=radius;
    catch ME
        err(imagenum).message = ME.message;
        err(imagenum).name = ME.stack.name;
        err(imagenum).line = ME.stack.line;
        return
    end
end

ellipseradius=NaN(size(x,3), 5);
for frame=1:size(x,3)
    if sum(isfinite(x(:,2,frame)))>=3
        ellipsedata=fit_ellipse(x(isfinite(x(:,2,frame)),2,frame),
x(isfinite(x(:,2,frame)),3,frame));
        if isempty(ellipsedata)==0
            if isempty(ellipsedata.long_axis)==0
                ellipseradius(frame, :)=[ellipsedata.long_axis,
ellipsedata.short_axis, ellipsedata.phi, ellipsedata.X0_in,
ellipsedata.Y0_in];
            end
        end
    end
end

```

end  
end  
end

## D.2 Optical model of critical light reflection for round tube

### D.2.1 Main program: refractionmap6

```
% Scott Wujek
% Models optical interactions between a point source of light and
% concentric cylinders
% Later version of film_thickness_optical_model
% Additional comments by Melissa Meyer, July 2013
% Modified by Melissa Meyer, October 2013 (added Excel storage at end)
%% Initialize program
clear
close all
tic
set(0,'defaultaxesfontsize',14);
scrsz = get(0,'ScreenSize');
%% Indices of refraction
%ntape=1.5;
% ntube=1.43;
ntube=1.385;
%ntube = 1.473; % Pyrex
% noil=1.25;
nliq=1.195;
nvap=1.0;
fluidname = '';

%% Geometric constants
%all lengths in mm
% Douter=9.525;      % outer diameter of 3/8" tube
% tubethick=1.5875; % 1/16"
Douter=10.1;
tubethick=2.0;
Router=Douter/2;
clear Douter
Rinner=Router-tubethick;

filmthickoptions=[0, 1E-3, 10E-3, 20E-3];
% filmthickoptions=[30E-3, 40E-3, 50E-3, 75E-3, 100E-3];

% Loop 1: repeat for various film thicknesses
for filmthicknum=1:length(filmthickoptions)
    filmthick=filmthickoptions(filmthicknum);

    Rfilm=Rinner-filmthick;
    R=[Rfilm, Rinner, Router];

    clear Rfilm
%     n=[ngas, noil, ntube];
```

```

n=[nvap, nliq, ntube];
%% modify for dry tube
if filmthick==0
    n=[n(1), n(3)];
%    R=R(2:3);
    R=R(2:end);
end

%% Variables
position=[R(end), 0]; %position where light enters tube
surface=size(R,2); %surface where light enters tube (outer tube
surface)

    phioptions=[0.51:0.002:1.49]*pi; % initial light ray angle
%#ok<NBRAK>
    ellipseangleoptions=[.01, .05, .075, 0.1, .125, 0.15, 0.2, 0.25,
.3, .35, .401, .45, 0.5, .55, .599, .65, .7, .75, .8, .85, .875, .9,
.925, .95, .99]*pi; %angle that the cross sections of tube make with
axis
    angleintensitypeak=pi*1;
    sigma=(pi/2)/4; % standard deviation for Gaussian distribution of
intensity
    %intensity distribution of light entrance as a function of light
    %angle--modified from Scott's to fit equation for Gaussian
distribution
    intensityvalues=(1/(2*pi*sigma^2)^0.5)*exp(-(((phioptions-
angleintensitypeak).^2)/(2*sigma^2)));
    %phioptions=pi

    %intensityvalues=2*(0.5-abs(phioptions/pi-1)).^2;
    accuracy=0.99; %ratio of light which must strike outer surface
again for program to consider it good enough

    %% Light out determinations
    anglestep=pi/1440;
    anglefromhoriz=single([anglestep:anglestep:2*pi-anglestep]');
%#ok<NBRAK>
    intensitymodematrix=NaN(length(phioptions), 1,
length(ellipseangleoptions), 'single');
    anglemodematrix=NaN(length(phioptions), 1,
length(ellipseangleoptions), 'single');
    permutations=NaN(length(ellipseangleoptions), 1);
    initialbeamlength=NaN(1, length(phioptions),
length(ellipseangleoptions));
    % Loop 2: repeat for various cross-sectional plane angles
    for ellipseanglenum=1:length(ellipseangleoptions)
        lightoutmatrix=[];
        % Loop 3: repeat for various initial light ray angles
        for lightanglenum=1:length(phioptions)

```

```

[lightout]=refractionfun(R,n,intensityvalues(lightanglenum), position,
phioptions(lightanglenum), surface,
ellipseangleoptions(ellipseanglenum), accuracy);
    lightoutmatrix=[lightoutmatrix,
[[lightout.intensity]./[lightout.lengthsquard]; [lightout.position];
[lightout.path]; [lightout.path2]; repmat(phioptions(lightanglenum),
[1,(size(lightout,2))])]]; %#ok<AGROW>
    end
    clear lightout
    clear initialbeamlength
    nearestangle=angle(complex(lightoutmatrix(2,:),
lightoutmatrix(3,:))); % convert exit position from ellipse (x,y)
coordinates to angle
    lightoutmatrix=[lightoutmatrix;nearestangle]; %#ok<AGROW>
    clear nearestangle
    %% determine intensity out at each "radial" angle due to the
different modes of reflection

permutations(ellipseanglenum,1:length(unique(lightoutmatrix(7,:)))=un
ique(lightoutmatrix(7,:))); % lists all the modes or light travel
paths for each ellipse angle
    % Loop 4: repeat for each mode (number of modes changes for
different ellipse angles)
    for mode=1:find(permutations(ellipseanglenum,:), 1, 'last');
        %if
length(lightoutmatrix(9,lightoutmatrix(7,:)==permutations(ellipseangle
num,mode)))>1

phitemp=lightoutmatrix(8,lightoutmatrix(7,:)==permutations(ellipseangl
enum,mode)); % initial angles of all rays that travel a given mode

intensitytemp=lightoutmatrix(1,lightoutmatrix(7,:)==permutations(ellip
seanglenum,mode));

positiontemp=lightoutmatrix(9,lightoutmatrix(7,:)==permutations(ellips
eanglenum,mode));

intensitymodematrix(:,mode,ellipseanglenum)=NaN(length(phioptions),1,1
);

anglemodematrix(:,mode,ellipseanglenum)=NaN(length(phioptions),1,1);
    % Loop 5: repeat for each ray that belongs to the mode
    for selection=1:length(phitemp)
        intensitymodematrix(phitemp(selection)==phioptions,
mode, ellipseanglenum)=intensitytemp(selection);
        anglemodematrix(phitemp(selection)==phioptions, mode,
ellipseanglenum)=wrapTo2Pi(positiontemp(selection));
    end

%end

```

```

        end
    end
    clear ellipseanglenum
    clear lightanglenum
    %clear lightoutmatrix
    % consolidate modes for all ellipse angles
    permutations2=unique(permutations);
    permutations2(permutations2==0)=[];
    permutations2=reshape(permutations2, 1, []);
    intensitymodematrix2=NaN(size(intensitymodematrix));
    anglemodematrix2=NaN(size(anglemodematrix));
    % Loop 6: repeat for each ellipse angle
    for ellipseanglenum=1:length(ellipseangleoptions)
        % Loop 7: repeat for each unique mode
        for mode=1:length(permutations2)
            if
sum(permutations(ellipseanglenum, :)==permutations2(mode))==1 % if
there is one matching mode

intensitymodematrix2(:,mode,ellipseanglenum)=intensitymodematrix(:,per
mutations(ellipseanglenum, :)==permutations2(mode), ellipseanglenum);

anglemodematrix2(:,mode,ellipseanglenum)=anglemodematrix(:,permutation
s(ellipseanglenum, :)==permutations2(mode), ellipseanglenum);

            end
        end
    end
    end

    anglemodematrix=anglemodematrix2;
    anglemodematrix(anglemodematrix==0)=NaN;
    clear anglemodematrix2;
    intensitymodematrix=intensitymodematrix2;
    clear intensitymodematrix2;

    % Interpolate intensities around outer edge of tube
    intensitymatrix=zeros(length(anglefromhoriz),
length(ellipseangleoptions));
    intensitymatrixmodal=zeros(length(anglefromhoriz),
size(intensitymodematrix,2), length(ellipseangleoptions));
    dtheta=anglefromhoriz(2)-anglefromhoriz(1);
    % Loop 8: repeat for each ellipse angle
    for ellipseanglenum=1:length(ellipseangleoptions)
        % Loop 9: repeat for each mode
        for mode=1:size(intensitymodematrix,2)

indices=find(isfinite(anglemodematrix(:,mode,ellipseanglenum))); %
because values corresponding to missing modes were replaced with NaN
indicesiso=indices;

```

```

        indices=indices((indices(2:end)-indices(1:end-1))==1); %
consecutive indices (for continuous exiting light)
        indicesiso=setdiff(indicesiso,indices); % gives values
in indicesiso that are not in indices (nonconsecutive indices)

        %for continuous values
        % Loop 10: repeat for each consecutive exit angle
        for step=1:length(indices)

anglebound=anglemodematrix(indices(step):indices(step)+1, mode,
ellipseanglenum); % angular exit position slice
        if abs(anglebound(1)-anglebound(2))<pi*1.5
            insertindex=find(anglefromhoriz<=max(anglebound)&
anglefromhoriz>min(anglebound)); % finds index of discrete angle
contained within slice
            if isempty(insertindex)==0
                % interpolates to find intensity in the slice
                intensitymatrix(insertindex,
ellipseanglenum)=intensitymatrix(insertindex,
ellipseanglenum)+interp1(anglebound,
intensitymodematrix(indices(step):indices(step)+1, mode,
ellipseanglenum), anglefromhoriz(insertindex));
                intensitymatrixmodal(insertindex, mode,
ellipseanglenum)=intensitymatrixmodal(insertindex, mode,
ellipseanglenum)+interp1(anglebound,
intensitymodematrix(indices(step):indices(step)+1, mode,
ellipseanglenum), anglefromhoriz(insertindex));
            else

insertindex=[find(anglefromhoriz<=min(anglebound), 1, 'last'),
find(anglefromhoriz>min(anglebound), 1, 'first')];
                intensitymatrix(insertindex,
ellipseanglenum)=intensitymatrix(insertindex,
ellipseanglenum)+interp1(anglebound,
intensitymodematrix(indices(step):indices(step)+1, mode,
ellipseanglenum), anglefromhoriz(insertindex), 'linear', 'extrap');
            end
            %
            %
            insertindex=find(wrapToPi(anglefromhoriz)<=max(wrapToPi(anglebound))&
wrapToPi(anglefromhoriz)>min(wrapToPi(anglebound)));
            %
            %
            if isempty(insertindex)==0
                intensitymatrix(insertindex,
ellipseanglenum)=intensitymatrix(insertindex,
ellipseanglenum)+interp1(wrapToPi(anglebound),
intensitymodematrix(indices(step):indices(step)+1, mode,
ellipseanglenum), wrapToPi(anglefromhoriz(insertindex)));
            %
            intensitymatrixmodal(insertindex, mode,
ellipseanglenum)=intensitymatrixmodal(insertindex,
ellipseanglenum)+interp1(wrapToPi(anglebound),

```

```

intensitymodematrix(indices(step):indices(step)+1, mode,
ellipseanglenum), wrapToPi(anglefromhoriz(insertindex)));
        %
    end
end
end
%for isolated values
% Loop 11: repeat for isolated exit angles
for step=1:length(indicesiso)
    insertindex=find(abs(anglefromhoriz-
anglemodematrix(indicesiso(step)))==min(abs(anglefromhoriz-
anglemodematrix(indicesiso(step))))); % find closest discrete angle
    if length(insertindex)==1
        intensitymatrix(insertindex,
ellipseanglenum)=intensitymatrix(insertindex,
ellipseanglenum)+intensitymodematrix(indicesiso(step), mode,
ellipseanglenum);
    elseif length(insertindex)==2;
        intensitymatrix(insertindex,
ellipseanglenum)=intensitymatrix(insertindex,
ellipseanglenum)+intensitymodematrix(indicesiso(step), mode,
ellipseanglenum)/2;
    end
end
end

end

end

intensitymatrix(intensitymatrix==0)=NaN;
intensitymatrixmodal(intensitymatrixmodal==0)=NaN;

%% plotting of results
Z= (max(R)*sin(repmat(anglefromhoriz,
[1,length(ellipseangleoptions)])))/tan(repmat(ellipseangleoptions,
[length(anglefromhoriz),1])); % global axial coordinate of each
point around outer edge of each ellipse

% [X,Y] = pol2cart(anglefromhoriz,max(R));

importantmodes=(nansum(nansum(intensitymodematrix,3),1)./nansum(intens
itymodematrix(:))>0.005; % finds each mode whose summed intensity
accounts for more than 0.5% of total

intensitymatriximportant=squeeze(nansum(intensitymatrixmodal(:,importa
ntmodes,:),2)); % sums intensity from all important modes at
each discrete angular position

% figure
%
bar(nansum(nansum(intensitymodematrix(:,importantmodes,:),3),1)./nansu
m(intensitymodematrix(:)))

```

```

% temp={num2str(permutations2(importantmodes)')};
% set(gca,'XTickLabel',temp)
% xlabel('Mode')
% ylabel('Normalized intensity [-]')

% figure
% plot(phioptions,
squeeze(anglemodematrix(:,importantmodes,13)), '.')
% legend(num2str(permutations2(importantmodes)'))
% xlabel('Angle light leaves point source [-]')
% ylabel('Polar angle [-]')
% xlim([pi/2, 3*pi/2])
% ylim([0, 2*pi])
% set(gca,'XTick',0:pi/2:2*pi)
% set(gca,'YTick',0:pi/2:2*pi)
% set(gca,'FontName','Symbol')
% set(gca,'XTickLabel',{'0','p/2','p','3p/2','2p'})
% set(gca,'YTickLabel',{'0','p/2','p','3p/2','2p'})
% %
% figure
% plot(phioptions,
squeeze(intensitymodematrix(:,importantmodes,13))/max(intensitymodemat
rix(:)), '.')
% legend(num2str(permutations2(importantmodes)'))
% xlabel('Angle light leaves point source [-]')
% ylabel('Normalized intensity [-]')
% xlim([pi/2, 3*pi/2])
% set(gca,'XTick',0:pi/2:2*pi)
% set(gca,'FontName','Symbol')
% set(gca,'XTickLabel',{'0','p/2','p','3p/2','2p'})

% for mode=1:length(importantmodes)
% if importantmodes(mode)==1
% figure
% plot3(repmat(anglefromhoriz,
[1,length(ellipseangleoptions)]), repmat(ellipseangleoptions,
[length(anglefromhoriz),1]), squeeze(intensitymatrixmodal(:,mode,:)))
% % hold on
% % plot3(squeeze(anglemodematrix(:,mode,:)),
repmat(ellipseangleoptions, [length(anglemodematrix),1]),
squeeze(intensitymodematrix(:,mode,:)), '.')
% title(['Mode: ', num2str(permutations2(mode))])
% xlabel('Polar angle [-]')
% xlim([0, 2*pi])
% ylabel('Ellipse angle [-]')
% ylim([0,pi])
% zlabel('Normalized intensity[-]')
% zlim([0, nanmax(intensitymatrixmodal(:))])
% set(gca,'XTick',0:pi/2:2*pi)
% set(gca,'YTick',0:pi/4:pi)

```

```

%         set(gca,'FontName','Symbol')
%         set(gca,'XTickLabel',{'0','p/2','p','3p/2','2p'})
%         set(gca,'YTickLabel',{'0','p/4','p/2','3p/4','p'})
%
%     end
% end

% figure
% plot3(repmat(anglefromhoriz, [1,length(ellipseangleoptions)]),
repmat(ellipseangleoptions, [length(anglefromhoriz),1]),
squeeze(nansum(intensitymatrixmodal,2)))
% xlabel('Polar angle [-]')
% xlim([0, 2*pi])
% ylabel('Ellipse angle [-]')
% ylim([0,pi])
% zlabel('Normalized intensity[-]')
% zlim([0, nanmax(intensitymatrixmodal(:))])
% set(gca,'XTick',0:pi/2:2*pi)
% set(gca,'YTick',0:pi/4:pi)
% set(gca,'FontName','Symbol')
% set(gca,'XTickLabel',{'0','p/2','p','3p/2','2p'})
% set(gca,'YTickLabel',{'0','p/4','p/2','3p/4','p'})

% figure
% surf([repmat(X, [1,length(ellipseangleoptions)]),
flipud(X(:,1))],[repmat(Y, [1,length(ellipseangleoptions)]),
flipud(Y(:,1))],[Z, flipud(Z(:,1))],
(double([intensitymatriximportant,
flipud(intensitymatriximportant(:,1))])) %first column is repeated
upside down at end to complete the tube
% shading interp
% colormap bone
% axis('equal')
% xlabel('X')
% ylabel('Y')
% zlabel('Z')
% zlim([max(min(Z(:)),-2*(max(R))),min(max(Z(:)),2*max(R))])

%%

viewangleoptions=[0 10 20 30 45]*pi/180; %#ok<NBRAK>
% viewangleoptions=0; % angle between camera line of sight and
light ellipse centerline
minord=NaN(size(viewangleoptions));
% Loop 12: repeat for all viewing angles
for step=1:length(viewangleoptions)
viewangle=viewangleoptions(step);
angledif=anglefromhoriz-viewangle;

```

```

[X2,Y2] = pol2cart(angledif,max(R));    % transform polar
coordinates to Cartesian
[temp,indices]=sort(wrapToPi(angledif));
indices2=find(wrapToPi(angledif)>=-pi/2 &
wrapToPi(angledif)<=pi/2);    % finds indices for non-negative x
coordinates
nonnegX=indices(ismember(indices,indices2));

clear temp
clear indices
clear indices2

%Realistic view
figure('Position',[1 1, scrsz(3), scrsz(4)])
surf([repmat(Y2(nonnegX,:), [1,length(ellipseangleoptions)]),
Y2(flipud(nonnegX),1)], [Z(nonnegX,:), Z(flipud(nonnegX),1)],
(double([intensitymatriximportant(nonnegX,:),
flipud(intensitymatriximportant(nonnegX,1))])) %first column is
repeated upside down at end to complete the tube
shading interp
colormap bone
daspect([1, 1,
max(max(intensitymatriximportant(nonnegX,:))/max(Z(isfinite(Z))))]
xlabel('Y [mm]')
ylabel('Z [mm]')
ylim([max(min(Z(:)), -2*(max(R))), min(max(Z(:)), 2*max(R))])
xlim([-max(R), max(R)])
view(90,90)

% critical minor diameter determination
crosssliceindex=find(sum(abs(Z),1)==min(sum(abs(Z),1)));    %
find index of ellipse that is closest to a vertical cross-section of
tube
intensityslice=intensitymatriximportant(nonnegX,
crosssliceindex);
Yslice=Y2(nonnegX);
center=-sin(viewangle)*max(R);

minord(step)=abs(Yslice(max(intensityslice(Yslice<center))==intensitys
lice(Yslice<center))-
Yslice(find(max(intensityslice(Yslice>center))==intensityslice, 1,
'last')));    % find distance between y coordinates of points of
maximum intensity on opposite sides of center
end
disp(filmthick)
disp([viewangleoptions, minord])

% plot(rad2deg(viewangleoptions), minord)
% xlim([0, max(rad2deg(viewangleoptions))]);
% xlabel('Viewing angle [degrees]')
% ylabel('Projected minor diameter [mm]')

```

```

        minordgrid(:,:,filmthicknum)=[repmat(filmthick,
[length(minord),1]), rad2deg(viewangleoptions), minord];
        toc
end

figure
plot(squeeze(minordgrid(:,2,:)), squeeze(minordgrid(:,3,:)))
legend([repmat('t=',
[length(filmthickoptions),1]),num2str(filmthickoptions')])
xlim([0, max(minordgrid(:,2,1))]);
xlabel('Viewing angle [degrees]')
ylabel('Projected minor diameter [mm]')

% figure
% plot(squeeze(minordgrid(1,1,:)), squeeze(minordgrid(1,3,:)))
% xlabel('Film thickness [mm]')
% ylabel('Projected minor diameter [mm]')
% xlim([0, max(squeeze(minordgrid(1,1,:)))]))
%
filename = 'Refraction Map Results';
sheetname = [fluidname ' nt=' num2str(ntube) ' n=' num2str(nliq) '
OD=' num2str(2*Router) ' t=' num2str(tubethick)];
col_header = {'Film thickness [mm]','Projected minor diameter
[mm]','Viewing angle [deg]'};
minordgrid_all = [];
for j=1:size(minordgrid,3)
minordgrid_all = cat(1,minordgrid_all,minordgrid(:,:,j));
end
xlswrite(filename,col_header,sheetname,'A1:C1');
[num,txt,row] = xlsread(filename,sheetname);
filledrows = size(row,1);
nextrow = filledrows+1;
xlswrite(filename,minordgrid_all(:,1,:),sheetname,strcat('A',num2str(n
extrow)));
xlswrite(filename,minordgrid_all(:,3,:),sheetname,strcat('B',num2str(n
extrow)));
xlswrite(filename,minordgrid_all(:,2,:),sheetname,strcat('C',num2str(n
extrow)));

```

## D.2.2 Called function: refractionfun

```

function[lightout,initialbeamlength]=refractionfun(R,n,intensity,
position, phi, surface, ellipseangle, accuracy)

%
*****
*
% FUNCTION FOR DETERMINING ANGLES AND INTENSITIES AT EACH INTERACTION
OF

```

```

% LIGHT RAY WITH A SURFACE
% Scott Wujek
% Mist to Annular Flow Development Quantified by Novel Video Analysis
% Methods, 2011 PhD thesis, Appendix A.3.1
% Modified by Melissa Meyer 7-24-13
%
*****
*

% n=[1, 1.25, 1.43];
% R=[2.9750, 3.1750 , 4.7625];
% position=[R(end), 0];
% intensity=1;
% phi= pi*.9;
% surface=size(R,2);
% ellipseangle=pi/4;
% accuracy=0.999;
light.phi=wrapToPi(phi); % angle values converted to between [-pi,
pi] instead of [0, 2*pi]
light.intensity=intensity;
light.position=position;
light.surface=surface;
intensity0=intensity;
clear phi
clear intensity
clear position
clear surface;

lightgrid{1}=light;

Rmajor=R/sin(ellipseangle); % long radius of ellipse; corrected
mistake from previous codes
n0=n(light.surface); % index of refraction of surface light hits
first

% initialize counters and loop stop criterion
interaction=1; % count of light ray hitting an interface
branch=1; % count of light ray directions of travel
lightoutnum=1; % count of light rays exiting the tube
lightout=struct('intensity', {}, 'position', {}, 'path', {});
completed=0;
while completed~=1

    % find location of next interface interaction

    if ellipseangle~=0
        % find (x,y) coordinates where ray beginning at light.position
and
        % traveling in the direction of light.phi intersects the edge
of
        % each ellipse (each interface)

```

```

        A=tan(light.phi)^2+Rmajor.^2./R.^2;
        B=-
2*light.position(1)*tan(light.phi)^2+2*tan(light.phi)*light.position(2
);
        C=light.position(1)^2*tan(light.phi)^2-
2*tan(light.phi)*light.position(1)*light.position(2)-
Rmajor.^2+light.position(2)^2;
        locationtemp=(-B+(B^2-4*A.*C).^0.5)/(2*A);
        locationtemp(end+1:end+size(R,2))=(-B-(B^2-
4*A.*C).^0.5)/(2*A);
        locationtemp(2,:)=tan(light.phi)*(locationtemp-
light.position(1))+light.position(2);
        % clear A
        % clear B
        % clear C
    else
        locationtemp=[R, -R];
        locationtemp(2,:)=tan(light.phi)*(locationtemp-
light.position(1))+light.position(2);
    end

    locationpossible=NaN(1,size(locationtemp,2));
    for k=1:size(locationtemp,2)
        locationpossible(k)=isreal(locationtemp(1,k));
    end

    if light.phi>=pi/2 || light.phi<=-pi/2

locationpossible=locationpossible.*(locationtemp(1,:)<=light.position(
1));
        else

locationpossible=locationpossible.*(locationtemp(1,:)>=light.position(
1));
        end
        if light.phi>=0

locationpossible=locationpossible.*(locationtemp(2,:)>=light.position(
2));
        else

locationpossible=locationpossible.*(locationtemp(2,:)<=light.position(
2));
        end
        locationpossible(2,:)=((locationtemp(1,:)-
light.position(1)).^2+(locationtemp(2,:)-light.position(2)).^2).^0.5;
        locationpossible(2, locationpossible(2,*)<0.00001)=999;
        index=find(locationpossible(2, :)==min(locationpossible(2,
locationpossible(1, :)==1))&locationpossible(1, :)==1);

        %new matrices

```

```

light.position(1)=locationtemp(1,index);
light.position(2)=locationtemp(2,index);

if interaction==1
    initialbeamlength=(sum((light.position-
lightgrid{1,1}.position).^2))^0.5;
end

% Identify surface
light.surface=mod(index,size(R,2));
light.surface(light.surface==0)=size(R,2);
% clear index

% Fresnel's equation
if light.surface~=size(R,2)
    %determine index of refraction based on which direction light
is going
    if interaction>1
        if light.surface<lightgrid{interaction-
1,ceil(branch/2)}.surface
            n1=n(light.surface+1);
            n2=n(light.surface);
        else
            n1=n(light.surface);
            n2=n(light.surface+1);
        end
    else
        n1=n0;
        clear n0
        n2=n(light.surface);
    end
    % determine angle of surface
    % if light.surface~=size(R,2)
    if ellipseangle~=0
        if light.position(2)~=0
            phisurface=atan(-
(Rmajor(light.surface)/R(light.surface))^2*(light.position(1)/light.po
sition(2)));
        else
            phisurface=pi/2;
        end
    else
        phisurface=pi/2;
    end
    % end
    %T=transmitted, R=reflected
    [Transmitted, Reflected, phiT, phiR]=fresnel(n1, n2,
phisurface, light.phi);
    light.intensity=light.intensity*Reflected;
    if phiR<-pi || phiR>pi
        light.phi=wrapToPi(phiR);
    end
end

```

```

else
    light.phi=phiR;
end
lightgrid{interaction+1,2*(branch-1)+2}=light; %#ok<*AGROW>
if isfinite(Transmitted)
    light.intensity=(light.intensity/Reflected)*Transmitted;
%have to divide back by reflected since it has already overwritten
light.intensity
    light.phi=wrapToPi(phiT);
    lightgrid{interaction+1,2*(branch-1)+1}=light;
else
    light.phi=NaN;
    light.intensity=0;
    lightgrid{interaction+1,2*(branch-1)+1}=light;
end
else
    light.phi=NaN;
    light.intensity=light.intensity;
    lightgrid{interaction+1,2*(branch-1)+1}=light;
    lightgrid{interaction+1,2*(branch-1)+2}=0;

    %path=NaN(interaction,1);
    branchtemp=branch;
    for intnum=interaction:-1:1
        path2(intnum)=lightgrid{intnum, branchtemp}.surface;
        branchtemp=ceil(branchtemp/2);
    end
    path2=path2(length(path2):-1:1);
    path2=sum([size(R,2), path2].*(10.^(0:interaction)));

    branchtemp=branch;
    for intnum=interaction:-1:1
        positions(intnum,:)=lightgrid{intnum,
branchtemp}.position;
        branchtemp=ceil(branchtemp/2);
    end
    positions(2:size(positions,1)+1,:)=positions;
    positions(1,:)=light.position;
    cumulativelength=0;
    for step=1:size(positions,1)-1
        cumulativelength=cumulativelength+(sum((positions(step,:)-
positions(step+1,:)).^2));
    end
    lightout(lightoutnum).intensity=light.intensity;
    lightout(lightoutnum).position=[light.position(1);
light.position(2)*sin(ellipseangle);
light.position(2)*cos(ellipseangle)];
    lightout(lightoutnum).path2=path2;
    lightout(lightoutnum).path=[interaction; branch];
    lightout(lightoutnum).lengthsquared=cumulativelength;
    lightoutnum=lightoutnum+1;

```

```

end

% decide on if done or next set to analyze and reload variable

if sum([lightout.intensity])>accuracy*intensity0 || interaction>10
    completed=1;
else
    completed=0;
    phi=NaN;
    intensity=1;
    while isfinite(phi)==0
        if branch<2^(interaction-1)
            branch=branch+1;
        else
            branch=1;
            interaction=interaction+1;
        end
        if isstruct(lightgrid{interaction, branch})
            phi=lightgrid{interaction, branch}.phi;
            intensity=lightgrid{interaction, branch}.intensity;
        end
    end
end

position=lightgrid{interaction, branch}.position;
surface=lightgrid{interaction, branch}.surface;
light.intensity=intensity;
light.position=position;
light.surface=surface;
light.phi=phi;
end
end
end

```

### D.2.3 Called function: fresnel

```

function [T, R, phiT, phiR]=fresnel(n1, n2, phisurface, phiin)
%Scott Wujek
%Determines transmission intensity, reflection intensity, transmission
angle, and reflection
%angle using Fresnel's Equations and Snell's Law
%n1 is the refractive index of medium from which light came
%n2 is the refractive index of medium through which transmitted light
will
%pass
%phisurface is angle interface makes wrt +x axis
%phiin is angle incident light is headed wrt +x axis

%uses all of these if statements because wrapTo2Pi and wrapToPi are
%expensive operations
if phisurface<0 || phisurface>2*pi
    phisurface=wrapTo2Pi(phisurface);

```

```

end
phisurfnormal=[phisurface+pi/2, phisurface-pi/2];

if phiin<-pi || phiin>pi
    phiin=wrapToPi(phiin);
end

thetain=wrapToPi(phiin-phisurfnormal);

select=abs(thetain)==min(abs(thetain));
if sum(select)>1 %incase the light is moving tangentially to surface
    select=1;
end
phisurfnormal=phisurfnormal(select);

if phisurfnormal<-pi || phisurfnormal>pi
    phisurfnormal=wrapToPi(phisurfnormal);
end

thetain=thetain(select);

phiR=(phisurfnormal+pi)-thetain;
if phiR<-pi || phiR>pi
    phiR=wrapToPi(phiR);
end

thetaT=asin(sin(thetain)*n1/n2);
if isreal(thetaT) %checks to see if transmission possible
    phiT=phisurfnormal+thetaT;
    if phiT<-pi || phiT>pi
        phiT=wrapToPi(phiT);
    end
    %reflected light power
    Rs=((n1*cos(thetain)-
n2*cos(thetaT))/(n1*cos(thetain)+n2*cos(thetaT)))^2;
    Rp=((n1*cos(thetaT)-
n2*cos(thetain))/(n1*cos(thetaT)+n2*cos(thetain)))^2;
    %assumes both directions of phase are equally distribured
    R=(Rs+Rp)/2;
else %total reflection
    phiT=NaN;
    R=1;
end

%conservation of energy
T=1-R;

```